

Die approbierte Originalversion dieser Dissertation ist an der Hauptbibliothek der Technischen Universität Wien aufgestellt (<http://www.ub.tuwien.ac.at>).

The approved original version of this thesis is available at the main library of the Vienna University of Technology (<http://www.ub.tuwien.ac.at/englweb/>).

DISSERTATION

Design of Optical Space-to-Ground Links for the International Space Station

ausgeführt zum Zwecke der Erlangung des akademischen Grades
eines Doktors der technischen Wissenschaften

eingereicht an der Technischen Universität Wien
Fakultät für Elektrotechnik und Informationstechnik

von

DI Martin Pfennigbauer
Frauentorgasse 42
A-3430 Tulln

geboren am 7. November 1973 in Tulln
Matrikelnummer 9325940

Wien, im Februar 2004

Begutachter:

Univ. Prof. Dr. Walter R. Leeb

Univ. Doz. Dr. Peter J. Winzer

Abstract

Innovative technologies will have to be developed in the near future to satisfy the ever increasing demand on bandwidth associated with new communication services. Free-space laser communication is a promising candidate in this field. The outstanding advantage of systems employing optical carrier frequencies in comparison to widely used radio-frequency technology is the low beam divergence. However, small beam diameters lead to high technological demands concerning mutual *pointing, acquisition, and tracking* (PAT) of the communicating terminals.

Within this thesis, the major concepts and technological requirements of an optical link operating in the Gb/s-regime between the International Space Station (ISS) and a ground station are being investigated. Such a link could serve as broadband communication channel for the scientific experiments aboard the station and would, additionally, extend the operational experience with optical space-to-ground links. I am deriving numerical benchmarks for the parameters concerning the link loss, the pointing accuracy, and the effects of atmospheric propagation. I am calculating the power spectral density originating from celestial bodies and the atmosphere of the Earth accepted by a telescope aboard the ISS or on ground and assess its impact on the performance of the system.

The distances to be bridged between the ISS and a ground station are up to 2 200 km. This fact, together with the limited transmit power, the high cost of large telescopes, and the impossibility of in-line amplification lead to the need for highly sensitive receivers to fully exploit the low signal power available. After comparing different receiver technologies, I am focussing on *optically preamplified direct detection receivers*. The system parameters affecting the receiver's performance are investigated by a self-developed simulation program and by experiments. Two forms of on-off keying modulation formats, namely non return-to-zero (NRZ) and return-to-zero (RZ), are implemented and the effect on the receiver sensitivity is being assessed. By using an RZ coded transmit signal and by optimizing optical and electrical filter bandwidths in the receiver, I experimentally approached – at a data rate of 10 Gb/s – the theoretical limit of receiver sensitivity, the *quantum limit*, as close as 1.1 dB.

I set up a laboratory breadboard of an optical transceiver implementing devices commercially available off-the-shelf to assess the potential of utilizing fiber communication technology for free space laser communication. I show that *Erbium-doped fiber amplifiers* are suitable to serve as high-power booster amplifier in the transmitter and as preamplifier in the receiver.

Many aspects of classical optical free-space communication systems, e.g., PAT, link loss, and background radiation are also relevant for *quantum communication* in space. I am investigating the implementation of *quantum cryptography* for distributing a secret key to two ground stations by employing a source of entangled photons aboard the ISS. In an assessment of the technological requirements of this scenario I identify the data rate, the accuracy of synchronization, and the link availability as critical issues.

Kurzfassung

Die durch das Angebot von neuen Kommunikationsdiensten ständig wachsende Nachfrage nach Bandbreite kann in Zukunft nur durch die Entwicklung von innovativen Technologien befriedigt werden. Ein vielversprechendes Konzept auf diesem Sektor ist die Freiraumübertragung mittels Laserstrahlen, wo Datenraten von mehreren Gb/s realisiert werden können. Einer der Hauptvorteile der Verwendung von Trägerfrequenzen im optischen Bereich im Gegensatz zur herkömmlichen Mikrowellentechnik ist die kleine Strahldivergenz. Sie geht jedoch einher mit hohen Anforderungen an die Ausrichtung und Nachführung der Antennen der kommunizierenden Endgeräte.

Die vorliegende Dissertation definiert Anforderungen und Konzepte einer breitbandigen optischen Datenübertragung zwischen der Internationalen Raumstation (ISS) und einer Bodenstation. Eine Verbindung dieser Art würde einerseits die Kommunikationsmöglichkeiten der Station mit der Erde verbessern und andererseits wesentliche Aufschlüsse über den Einsatz optischer Datenübertragung im Weltraum liefern. Ich gebe Richtwerte für die zu erwartende Signalabschwächung, die erforderliche Genauigkeit der Strahlausrichtung und den Einfluss der Atmosphäre auf die Strahlausbreitung an. Die von den Empfangsteleskopen auf der ISS und auf der Erde aufgenommene spektrale Leistungsdichte der Strahlung von Himmelskörpern und der irdischen Atmosphäre wird berechnet und der entsprechende Einfluss auf die Qualität der Übertragung analysiert.

Bei Verbindungen zwischen ISS und Erde beträgt die zu überbrückende Distanz immerhin bis zu 2 200 km, die Größe der Teleskope und die verfügbare Sendeleistung an Bord der ISS ist stark begrenzt, eine Zwischenverstärkung ist nicht möglich. Der sich daraus ergebende geringe Signalpegel am Empfänger muss optimal ausgenutzt werden. Nach dem Vergleich verschiedener Empfängertechnologien richte ich mein Augenmerk auf *optisch vorverstärkte Direktempfänger*. Mit Hilfe eines eigens entwickelten Simulationsprogramms, dem eine detaillierte Modellierung des Übertragungssystems bestehend aus Sender und Empfänger zugrunde liegt, untersuche ich den Einfluss unterschiedlicher Parameter auf die Empfindlichkeit des Empfängers. Senderseitig fasse ich zwei Modulationsformate ins Auge, nämlich NRZ (non return-to-zero) und RZ (return-to-zero). Die wichtigsten Parameter des Empfängers sind die Bandbreiten des optischen und des elektrischen Filters. Durch Verwendung eines RZ-Signals und durch sorgfältige Optimierung der Filterbandbreiten gelingt es mir, bei einer Datenrate von 10 Gb/s, der theoretischen Grenze der Empfängerempfindlichkeit, dem *Quantenlimit*, experimentell bis auf 1.1 dB nahe zu kommen.

Um das Potential des Einsatzes von kommerziell verfügbaren Komponenten, die für den Einsatz in fasergebundenen Systemen entwickelt wurden, für die optische Freiraumübertragung zu beurteilen, habe ich ein Übertragungssystem bei einer Wellenlänge von 1.55 μm aufgebaut. Ich zeige, dass *Erbiumdotierte Faserverstärker* als Leistungsverstärker im Sender und als Vorverstärker in empfindlichen Empfängern bestens geeignet sind.

Viele Aspekte der klassischen optischen Freiraumübertragung wie zum Beispiel Strahlausrichtung und Nachführung, Abschwächung und Hintergrundstrahlung sind auch für die Anwendung von *Quantenkommunikation* im Weltraum von Bedeutung. Ich untersuche den Einsatz von *Quantenkryptographie* in folgendem Szenario: Unter der Verwendung einer Quelle von verschränkten Photonen an Bord der ISS soll ein geheimer Schlüssel auf zwei Bodenstationen verteilt werden. In einer Analyse der technologischen Anforderungen identifiziere ich die nach oben beschränkte Datenrate, die Genauigkeit der Synchronisation und die Verfügbarkeit der Verbindung als kritische Parameter.

Acknowledgement

I would like to express my gratitude to my supervisor, Prof. Walter Leeb, who has always been generous towards me with his time, knowledge and sound experience. His lucid comments and critical questions improved the scientific quality of this thesis. Furthermore, I am sincerely indebted to Peter Winzer, who not only proposed the methodology for the research presented here but also followed my progress with eager interest. Major results of this work could not have been obtained without his enthusiasm and ability to motivate.

I would like to thank my colleagues Martin Strasser and Martin Pauer with whom I kept a close teamwork, particularly concerning the experiments. I also appreciate the various discussions with Oswald Wallner, reaching from basic physics to word processing. Bernhard Furch, Zoran Sodnik, and Josep Maria Perdigues from the European Space Agency were always willing to share their hands-on experience with aerospace systems. I owe special thanks to Prof. Anton Zeilinger and Markus Aspelmeyer for unveiling some of the secrets of quantum physics to me.

Major parts of this work were performed under ESA/ESTEC contracts. I am also grateful for the funding provided by *Fonds zur Förderung der wissenschaftlichen Forschung* and *Hochschuljubiläumsstiftung der Stadt Wien*.

Last but not least I want to thank my family for their continuing support.

Contents

1	Introduction	1
1.1	Establishing an optical link to the ISS: benefits and difficulties	1
1.2	International efforts towards satellite laser communication	2
1.3	Receiver technologies	6
1.4	Choice of laser wavelength	10
1.5	Intention of the work	11
2	Link Properties	13
2.1	Link distance	13
2.2	Link availability	15
2.3	Influence of atmosphere	16
2.3.1	Absorption	16
2.3.2	Scattering	17
2.3.3	Turbulence	17
2.4	Link attenuation	20
2.5	Background radiation	22
2.5.1	Radiation from celestial bodies and ISS	25
2.5.2	Radiation from Earth	26
3	Pointing, Acquisition & Tracking	29
3.1	Pointing	30
3.2	Acquisition	30
3.3	Tracking	30
3.4	Point ahead angle	31
3.5	Pointing accuracy – choice of the telescope size	33
3.6	Adaptive optics	35
4	Receiver Sensitivity	37
4.1	System setup	37
4.1.1	Optical input field	38
4.1.2	Optical preamplifier	40
4.1.3	Optical bandpass filter	41
4.1.4	Photo diode module	41
4.1.5	Analog-to-digital conversion	43
4.2	Noise model	44
4.2.1	Advanced Gaussian model	46
4.2.2	Standard model	46

4.3	Calculating the receiver sensitivity	47
4.4	Simulation results	47
4.4.1	Decision threshold and sampling instant	47
4.4.2	Filter bandwidth optimization	49
4.4.3	Influence of filter characteristics	55
4.4.4	Polarization filter	58
4.4.5	Influence of transmitter properties	58
4.5	Measurements	62
4.5.1	Experimental setup	62
4.5.2	Results	63
5	Breadboarding a System Employing Commercial Devices	67
5.1	Breadboard Setup	67
5.2	Receiver sensitivity measurements and simulations	70
5.2.1	Simulation	70
5.2.2	Measurements with NRZ-coded input signal	71
5.2.3	Measurements with RZ-coded input signal	73
5.3	Discussion	74
5.3.1	Transmitter	74
5.3.2	Receiver	75
5.4	Effects leading to the difference to the quantum limit	76
6	Quantum Communications in Space	77
6.1	Principles of quantum key distribution with entangled photons	77
6.1.1	Quantum entanglement	78
6.1.2	Quantum key distribution protocol	78
6.2	State-of-the-art of quantum key distribution	79
6.3	Quantum communication scenarios comprising the ISS	80
6.3.1	Earth-based transmitter terminal	80
6.3.2	ISS-based transmitter terminal	81
6.4	Quantum key distribution between two ground stations using the ISS	81
6.5	Assessment	83
	Appendices	85
A	Link duration between the ISS and a ground station	87
B	Abbreviations, constants, and symbols	89
B.1	List of abbreviations	89
B.2	List of physical and mathematical constants	90
B.3	List of astronomical data	91
B.4	List of Latin symbols	91
B.5	List of Greek symbols	93
	Bibliography	95
	Curriculum Vitae	105

Chapter 1

Introduction

1.1 Establishing an optical link to the ISS: benefits and difficulties

The International Space Station (ISS) is the largest scientific cooperative and engineering development program in history and its purpose is to “offer an extensive range of facilities in a unique environment that cannot be found on Earth, and will enable mankind to continue to learn how to live and work in space for long periods” [1]. In this thesis I want to assess the possibilities of an optical link between the ISS and a ground station. The benefits of establishing an optical link to the ISS would be twofold: First, to advantageously make use of the easily accessible and serviceable infrastructure; and second, to support the scientific program onboard the ISS by providing a broadband link.

The current communication bandwidth available between ISS and ground is 72 kb/s for the uplink and 43 Mb/s for the downlink mainly via TDRSS¹, and possibly also via ARTEMIS or DTRS². When taking into account that a portion of the data traffic is needed to operate the station itself, comparatively low data rate is available for research projects [1]. However, bandwidth-consuming real-time monitoring of certain experiments may be desired to enlarge the scientific output and/or reduce possible risks for the crew due to experiments out of control.

Optical communication systems linking the ISS with other satellites or a ground station have been considered quite from the beginning of the design of the ISS. Corresponding projects are planned or under development in Japan [5, 6], the USA [7] and, more recently, also in Europe (cf. Chapt. 6).

The potential advantages of optical data transmission over RF-based systems are well known and have been laid down in e.g. [8–11]. They mainly originate in the extremely high carrier frequency. Compared to the S-band (2 GHz) or Ka-band (23 GHz) used by the TDRSS, the frequency of a laser operating at, e.g., 1 550 nm is higher by 5 or 4 orders of magnitude. For equal antenna dimensions, this results in a beam divergence reduced by the same factor and the potential availability of extremely high communication bandwidths. Data rates of 10 Gb/s with antenna diameters in the range of 25 cm are achievable with state-of-the-art

¹The Tracking and Data Relay Satellite System (TDRSS) is a radio frequency (RF) communication signal relay system that provides tracking and data acquisition services between low earth orbiting spacecraft and ground. The system is operated by the USA, consists of seven GEO satellites, and is capable of transmitting to and receiving data from spacecraft permanently [2].

²The European ARTEMIS and the Japanese Data Relay Test Satellite (DRTS), both GEO satellites, have RF transmission systems to relay data between a spacecraft (low earth orbit satellites, space stations, etc.) and ground stations [3, 4].

components. The low divergence of the beam is not only a major merit but also a major difficulty of optical communication systems. It asks for a sophisticated pointing, acquisition and tracking (PAT) mechanism and impedes the possibility of multi-terminal or broadcast communication. Links can only be established between two partners, a fact that might on the other hand be desired for security reasons.

The altitude of the ISS is as low as some 400 km, resulting in a high relative velocity of the space and ground terminal. For an ISS-to-ground link, this asks for fast tracking, and a large point ahead angle (PAA). Another consequence of the low altitude is the comparatively short link duration. Only a few minutes of communication are possible for each orbital pass. Depending on the latitude of the ground station there are about four passes with different possible link periods within every 24 hours, limiting the overall amount of data to be transferred via the optical link. Of course, this problem could be overcome by using several ground stations. It is not quite possible, though, to establish uninterrupted communication. This would afford a very dense network of ground stations and two space terminals aboard the ISS for handover.

Another issue is the fact that the ISS is a manned spacecraft. Security regulations are much more stringent than on an unmanned satellite. Additionally, astronaut crew activities cause high vibrations tightening the requirements for the PAT system.

Nevertheless, I think it is worth while to consider optical space-to-ground links, especially employing the ISS as a platform for the space terminal. Such a system has the potential to improve both the performance of the ISS communication and to enlarge the experience with optical free space communication terminals.

1.2 International efforts towards satellite laser communication

Since the early seventies efforts towards optical space communications have been undertaken worldwide, mainly in the USA, Europe, and Japan. Links from ground to space (and vice versa), deep space communications and intersatellite links (ISL) were considered [12, 13]. Recently, the first non-classified optical intersatellite link has been established between SPOT-4 and ARTEMIS, two satellites built by European consortia [14].

In the following, I will give a brief overview of some optical space communication systems that have been designed and partially operated in the past 15 years. Projects representing milestones or having special impact on the ISS were selected. Representing the most important parameters of optical communication terminals, the transceiver technology, telescope aperture size, and the weight and power consumption of the system are emphasized. The aim of this section is to assess the state-of-the-art within this field, providing a baseline for the considerations to follow.

Systems realized and tested

Semiconductor Laser Intersatellite Link Experiment (SILEX): This project consists of two optical communication payloads – OPALE and PASTEL – embarked on ESA's ARTEMIS (Advanced Relay and Technology Mission Satellite) spacecraft and on the French Earth-observation spacecraft SPOT-4, respectively. It allows data transmission at 50 Mb/s from low earth orbit (LEO) to geostationary orbit. The OPALE terminal on ARTEMIS is capable of transmitting data at a rate of 2 Mb/s. It can also receive an optical signal from a LEO satellite. This link will be established either with the Japanese OICETS (cf.

below) or with ESA's optical ground station (OGS) simulating a LEO terminal.

The SILEX terminals OPALE and PASTEL have an aperture of 25 cm, a mass of 157 kg and a power consumption of 150 W. Acquisition is achieved with a beacon laser from OPALE (generated by 19 laser diodes) detected by CCD sensors located on PASTEL, after pointing towards each other on the basis of satellites orbital data. After detecting the beacon signal, PASTEL emits its communication signal which will be detected by OPALE. OPALE then switches off its beacon [14].

On ARTEMIS, AlGaAs lasers operating at a wavelength of 819 nm with an output power of 120 mW are used for data transmission. The receiver is based on direct detection at 847 nm [13, 15].

The first successful link test took place on November 22, 2001, constituting the very first non-classified communication between satellites using a laser beam as carrier. A first image was transmitted on November 30, 2001. Also, an optical link between ARTEMIS and OGS was established.

Laser Utilizing Communications Equipment (LUCE): The LUCE terminal is part of Japan's OICETS (Optical Inter-orbit Communications Engineering Test Satellite) spacecraft. It is fully compatible with the SILEX terminal on ARTEMIS. When OICETS will be finally launched (launch was planned for 1998 but is postponed since then), a bi-directional link with the OPALE module shall be established. The terminal will transmit at a data rate of 50 Mb/s and is capable of receiving 2 Mb/s [13, 16].

Laser Communications Equipment (LCE): This Japanese project was planned to establish space-to-ground and ground-to-space data transmission at 2 Mb/s and 1.024 Mb/s, respectively. It was embarked on the ETS VI spacecraft, which did not reach the planned geostationary orbit but an elliptical orbit, restricting the mission objectives.

The space-borne terminal has an aperture diameter of 7.5 cm. Its mass is 22.4 kg and the power consumption is 90 W maximum. A semiconductor laser diode serves as light source. The ground terminal in Tokyo has a 1.5 m telescope and uses an Argon laser for the uplink. Intensity modulation and direct detection is implemented.

Due to the unexpected orbit of the satellite, most of the experimental results were not achieved with the Tokyo ground station but with JPL's Table Mountain facilities in California [17].

Space Technology Research Vehicle (STRV-2): One part of the STRV-2 was a low earth orbit satellite laser communication terminal on the US Air Force Tri-Service Experiments (TSX-5) spacecraft, launched in July 2000. The terminal was designed to transmit data at up to 1.24 Gb/s over a link distance of 1 600 km. The space terminal had an aperture of 13.7 cm diameter for reception and 10 transmit apertures with 2.5 cm diameter (8 for communication and 2 for the beacon laser). The ground terminal provided three 30.4 cm transmit and one 40.6 cm receive aperture. All four telescopes were of the Meade Schmidt-Cassegrain type [18]. Each of the transmit telescopes broadcasted 12 laser beams to reduce the uplink scintillation at the satellite.

The design of the satellite and the ground optical communication transceivers were based on direct modulation of semiconductor lasers, direct detection using avalanche photodiodes and separate acquisition/tracking and communication wavelengths of 852 nm and 812 nm, respectively. Acquisition and tracking was CCD-camera supported and performed by two-axis gimbals in both the space terminal and the ground terminal. The ground terminal had additional separate fine steering mirrors for all three transmit

apertures and the receive telescope.

No optical communication link was achieved because the satellite terminal could not acquire and track the ground terminal beacon, the reason being that the spacecraft's attitude control operated out of specification [19–21].

GeoLITE: There are indications that there is another laser-based ISL operating, developed by military research facilities in the USA. This system is believed to use a wavelength of 1 550 nm, optically preamplified detection, employing commercial off-the-shelf components to a large extent. Obviously space qualifying Erbium doped fiber amplifiers has been obtained. The name of the system is GeoLITE [12].

Systems developed but not yet launched

Coherent Detection Terminal (CDT): This demonstrator of an optical intersatellite link terminal, developed by Bosch Telecom GmbH, Germany, is designed to communicate over a distance of 6 000 km with an aperture diameter of 9 cm. The mass of the module is in the range of 25 kg with a power consumption of less than 100 W and a lifetime of more than 8 years. In the laboratory, data rates as high as 7.8 Gb/s were demonstrated, for operational conditions some 2.5 Gb/s are expected. The optical transmitter employs a Nd:YAG laser and a LiNbO₃ waveguide modulator for phase modulation. An Yb-doped fiber amplifier boosts the output of the modulator (some 100 mW) to the desired transmit power of 1 W. Homodyne reception implementing a Costas phase locked loop is used. The tracking and acquisition subassembly works as follows: The receiver front end comprises four fast communication photodiodes for data detection and several large-area photo diodes for generating acquisition error signals. For generation of tracking error signals, two of the four communication photo diodes are divided physically. There is no dedicated beacon laser, the communication laser is used for PAT issues [22–24].

Coherent Analog Communication System (OPTEL 25): Anticipating a demand for optical terminals which can handle analog transparent communications channels, Contraves Space AG developed a coherent analog laser transmission system for intersatellite applications. The terminal is designed for GEO-GEO link with a link distance of 25 000 km.

The terminal is capable of transmitting, re-arranging and duplicating several analog channels of 36 MHz bandwidth with a channel-spacing of 41 MHz. The transceiver setup is similar to that of a digital terminal. The transmitter includes a Nd:YAG laser operating at 1 064 nm, an electro-optical modulator and a booster amplifier. A high-sensitive coherent receiver permits the transmit power and consequently the DC power consumption of the terminal to be low.

Acquisition is performed by means of a beacon laser at 808 nm. To avoid large moving masses, coarse pointing is performed by a 2-axis mirror [25].

Systems employing the ISS

Laser Communications Demonstration Experiment (LCDE): The space terminal is planned to be installed on the Japanese Experimental Module (JEM) attached to the International Space Station. The aim of the project is to perform communication experiments with several ground stations at a downlink data rate of 2.5 Gb/s and an uplink data rate

of 1.2 Gb/s. The experiment was expected to take place in the year 2004 for a duration of about one year, but right now it is dormant (information through personal communication).

One challenge is to compensate for the strong vibrations common to a manned space facility. Coarse tracking is performed by 2-axis gimbals providing a field-of-view (FOV) of 10 mrad and a Si CCD detector, fine tracking with a quadrant photo-detector and a 2-axis fast steering mirror.

The optical transceiver employs an Erbium-doped fiber amplifier (EDFA) capable of boosting the output power to a maximum value of 1 W. However, the actual output power will be reduced to the level of 400 mW to assure eye safety. The laser wavelength is 1 552 nm for transmission and 1 562 nm for reception. DPSK or intensity modulation will be implemented. The optical antenna is a coaxial Cassegrain type telescope with Coudé optics and has a diameter of 15 cm. The terminal weighs less than 90 kg and has a power consumption below 115 W [5, 6].

Optical Communication Demonstration and High-Rate Link Facility (OCDHRLF): The Jet Propulsion Laboratory is developing a Gb/s-class optical communications downlink for the ISS in cooperation with the International Space Station Engineering Research and Technology development program (ISSERT). The OCD terminal [26] is adapted for this purpose. Operation of the OCDHRLF was planned for October 2002. Right now, the project seems to be in a dormant state.

The diameter of the transmit aperture for the flight terminal and the ground receiver aperture are 10 cm and 100 cm, respectively. For eye safety reasons, a wavelength of 1 550 nm is chosen for the transmit signal. An Erbium-doped fiber amplifier boosts the directly modulated data signal provided by a DFB laser to an output power of 200 mW.

To provide a reference signal for the PAT system at a wavelength sensitive to silicon focal plane arrays, the light from a low-power 980 nm laser diode is coupled in the single mode fiber carrying the transmit signal after the booster amplifier. A steering mirror is used for controlling the beam, while coarse pointing is performed by a gimbal [7, 27].

Assessment

The development of free space laser communication has not yet reached a high degree of maturity and no general design rules have been established. This opens a wide field for research and development to which this work may contribute. Nevertheless, several tendencies can be observed when surveying past projects.

The first applications in mind for free space laser communication terminals was data relaying using a geostationary satellite (e.g. ESA's SILEX mission) or communication for deep space missions (e.g. by NASA's JPL). In the early 90ies the conception of satellite networks like TELEDESIC or IRIDIUM seemed to open a promising field for laser communication terminals. Unfortunately, developments in that direction have proven to be commercially unprofitable and consequently are now dormant. On the other hand, the successful operation of SILEX and projects concerning the ISS (e.g. LCDE, OCDHRLF) give hope that, with the experience to be gained, the development of future systems will accelerate.

As a receiving method, direct detection was implemented first because of the comparatively simple setup (examples are the projects SILEX, LCE [17], and OCD [26]). Later, coherent receivers were investigated with the aim to achieve higher sensitivity and better immunity to

background radiation. Examples for these efforts are Lincoln Labs' "space coherent optical communication system" and SOLACOS [28] and SROIL [13] in Europe. Presently the two prime candidates for long-distance optical free space links are one based on Nd:YAG lasers (wavelength $\lambda = 1\,064\text{ nm}$) with homodyne reception and one based on semiconductor lasers operating at $\lambda = 1\,550\text{ nm}$ with direct detection. The advantage of the former is a somewhat better sensitivity (at least in theory), the merit of the latter its simplicity and the excellent availability of commercial off-the-shelf components developed for the fiber communication market. Lately the competition was pushed by attractive experimental results for the sensitivity of direct detection systems [29,30].

In the following section I will detail the mentioned reception technologies and point out which technology I consider best suited for the considered link scenario.

1.3 Receiver technologies

The receiver front-end is a crucial subsystem of any free space laser communication terminal. Because of the large distances in combination with the small telescopes usually employed to save on weight, high path attenuation has to be expected (without the possibility of in-line amplification, of course). This fact and the limited transmit power available at the transmitter aboard a space-based terminal leads to the desire to optimally exploit the power available at the receiver. Therefore the receiver sensitivity – the input power (or the number of photons per bit) necessary to achieve a certain bit error probability – is one of the major parameters when designing the optical transceiver. I will now discuss five different receiver technologies and their impact on system performance:

- direct detection (DD)
 - DD with *pin* photo-diodes
 - DD with avalanche photo-diodes (APDs),
 - optically preamplified DD;
- coherent detection
 - homodyning,
 - heterodyning.

The receiver sensitivity is often expressed relative to the *quantum limit* of the corresponding technology. This limit is the performance resulting from an ideal system neglecting any background illumination or noise from subsequent electronics. Any bandwidth limitation is matched to the input signal's pulse shape. The only non-ideal effect taken into account is the statistical distribution of the photons arrival instant at the photo diode and (for the optically preamplified DD receiver) the amplified spontaneous emission (ASE) of the preamplifier. Anyway, I will not only discuss the performance concerning input power but also mention issues such as sensitivity towards background radiation, fiber coupling, availability of components, and technological difficulties. These considerations will put me in the position to make a choice of the proper technology for a link from the ISS to a ground station.

Direct detection employing *pin* diodes

The most simple way of detecting optical data is direct detection employing *pin* photo-diodes³. The optical signal at the telescope is coupled to the photo-diode. The electrical signal proportional to the optical input power is then amplified and filtered. The receiver sensitivity achievable with this technology is poor (some 5 000 photons per bit [31, 32]) because of the high impact of thermal noise, which lets me exclude direct detection receivers employing *pin* diodes from further considerations.

Direct detection employing APDs

To improve the performance of direct detection receivers, the incoming signal is amplified within the photo-diode [33]. Sensitivity performance is not close to the quantum limit at data rates beyond 1 Gb/s due to the limited gain bandwidth product and the comparatively large excess noise factor⁴ of APDs. Some 1 000 photons per bit are necessary to achieve a bit error probability of 10^{-9} [34] at a data rate of 10 Gb/s; some 200 photons per bit are needed at 50 Mb/s [15].

To avoid problems that might come along with single-mode fiber coupling (positioning, angular alignment [35]), the possibility of multi-mode fiber coupling or positioning the photo-diode directly in the focal point of the telescope seems to be an attractive method.

If the telescope/fiber system has a larger field-of-view (FOV) than given by the diffraction limit, spatial filtering of the background radiation will be poor, leading to high performance deterioration when bright celestial bodies like Sun or Venus are within the receive telescope (FOV). A single-mode fiber would act as optimum spatial filter and therefore reduce the influence of background radiation.

Optically preamplified direct detection

Optically preamplified direct detection receivers are presently considered in different free-space laser communication projects, namely LCDE [5, 6] (Japan), and OCDHRLF [7, 27, 36] as well as GEO-Lite [12] (USA). They combine the properties of a comparatively simple setup and of high realizable receiver sensitivity.

A low noise optical preamplifier is employed at the receiver's front end. This amplifier (fiber amplifier or semiconductor amplifier) introduces amplified spontaneous emission (ASE) with the power spectral density $N_{ASE,p} = hfG_pF_p/2$ per spatial and polarization mode [33, 37, 38]. In this equation hf stands for the energy of a photon, G_p represents the preamplifier's gain and F_p denotes its noise figure, which is always larger than 3 dB. This incoherent light adds to the background radiation⁵ N_{back} , resulting in a total power density of $N_0 = N_{ASE,p} + G_pN_{back}$ at the amplifier output. Assuming the power gain of the amplifier to be high, the detection noise is dominated by beating of either N_0 with itself or with the signal. In most cases the second contribution will have a more pronounced influence on system performance than the first. The optical preamplifier is usually a single-mode device and therefore serves as spatial filter for the incoherent background radiation. It is shown in

³The abbreviation *pin* stands for *p-doped/intrinsic/n-doped*, and describes the basic layer structure of the associated semiconductor device.

⁴The excess noise of an APD is caused by the statistic nature of the multiplication process.

⁵The background radiation may comprise the ASE from the booster amplifier at the transmitter, cf. Sect. 4.2

Sect. 4.4.5 and in [29] that for a well-designed system, optically preamplified DD receivers are nearly insensitive to background radiation.

An optical bandpass filter is implemented after the preamplifier to spectrally curtail the broadband ASE and background radiation. The choice of the bandwidth of this filter is not a trivial task. On one hand, too narrow filters not only introduce optical intersymbol interference (ISI) but may also reduce the signal's power. Additional problems arise with the alignment of the filters' center wavelength and the laser's emission wavelength. Too broad filters on the other hand fail to sufficiently reduce the ASE power at the photo-diode. Similar considerations apply for the bandwidth of the electronics following the photo-diode.

My colleges and I experimentally approached the theoretical limit for the receiver sensitivity of 38 photons per bit by as much as 1.5 dB, i.e. requiring 52 photons per bit at a data rate of 10 Gb/s. In this case I employed return-to-zero (RZ) coding scheme [39]. For the same data rate, in the course of the FALCO project performed at the Vienna University of Technology and supervised by ESA, I obtained a value below 110 photons per bit with commercial off-the-shelf components (except for the sampling circuit) and a very simple transmitter setup (non return-to-zero (NRZ) coding) [29]. Optically preamplified direct detection receivers will be thoroughly discussed in Chapt. 4 and Chapt. 5.

Coherent receivers

There are two possible ways of coherent detection: heterodyning and homodyning. Both implement a local laser oscillator (LO), whose signal beats with the communications signal when detected by the photo-diode. For homodyning the frequency of the LO is exactly the same as the received signal's carrier frequency, the optical signal is transformed directly into baseband [31,40,41]. For heterodyning there is a frequency difference of 3 to 5 times the data rate resulting in a corresponding intermediate frequency.

To obtain high-sensitive receivers, the strong LO not only amplifies the received signal but also dominates all other technical noise sources by its shot noise. Since the optical signal is completely transposed to the electrical regime (i.e. with amplitude and phase), demodulation can be carried out electronically. Therefore, various modulation formats are possible for coherent receivers (e.g. OOK, FSK, PSK, DPSK).

Coherent receivers are very robust with respect to background radiation since the LO serves as a spatial single-mode filter. The limit for negligible N_{back} is the same as for optically preamplified DD receivers.

Irrespective of the modulation format applied, heterodyne receivers have the same theoretical sensitivity limit as optically preamplified direct detection receivers when employing DPSK, i.e. 20 photons per bit, being 3 dB below the theoretical minimum sensitivity for OOK and DD [40,42]. For PSK modulation, homodyning yields an improvement of 3 dB with respect to heterodyning, resulting in a quantum limit 6 dB below that for optically preamplified OOK reception.

The improved sensitivity for coherent receivers comes at the price of increased system complexity. For heterodyning, the receiver electronics must provide a bandwidth of about 5 times the data rate, which might be a limiting factor when transmitting in the Gb/s regime. Additional problems may arise, if the linewidth of transmit laser and/or LO is not far below the signal bandwidth. For homodyning, an optical phase locked loop has to be realized which locks not only the frequency of received signal and LO, but also the phase. Wavelength fluctuations and Doppler shifts, a consequence of the relative velocity of the two terminals, must

be compensated for. For heterodyning this can be done by an electrical LO, for homodyning the compensation must be performed in the optical regime. (Direct detection receivers on the other hand are generally indifferent to such frequency deviations, provided that the optical filter is not too narrow.)

As already mentioned, information about frequency and phase of the incoming signal is preserved in coherent receivers. This imposes high demands on the quality of the telescope, mirrors, and coupling lenses of the optical system to avoid wavefront errors. Single-mode fiber coupling of any component is mandatory since the light propagating in a multi-mode fiber is not coherent.

Technically achievable receiver sensitivities

In Tab. 1.1 I summarize the quantum limit for the different receiver technologies and compare these theoretical limits with experimentally achieved receiver sensitivities at a data rate of $R = 10 \text{ Gb/s}$. The lowest sensitivity achieved was for an optically preamplified DD receiver.

$R = 10 \text{ Gb/s}$ $BEP = 10^{-9}$	homodyne	APD DD	optically preamplified DD	
modulation format	PSK	OOK	OOK	DPSK
ideal sensitivity (in photons per bit)	9	10	38	20
reference	[43]	[31]	[31]	[31]
experimentally achieved sensitivity (in photons per bit)	101	2000	52	30
reference	[44]	[34]	[39]	[45]

Table 1.1: Theoretical limits and experimentally achieved sensitivities for different receiver technologies ($\lambda = 1550 \text{ nm}$, $R = 10 \text{ Gb/s}$)

Assessment

The high technological complexity and the fact that subsystems (e.g. the optical phase locked loop employed to keep the LO's frequency at that of the receive signal) are not highly developed, especially for a wavelength of 1550 nm (which I intend to focus on as lined out in the following section), make me exclude homodyne reception in further considerations. Heterodyne receivers, although less sophisticated, are more limited with respect to data rate than their competitors.

The sensitivity values achievable with APD receivers at high data rates are not very encouraging. Nevertheless, the advantage of the simple setup and the possibility of multi-mode fiber coupling give a motivation to opt for this technology especially when considering a low-cost laser communication terminal.

The high degree of development of the components in a optically preamplified direct detection receiver along with the excellent sensitivity results let me conclude that this technology seems to be the best choice for ISS-to-ground laser communication systems, especially when considering data rates in the multi-Gb/s-regime. The present thesis will be focussed on optically preamplified direct detection receivers, other technologies will frequently be called on for comparison.

1.4 Choice of laser wavelength

Custom wavelengths for laser communication systems and the corresponding laser materials are:

532 nm	Nd:YAG (frequency doubled),
830 nm	AlGaAs,
1 064 nm	Nd:YAG,
1 550 nm	InGaAsP,
10.6 μm	CO ₂ .

The first choice for free space systems were CO₂ lasers (e.g. [46]) because of the high output power that can easily be obtained with such devices and the availability in the early days of optical communication. Another issue is the relaxed PAT requirement due to the increased divergence when using such long wavelengths. Also Nd:YAG solid state laser systems were investigated in early days and are considered until now (e.g. [47], CDT [22], and OPTEL 25 [25]). Semiconductor laser diodes were implemented since their development because of the compact and robust setup typical for semiconductor components. The most prominent system based on this technology is SILEX [13].

The main motivation for the choice of the wavelength to be considered within this thesis is the availability of highly developed components. Most long-haul terrestrial fiber communication systems operate at 1 550 nm because of the comparatively low fiber attenuation and because of the availability of low-noise optical amplifiers, namely Erbium-doped fiber amplifiers (EDFAs). Little modifications are necessary to make these components applicable for space-based systems. Therefore I will confine the considerations to follow to a wavelength of $\lambda = 1\,550\text{ nm}$.

In difference to terrestrial applications, the most critical issues for space-borne laser communication terminals are the high demands for reliability and the increased radiation in space. The temperature environment is generally quite stable aboard a spacecraft. The most sensitive subsystem of the optical transceiver with respect to radiation hardness is the EDFA. Nevertheless it was reported lately that not more than 0.5 dB performance loss due to radiation by a dose of 100 krad has to be expected [30].

The technology transfer may as well work in the reverse direction: A space-borne laser communications terminal designed for 1 550 nm can easily be adapted for terrestrial free space links, an emerging technology with high growth potential. Such links are used to establish fast and cheap last-mile connections or to provide an intermediate solution until fibers are laid.

Another important issue, especially when directing a narrow laser beam towards a manned spacecraft, is eye safety. At the wavelength of 1 550 nm, being well above the visible range, the lens of the human eye does not focus incoming light into the cornea. Possible eye damage can occur only due to absorption in the lens itself. In a space-to-ground link the spatial power density on ground or at the space terminal (i.e. at the ISS) will not be high enough to cause harms of that kind⁶.

The beam divergence being large compared to systems operating at 1 064 nm or 830 nm for equal transmit antenna aperture might be seen as a disadvantage of the wavelength $\lambda = 1\,550\text{ nm}$, when the link loss due to beam divergence is considered.

⁶According to the laser classification system, beams with a power density of less than 25 W/m² are considered uncritical.

1.5 Intention of the work

The purpose of this work is to make assessments on the engineering aspects of a free space laser communication system establishing a link between the ISS and a ground station. Main focus will be placed on the optical receiver, namely an optically preamplified direct detection receiver, operating at the wavelength of 1550 nm. The transmitter properties will only be mentioned with regard to their influence on the receiver performance.

In the following two chapters I will give an overview of the link properties, concerning link availability, attenuation, atmospheric influence, and background radiation. The engineering challenges of pointing, acquisition and tracking will be addressed.

Thorough investigations on the design parameters of the receiver with respect to optimum sensitivity, both theoretically and experimentally, have been performed. In Chapt. 4, I report on the results of these efforts and line out how the different parameters interact in the system.

I set up a breadboard implementing devices available commercial off-the-shelf to assess the potential of utilizing fiber communication technology for free space laser communication. The results are summarized in Chapt. 5.

Recently, communication schemes making use of quantum physical effects like, e.g., entanglement or the “no-cloning theorem” have reached a degree of development as to leave the laboratory of experimental physicists and become commercially available. The adaptation of such techniques for space-to-ground links is discussed in Chapt. 6 from the engineering point-of-view.

It is my conviction that free space laser communication – though being in its infancy still – is going to play an important role in future worldwide communication networks. Both, the increasing demand of individual broadband access to the internet or other information services to come, and decreasing costs for development and launch of satellites will lead to the advent of this powerful technology.

Chapter 2

Link Properties

2.1 Link distance

The ISS is in a low-earth orbit (LEO) with an inclination angle of 51° . It performs 15.6 orbits per day, corresponding to 92 minutes for one revolution. The altitude varies between 350 km and 460 km, depending on the solar activity cycle, causing the atmosphere of the earth to expand and shrink. Expanding atmosphere forces the ISS to increase its altitude to minimize atmospheric friction causing the ISS to sink. Besides these comparatively slow altitude variations¹, there are periodical reboosts to compensate for the unavoidable atmospheric drag of some 200 m downwards per day [1, 48]. I will take an average altitude of 400 km as baseline for the calculations to follow. The possible duration of communication will be longer, whereas the link attenuation will be worse than the results presented when the ISS eventually is at higher altitudes.

In the following, the distance L of a satellite with altitude h from a ground station with given altitude above sea-level a is calculated depending on the elevation angle ε for $a < h$. Figure 2.1 shows a sketch of the orbit of the satellite over the Earth's surface ($r_E \dots$ radius of Earth). I consider the triangle L , $r_E + a$ and $r_E + h$. Simple trigonometric calculations yield²

$$L = (r_E + h) \left[\sqrt{1 - \left(\frac{r_E + a}{r_E + h} \cos \varepsilon \right)^2} - \frac{r_E + a}{r_E + h} \sin \varepsilon \right]. \quad (2.1)$$

In literature dealing with the influence of the atmosphere (e.g. [49–51]), the distance L is calculated by using the asymptotic value, valid for $r_E \rightarrow \infty$,

$$L = \frac{h - a}{\sin \varepsilon}. \quad (2.2)$$

Figure 2.2 shows calculation results for the link distance L for the elevation angle from $\varepsilon = 0$ to 90° for $h = 500$ km, the altitude of the ISS. The altitude of the ground station³ $a = 2.5$ km. The Earth's radius is $r_E = 6377$ km. Especially for low elevation angles, the error of the approximation is considerable (e.g. 20% for $\varepsilon = 20^\circ$). Although the link distance amounts to 2290 km for an elevation angle of 0° , I will assume a minimum elevation angle of some

¹The solar activity cycle lasts for 11 years.

²All angles have to be inserted in the equations in radians, even if given in degrees in the text.

³The altitude of the ground station has little effect on the rough calculations performed here (the exact shape of the Earth is not considered, also), and will therefore be neglected from now on ($a = 0$).

$\varepsilon_{min} = 10^\circ$ as more realistic for an optical communications link. According to cf. Fig. 2.2 this corresponds to $L = 1\,430$ km.

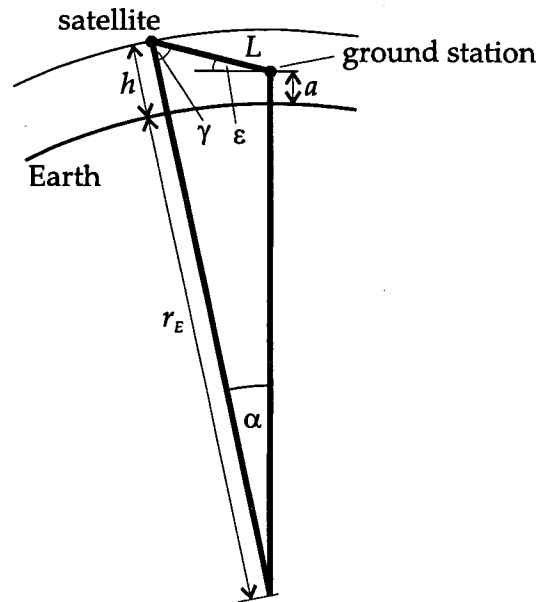


Figure 2.1: Satellite on its orbit over a ground station.

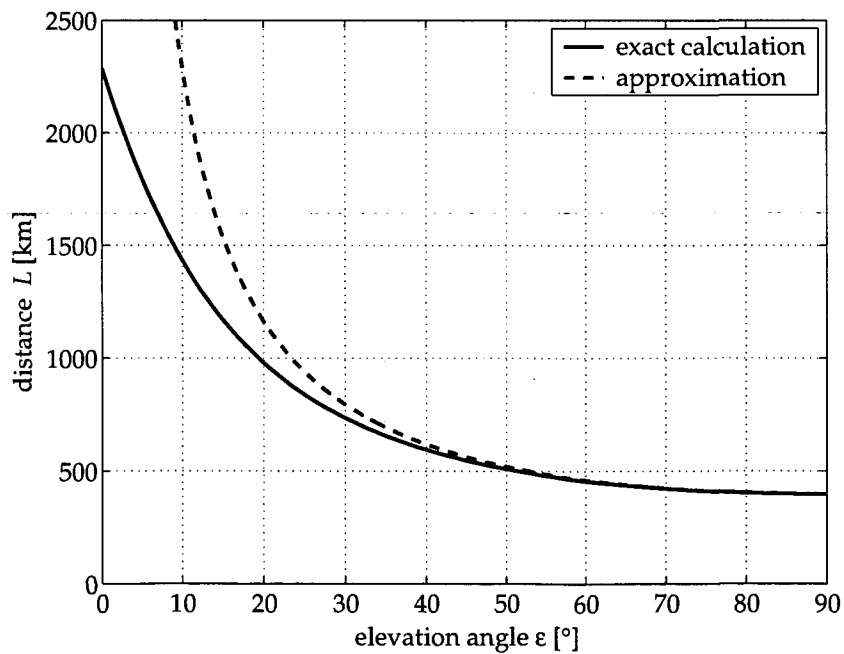


Figure 2.2: Distance between ISS and ground station as a function of the elevation angle for $h = 400$ km, $a = 2.5$ km, and $r_E = 6\,377$ km.

2.2 Link availability

As a consequence of the low altitude of the ISS, the link time is limited to a few minutes for each orbital pass (cf. e.g., [52]). I will now estimate⁴ how often and for how long a link may be established. The situation of the ISS passing a ground station is depicted in Figure 2.3 (a). The potential link duration depends on the minimum elevation angle ε_{min} . Figure 2.3 (b) shows schematically the trajectory of the ISS over a ground station. That part where a link is possible is highlighted with a bold line. I use five parameters to estimate the link period for a certain orbit: the inclination ϕ_i and altitude h of the ISS, the ground station's latitude Ψ , the minimum elevation angle⁵ ε_{min} , and the longitudinal shift of the actual orbit Δ_{long} (cf. Appendix A).

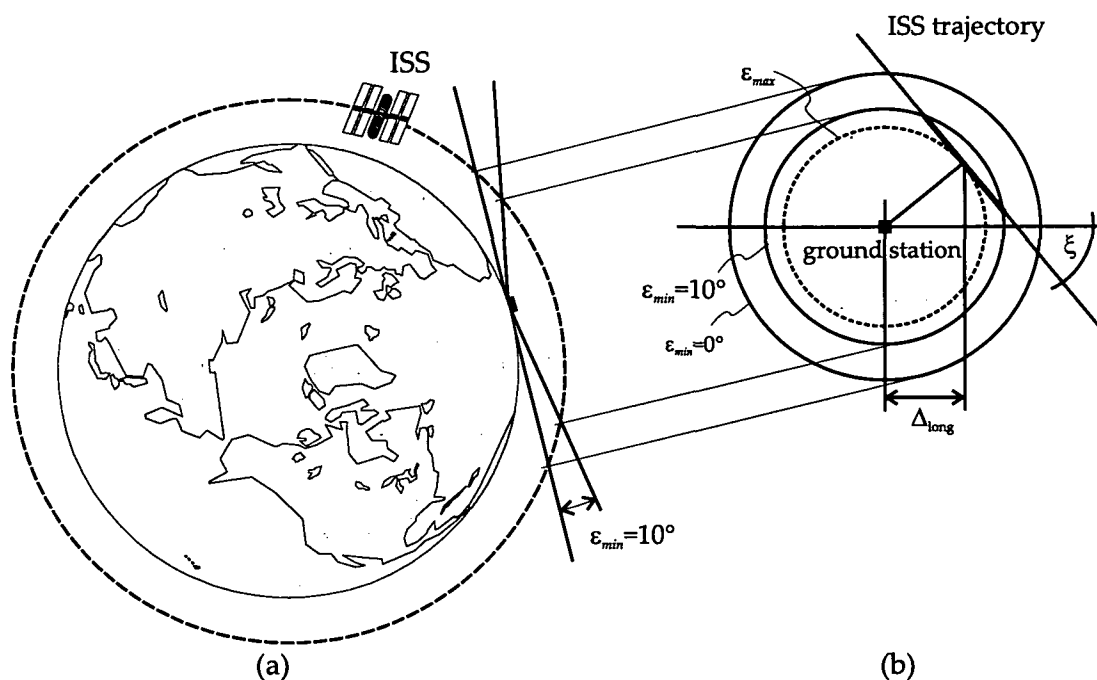


Figure 2.3: ISS on its orbit and ground station with its potential field of view (a) and trajectory of ISS over the field-of-view of a ground station as seen from above (b). The possible duration of communication depends on the minimum elevation angle ε_{min} and the longitudinal shift (Δ_{long}) between the ground station and the space station in its zenith as seen from the ground station; ε_{max} is the corresponding maximum elevation angle. The angle ξ is measured with respect to a line parallel to the equator.

I chose ESA's optical ground station (OGS) on Tenerife as an example for a possible location of the ground terminal. Details about this site can be taken from, e.g., [52]. In Fig. 2.4 numerical values of the link duration as a function of the minimum elevation angle and the longitudinal shift following Eq. (A.7) as derived in Appendix A can be read off for the OGS ($\Psi = 28.3^\circ$).

⁴There are certain simplifications leading to the presented results: The Earth is assumed to be a perfect sphere, the orbit of the ISS is a circle, and the trajectory of the ISS over the ground station is a straight line

⁵The elevation angle for which communication is possible may be restricted by atmospheric conditions or sight obscurations like, e.g., mountains or buildings.

The overall orbit shift is about 25° longitude difference. This will be experienced for some 14% of all the orbits. With 15 orbits per day this results in two links within 24 hours.

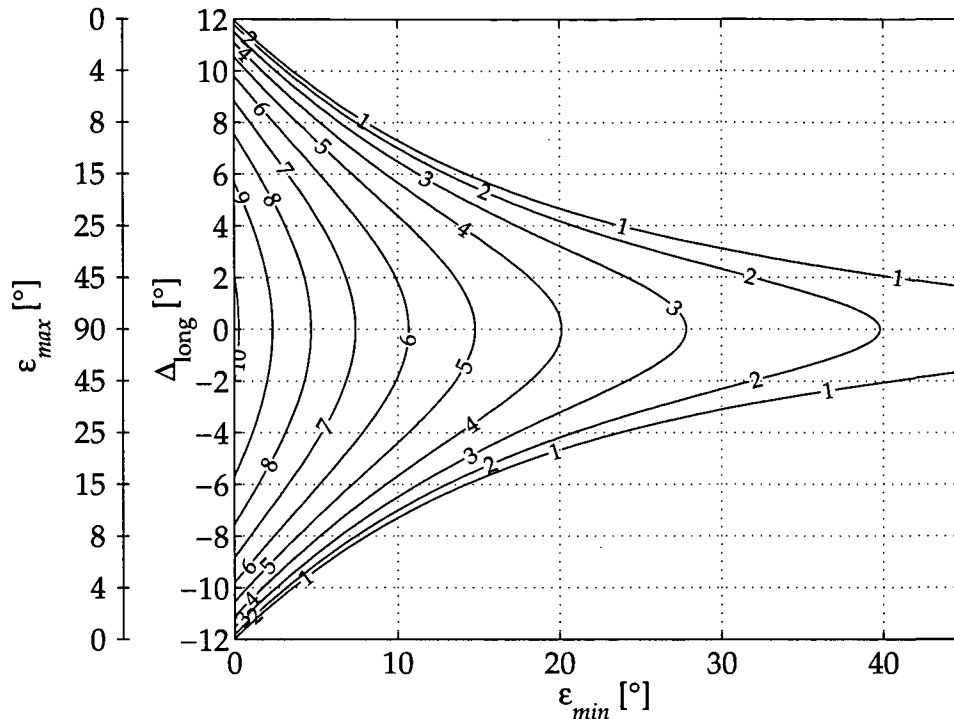


Figure 2.4: Maximum duration T of communication between ISS and the OGS (given in minutes by the numbers inserted along the lines) as a function of the elevation angle and the difference in longitude of the ground station and the satellite when in zenith as seen from the ground station.

2.3 Influence of atmosphere

The Earth's atmosphere extends to approximately 700 km above the surface and consists of several distinct layers. Pronounced density is found only within the lowest 20 km. This is the effective height responsible for distortions of propagating electromagnetic waves. Atmospheric effects on the beam propagation at optical wavelengths can be divided into three categories, namely absorption, scattering, and turbulence [49, 50].

2.3.1 Absorption

Absorption occurs when the optical electromagnetic field transfers energy to the molecular constituents of the atmosphere such as water vapor, carbon dioxide, and ozone. Molecular absorption is rather a line than a band phenomenon. It therefore exhibits a strong dependency on wavelength [49, 53]. Different weather conditions cause variations of the atmospheric absorption by several orders of magnitude. For clear skies some 1-2 dB atmospheric loss have to be expected at $\lambda = 1550$ nm (see Fig. 2.5).

2.3.2 Scattering

Atmospheric scattering due to molecular sized particles is called Rayleigh scattering. For objects large compared to the wavelength, Mie scattering occurs. Rayleigh scattering, being proportional to λ^{-4} , is dominant for short wavelengths, while Mie scattering does not depend on the wavelength that strong [53].

Figure 2.5 represents measurements of the atmospheric transmission including absorption and scattering as a function of wavelength, considering both absorption and scattering [53].

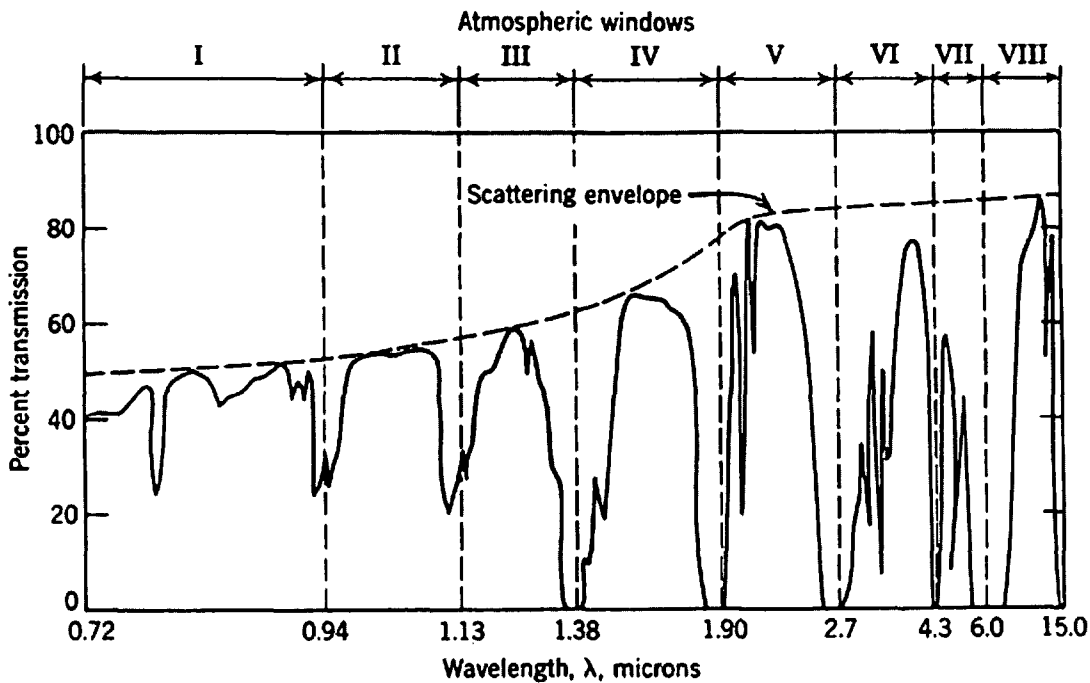


Figure 2.5: Atmospheric transmission as a function of wavelength (from [53]).

2.3.3 Turbulence

Wind blowing over an aerodynamically rough region of the Earth's surface in the presence of a temperature gradient creates fluctuations in the atmosphere's refractive index known as optical turbulence. These changes in the index of refraction cause turbulent eddies, acting as random optical lenses which refract the propagating light. The effect of these lenses is an enlarged divergence, resulting in a reduced amount of signal power collected by the receive telescope and consequently a reduced signal-to-noise ratio (SNR). Other consequences of atmospheric turbulence are wavefront distortions, deteriorating the performance of coherent receivers (cf. Sect. 1.3), and beam wander.

At a certain point \mathcal{R} , the refractive index can be written as

$$n(\mathcal{R}) = n_0 + n_1(\mathcal{R}), \quad (2.3)$$

where n_0 and n_1 are contributions independent and dependent on pressure and temperature, respectively. The actual values of pressure and temperature not only vary spatially within the

beam's diameter but also show a fluctuation in time. The properties of the atmosphere concerning turbulence are often represented by the structure constant $C_n^2(\mathcal{R})$. As a consequence of the statistical fluctuations of the atmosphere's local behavior, the spatial dependence of the structure constant is often reduced to be solely a – time averaged – function of the altitude, $\langle C_n^2(\mathcal{R}) \rangle = C_n^2(h)$, where h is the height above ground. For the *Hufnagel-Valley* (H-V) model, which is often used to obtain numerical approximations of empirically obtained values for $C_n^2(h)$, the only parameters besides the altitude are the so called *pseudo wind speed* v_{pw} and the value of the structure constant on ground $C_{n,0}^2 = C_n^2(0)$ [50]:

$$C_n^2(h) = 0.00594(v_{pw}/27)^2(10^{-5}h)^{10} \exp(-h/1000) + 2.7 \cdot 10^{-16} \exp(-h/1500) + C_{n,0}^2 \exp(-h/100). \quad (2.4)$$

Figure 2.6 shows the structure constant as a function of the altitude for different values of v_{pw} and $C_{n,0}^2$ typical during daytime. For extremely low or high turbulence, the structure constant on ground can become $C_{n,0}^2 = 10^{-17} \text{ m}^{-2/3}$ or $C_{n,0}^2 = 10^{-9} \text{ m}^{-2/3}$, respectively.

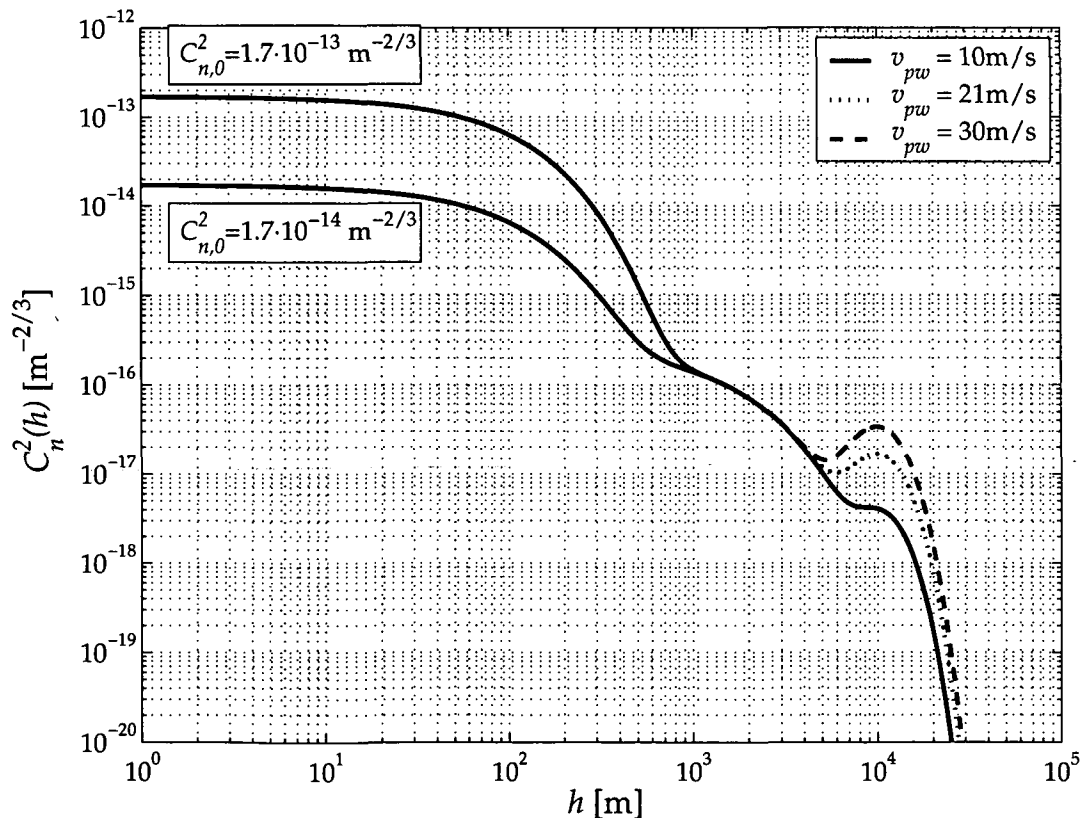


Figure 2.6: Structure constant $C_n^2(h)$ following from the H-V model as a function of the altitude h .

The divergence of optical beams due to atmospheric turbulence can be estimated from the Fried parameter r_0 [54]. This can be interpreted as the aperture which has the same divergence as a diffraction limited aperture in the absence of turbulence. The Fried parameter

is calculated from the structure constant as [55]

$$r_0 = \left[\frac{2.91}{6.88} \left(\frac{2\pi}{\lambda} \right)^2 \int_0^L C_n^2(h) dh \right]^{-3/5} \quad (2.5)$$

with the link distance L and the wavelength λ .

I will assume that the divergence due to turbulence adds quadratic to the divergence of the telescope (cf. following subsection). Recently obtained estimations for the Fried parameter at $\lambda = 1550$ nm, valid for the optical ground station at Tenerife are:

- $r_0 = 20$ mm for strong turbulence,
- $r_0 = 80$ mm for medium turbulence,
- $r_0 = 200$ mm for weak turbulence.

The value for weak turbulence agrees very well with the numerical result obtained from Eqs. (2.4) and (2.5) being $r_0 = 193$ mm for $v_{pw} = 21$ m/s and $C_{n,0}^2 = 1.7 \cdot 10^{-14} \text{ m}^{-2/3}$.

It shall be stated that the impact of turbulence depends on:

- wavelength ($r_0 \propto (\lambda)^{6/5}$),
- elevation angle (affecting the link distance),
- direction of transmission.

The effect of atmospheric turbulence is quite different for a space-to-ground link and a ground-to-space link and this has been called "shower curtain effect". The view from the inside out (from behind the shower curtain) is very much blurred, while the view from the outside in (from some meters away from the shower curtain) is comparatively clear. The same applies for a space-to-ground link, where the light propagates through vacuum for the most of the distance first before being disturbed by the atmosphere, whereas for a ground to space link the beam spreading effects of turbulence take place at the beginning of the propagation, causing strongly enhanced divergence (Fig. 2.7).

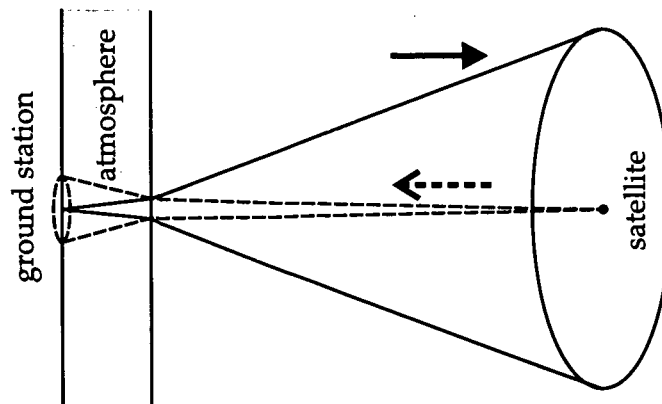


Figure 2.7: Shower curtain effect

2.4 Link attenuation

The *attenuation factor* A can be defined as the ratio of the optical power made available by the transmitter, P_T , to that provided to the receiver's detector, P_R . Figure 2.8 serves to illustrate this definition in case of a free-space link.

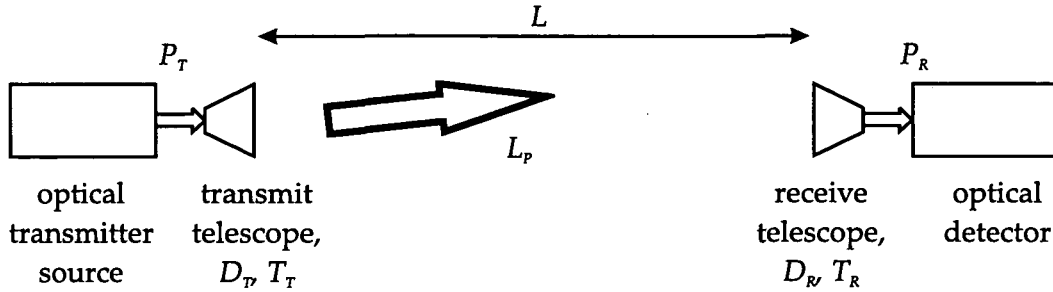


Figure 2.8: Layout of a free-space one-way link.

The attenuation factor $A = P_T/P_R$ is roughly given by

$$A = \frac{L^2 \lambda^2}{D_T^2 D_R^2} \frac{1}{T_T (1 - L_p) T_R} \quad (2.6)$$

where L is the link distance, λ the wavelength, and D_T and D_R the diameters of the transmit and receive telescope. With T_T and T_R I denote the transmission factors (≤ 1) of the telescopes, L_p is the pointing loss due misalignment of transmitter and receiver. This basic relationship applies if

- the receiver is in the transmitter's far field, i.e. $L \geq D_T^2/\lambda$,
- the transmit telescope is diffraction limited,
- there is no influence of the atmosphere.

While Eq. (2.6) applies for space-to-ground links, it is modified for ground-to-space to take into account an additional attenuation of the atmosphere and the influence of turbulence, which can be neglected for space-to-ground links (cf. former section). The diffraction limited divergence caused by the aperture diameter of the transmit telescope is increased when the beam passes turbulent atmosphere, depending on the *Fried parameter*, r_0 , which can be interpreted as an "effective aperture" [54]. As already stated, I assume that the divergence due to turbulence adds quadratic to the divergence of the telescope [56]. The attenuation factor may then be approximated by

$$A = \frac{L^2 (\theta_T^2 + \theta_{atm}^2)}{D_R^2} \frac{1}{T_T (1 - L_p) T_R} 10^{A_{atm}/10}, \quad (2.7)$$

where A_{atm} is the attenuation of the atmosphere, given in [dB]. The divergence angle⁶ resulting from the transmit telescope is assumed to be

$$\theta_T = \frac{\lambda}{D_T} \quad (2.8)$$

⁶The beam divergence angle is defined as the increase in the diameter, measured in rad, of a beam where the irradiance is $1/e^2$ of the peak irradiance.

and the turbulence causes the additional divergence

$$\theta_{atm} = \frac{\lambda}{r_0}. \quad (2.9)$$

Figure 2.9 shows a contour plot of the attenuation factor as a function of the ratio of the receive telescope aperture to the link distance and the transmit telescope aperture for the ground-LEO uplink for 1550 nm. Two additional vertical scales give the link distance for 30 cm receive telescope aperture and the receive telescope aperture for 400 km link distance. The lines of equal attenuation are separated by 5 dB. The corresponding plot for the LEO-ground downlink is shown in Fig. 2.10.

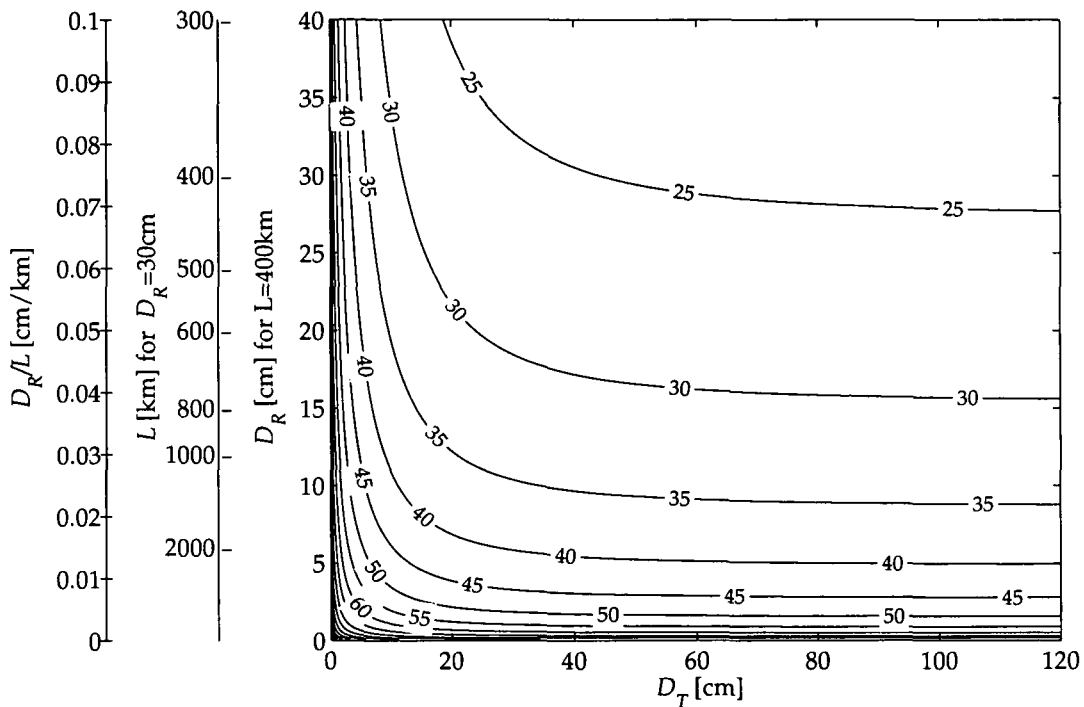


Figure 2.9: Attenuation factor A as a function of the ratio of the receive telescope aperture D_R to the link distance L and the transmit telescope aperture D_T for a ground-LEO uplink.

To obtain the presented results, I assumed an altitude of the ISS of 400 km representing the lower limit of the link distance (cf. 2.2).

The baseline for the ground aperture is 1 m, because this is the telescope diameter of the OGS. Telescopes with a diameter of 20 to 30 cm are small and light enough to be operated on-board a space platform. Larger telescopes are feasible, whereas expensive and more difficult to handle.

I assume the transmission factor of the involved telescopes to be $T_T = T_R = 0.8$ and the pointing loss to be $L_P = 0.2$, representing typical values. The assumption of an atmospheric attenuation of $A_{atm} = 1$ dB applies for excellent seeing conditions (no haze, fog, or clouds) and is valid only in certain wavelength regions. Following the intention to cover favorite scenario conditions, the calculations are performed for weak turbulence, $r_0 = 200$ mm.

Due to the turbulence the attenuation for the uplink is considerably worse than for the downlink. Another consequence of the turbulence is that increasing the transmitter aperture

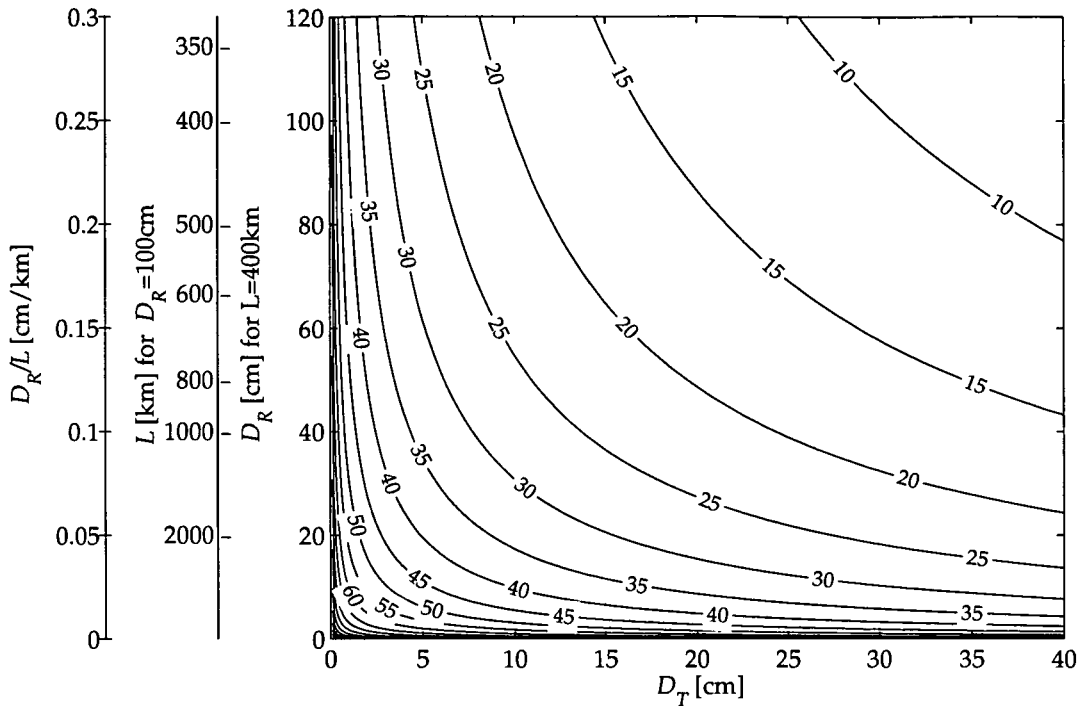


Figure 2.10: As Fig. 2.9 but for LEO-ground downlink.

for the uplink beyond 60 cm has almost no effect on the attenuation factor.

Compared to the values presented in [57], the divergence obtained with my model is lower by a factor of 1.5. (However I do not know the exact turbulence conditions assumed in [57].) Also, the ARTEMIS - OGS downlink experimental results are slightly worse than my calculations would predict [58]. I am aware of the fact that I probably underestimate the turbulence effect, but I will use my model to calculate a lower-bound estimation for the attenuation factor.

2.5 Background radiation

The receiver not only detects the signal from the transmitter but also unwanted light from celestial bodies. This may have a degrading effect on system performance. The spectral radiance (the unpolarized radiant power into a angle increment per unit area of source and unit wavelength, given in $[W/m^2m\ sr]$), from a self-emitting source at temperature T is described by Plank's law [53, 59]:

$$N(\lambda) = \frac{2hc^2}{\lambda^5 [e^{hc/\lambda kT} - 1]}, \quad (2.10)$$

where λ is the wavelength, c is the speed of light, while h and k are Planck's and Boltzmann's constant. Figure 2.11 shows the spectral radiance as a function of the wavelength for several temperatures and its maximum as depending on the temperature, following $N_{\lambda_{max}}(T) = 4.1 \cdot 10^{-6} T^5 W/m^2m\ sr K^5$.

The major source of background radiation is the Sun, either when looking directly into it, or through reflected sunlight from other objects like planets, the Moon and also the ISS. For

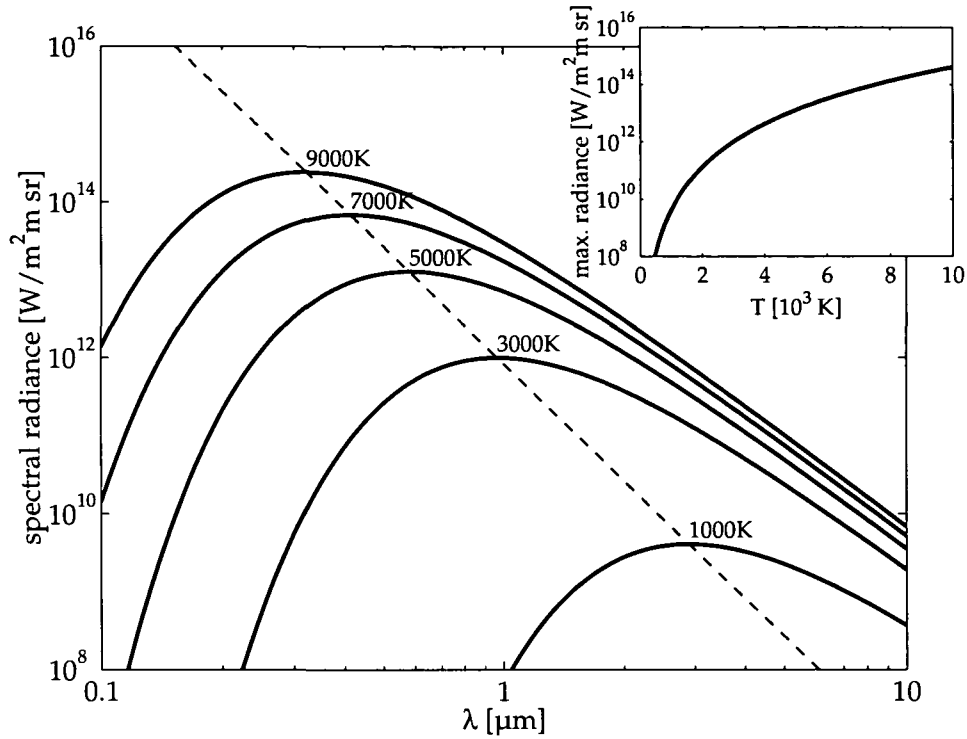


Figure 2.11: *Blackbody spectral radiance. The dashed line represents Wien's displacement law $T\lambda_{max} = 2898 \text{ K}\mu\text{m}$. The inset shows the maximum of the spectral radiance as a function of the temperature.*

ground-based receivers, a certain amount of background radiance has to be expected from the sky due to scattered sunlight [53].

By employing the definition of the spectral radiance, the power spectral density accepted by the receiver's telescope⁷ originating from a radiating body yields

$$N_{back}(\lambda) = A_{eff}\Omega_R\mathcal{N}(\lambda) \quad [\text{W/m}] \quad (2.11)$$

depending on $\Omega_R = D_R^2\pi/4R^2$, the solid angle subtended by the receiver at the source (with D_R is the receive telescope diameter, and R the distance between the receiver and the radiation source), and A_{eff} the area of the source as seen from the receiver.

If the source appears bigger than the receiver FOV, i.e., $\Omega_S > \Omega_{FOV}$ ⁸ (cf. Fig. 2.12 (a)) the effective area is

$$A_{eff} = \frac{\pi\theta_{FOV}^2R^2}{4}, \quad (2.12)$$

⁷To directly compare the power resulting from background radiation with the signal power from the transmitter reduced by the attenuation as defined in Eq. (2.7), the atmospheric attenuation and the receive telescope have to be considered, i.e. the results presented in this subsection have to be multiplied by the factor $T_R T_A$ (cf. former section).

⁸The solid angle subtended by the source at the receiver is $\Omega_S = D_S^2\pi/4R^2$, where D_S is the diameter of the source. The receiver field-of-view reads $\Omega_{FOV} = \pi\theta_{FOV}^2/4$, where θ_{FOV} is the planar angle of the receiver FOV.

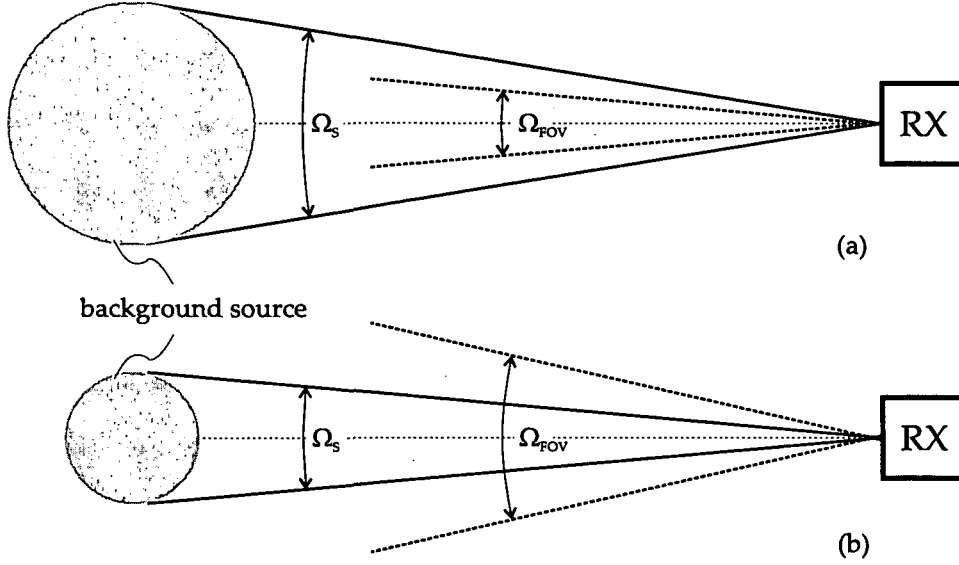


Figure 2.12: Background source and receiver. Ω_S is the angle subtended by the source at the receiver and Ω_{FOV} is the receiver's field of view. (a) $\Omega_S > \Omega_{FOV}$, (b) $\Omega_S < \Omega_{FOV}$.

leading to⁹

$$N_{back}(\lambda) = \left(\frac{\theta_{FOV}}{\theta_{DL}} \right)^2 \lambda^2 \mathcal{N}(\lambda) = \frac{\Omega_{FOV}}{\Omega_{DL}} \lambda^2 \mathcal{N}(\lambda), \quad (2.13)$$

while for $\Omega_S < \Omega_{FOV}$ (cf. Fig. 2.12 (b))

$$A_{eff} = \frac{D_S^2 \pi}{4}, \quad (2.14)$$

leading to

$$N_{back}(\lambda) = A_{rec} \Omega_S \mathcal{N}(\lambda) = \frac{\Omega_S}{\Omega_{DL}} \lambda^2 \mathcal{N}(\lambda), \quad (2.15)$$

where D_S is the diameter of the radiation source and $A_{rec} = D_R^2 \pi / 4$ is the receiver's area.

With the definitions of the number of spatial modes [61]

$$m = \frac{\Omega_{FOV}}{\Omega_{DL}} \quad \text{for } \Omega_S > \Omega_{FOV} \quad (2.16)$$

and

$$m = \frac{\Omega_S}{\Omega_{DL}} \quad \text{for } \Omega_S < \Omega_{FOV}, \quad (2.17)$$

respectively, the power spectral density is

$$N_{back}(\lambda) = m \lambda^2 \mathcal{N}(\lambda). \quad (2.18)$$

The power spectral density per frequency unit, given in [W/Hz], reads

$$N_{back}(f) = N_{back}(\lambda) \frac{\lambda^2}{c} = m \frac{\lambda^4}{c} \mathcal{N}(\lambda). \quad (2.19)$$

⁹The diffraction limited FOV is $\theta_{DL} = 4\lambda / (\pi D_R)$ [60].

2.5.1 Radiation from celestial bodies and ISS

For radiation caused by self emission (e.g. stars) and by reflected sunlight (e.g. ISS, Moon, planets), it is customary to define the spectral irradiance (radiant power incident upon a surface per unit surface area and unit wavelength) since the actual or projected area of the source is not generally known, especially for stars. The spectral irradiance is related to the spectral radiance by [53]

$$\mathcal{H}(\lambda) = \mathcal{N}(\lambda)\Omega_S \quad [\text{W}/\text{m}^2\text{m}]. \quad (2.20)$$

By applying this definition, Eq. (2.19) is modified to express the background power spectral density as a function of the spectral irradiance,

$$N_{back}(f) = m \frac{\lambda^4}{c} \frac{\mathcal{H}(\lambda)}{\Omega_S} = \begin{cases} \Omega_{FOV} R^2 \frac{D_S^2}{D_s^2} \frac{\lambda^2}{c} \mathcal{H}(\lambda) & : \Omega_S > \Omega_{FOV} \\ \frac{D_S^2 \pi}{4} \frac{\lambda^2}{c} \mathcal{H}(\lambda) & : \Omega_S < \Omega_{FOV} \end{cases} \quad (2.21)$$

The spectral irradiance can be calculated with [61, 62]

$$\mathcal{H}(\lambda) = \mathcal{H}_{peak}(M, T_{eff}) \frac{\mathcal{N}(\lambda)}{\mathcal{N}_{\lambda max}(T_{eff})} = \mathcal{H}_{peak}(M, T_{eff}) \frac{2.9 \cdot 10^{-11} \text{m}^5 \text{K}^5}{(\lambda T_{eff})^5 [e^{hc/\lambda k T_{eff}} - 1]}. \quad (2.22)$$

The maximum value of $\mathcal{H}(\lambda)$ concerning wavelength is denoted by $\mathcal{H}_{peak}(M, T_{eff})$. It depends on the *magnitude*¹⁰ M and the effective temperature of the object T_{eff} . For self-emitting objects this is the temperature of the object; for objects reflecting the light of a star, T_{eff} is the temperature of this star. The maximum spectral irradiance is calculated as [62]

$$\mathcal{H}_{peak}(M, T_{eff}) = I_0 \cdot 10^{-M/2.5} \mathcal{N}_{\lambda max}(T_{eff}) \left(\int_{0.51 \mu\text{m}}^{0.61 \mu\text{m}} \mathcal{N}(\lambda, T_{eff}) d\lambda \right)^{-1}, \quad (2.23)$$

with $I_0 = 3.1 \cdot 10^{-9} \text{W}/\text{m}^2$, the *reference visible irradiance* [62]. The resulting peak spectral irradiance is shown in Fig. 2.13 as a function of the effective temperature for different magnitudes.

For self emission of the planets and the Moon, Eq. (2.20) has to be modified, because these objects are assumed to radiate as grey bodies rather than black bodies. The spectral irradiance then becomes [62]

$$\mathcal{H}(\lambda) = (1 - A)\Omega_S \mathcal{N}(\lambda, T_{se}). \quad (2.24)$$

Here, A is the ratio of the amount of electromagnetic radiation reflected by the body to the amount incident upon it, the *albedo* [63], and T_{se} is its effective surface temperature for self emission.

Figure 2.14 shows the spectral irradiance for the brightest celestial bodies and the ISS. The parameters used to obtain the presented results are given in Tab. 2.1. For Moon and Venus both self emission and reflectance are taken into account, which means that the irradiance resulting from Eq. (2.24) and Eq. (2.22) are summarized. The spectral irradiance then experiences two maxima, one for sun reflectance and one for self emission, at lower and higher wavelengths, respectively. For the wavelength considered here, self emission has a negligible influence. For the other objects, only Eq. (2.22) applies.

The power spectral density per frequency unit following Eq. (2.21) is shown in Fig. 2.15 for the brightest objects in the sky and the ISS for the diffraction limited case $\theta_{FOV} = \theta_{DL}$. Using the parameters given in Tab. 2.1, the case $\Omega_S > \Omega_{FOV}$ applies for all bodies but for the Sirius, when considering reasonable telescope diameters.

¹⁰The brightness of an object relative to a reference star is called its *magnitude* M , which has dimension 1.

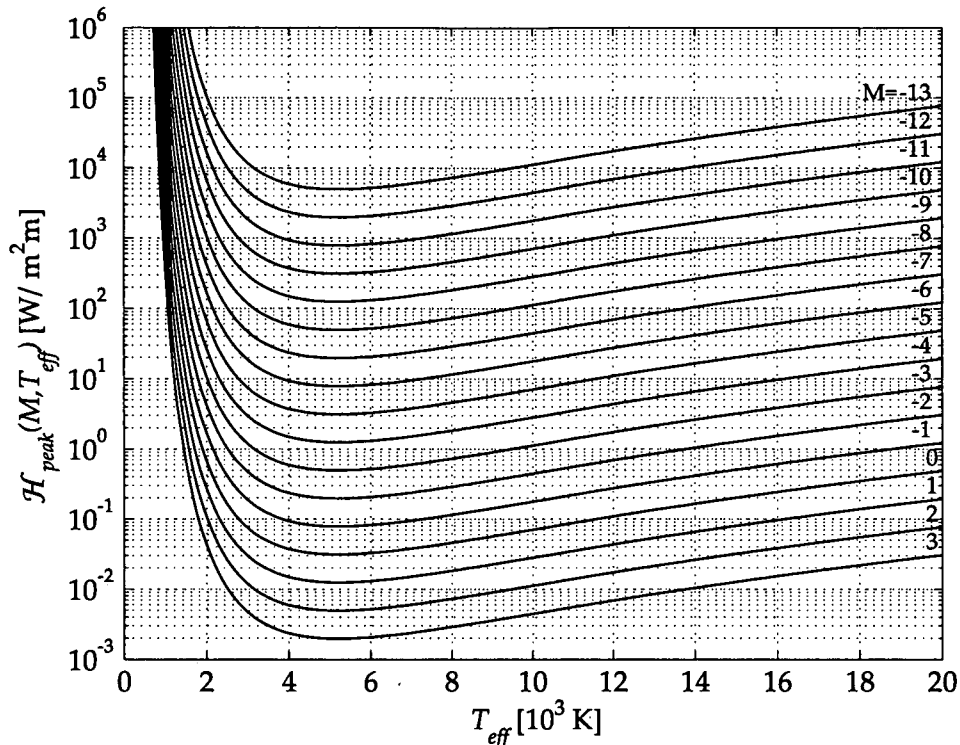


Figure 2.13: Peak spectral irradiance $\mathcal{H}_{peak}(M, T_{eff})$ for different values of the magnitude versus effective temperature.

	T_{eff} [K]	R [km]	D_S [km]	M	\mathcal{H}_{peak} [W/m ² m]	T_{se} [K]	A —
Sun	5 900	$149.597 \cdot 10^6$	$1.392 \cdot 10^6$	4.8	—	5 900	—
Moon ^a	5 900	384 400	3 468	-12.7	$3.896 \cdot 10^3$	400	0.072
Venus ^b	5 900	$41.4 \cdot 10^6$	12 104	-4.4	1.67	330	0.76
Sirius ^c	11 000	—	—	-1.44	0.122	11 000	—
ISS ^d	5 900	800	0.1	+1.5	0.39	—	—
ISS ^e	5 900	800	0.1	-2.7	$8.14 \cdot 10^{-3}$	—	—

Table 2.1: Parameters for the calculation of spectral irradiance for different celestial bodies. Values taken from [62, 64–67].

^afull moon

^bat brightest

^cbrightest star

^dminimum illumination

^emaximum illumination

2.5.2 Radiation from Earth

Downlink

An unavoidable source of background radiation in the downlink case is the spectral radiance caused by the atmosphere. Measured spectral radiance as a function of the wavelength for

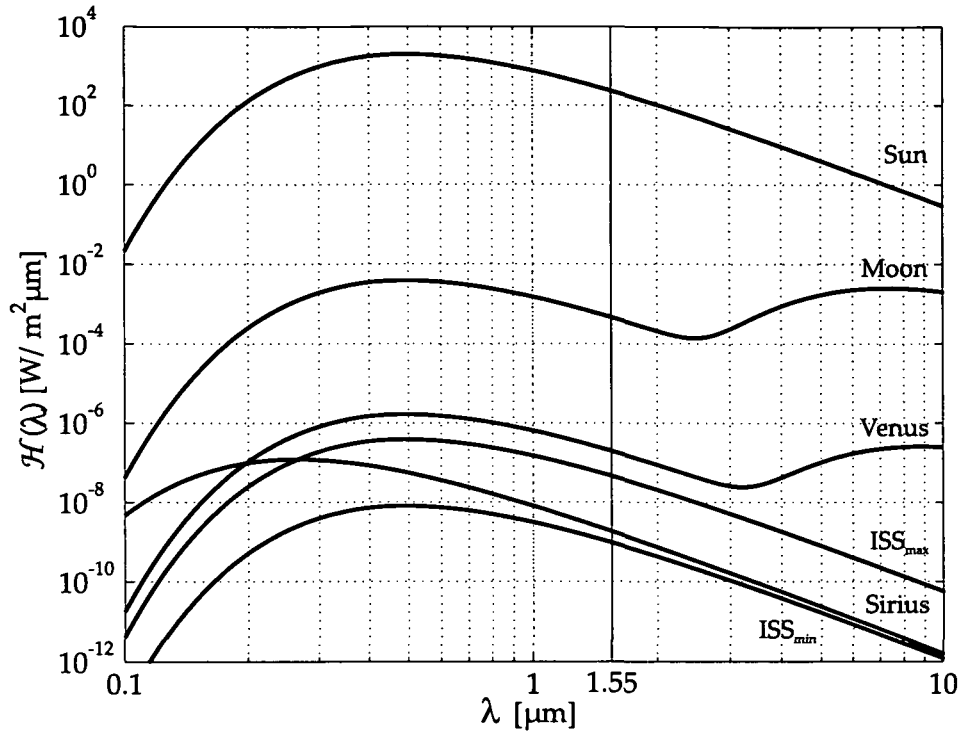


Figure 2.14: Spectral irradiance $\mathcal{H}(\lambda)$ for different celestial bodies and the ISS.

clear sky is given in [53], Fig. 6-6. Since the Earth's atmosphere represents a source extending over the whole hemisphere, Eq. (2.13) applies, independent of the telescope size. Corresponding values of the power spectral density for certain wavelengths are presented in Fig. 2.15. For sunlit clouds, the radiance has to be expected to be an order of magnitude higher than the values presented. At the wavelength of 1 550 nm, communication is practically impossible for clouded skies because of intolerably high attenuation, anyway [49].

During nighttime, sky radiance from zenith caused by zodiacal light, galactic light, and scattered starlight can be approximated by

$$\mathcal{N}(\lambda) = \mathcal{N}_{peak} \frac{2.9 \cdot 10^{-11} \text{ m}^5 \text{ K}^5}{(\lambda T_{eff})^5 [e^{hc/\lambda k_B T_{eff}} - 1]}, \quad (2.25)$$

where $\mathcal{N}_{peak} = 2.9 \text{ W/m}^2 \text{ m sr}$ and $T_{eff} = 6 170 \text{ K}$ were obtained from [53], Fig. 6-7. The resulting power spectral density is given in Fig. 2.15, representing the ultimate lower limit of background radiation.

Uplink

Since the orbit of the ISS is low and the telescope will always be pointed more or less in nadir direction (i.e. downwards), the only source of background radiation is the earth. It's power spectral density again results from Eq. (2.25). The parameters $\mathcal{N}_{peak} = 4.52 \cdot 10^7 \text{ W/m}^2 \text{ m sr}$ and $T_{eff} = 5 400 \text{ K}$ were extracted from [53], Fig. 6-11. The power spectral density as a function of the wavelength is included in Fig. 2.15 ("Earth").

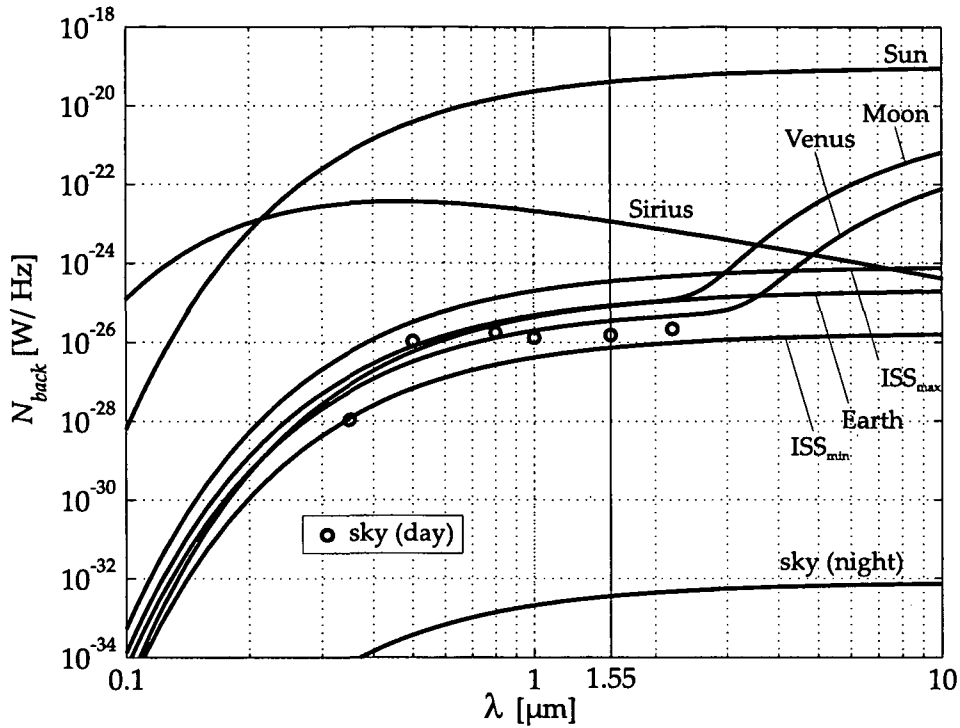


Figure 2.15: Power spectral density N_{back} for different celestial bodies, the sky during day and night, and the ISS received by a diffraction limited telescope.

It is interesting that the two major background radiation sources, the ISS and the Earth for downlink and uplink, respectively are of the same order of magnitude. In Tab. 2.2, the values of the power spectral density for $\lambda = 1550$ nm are given explicitly. The presented numbers however, apply only for diffraction limited FOV.

	N_{back} [W/Hz]
Sun	$4.1 \cdot 10^{-20}$
Sirius	$1.2 \cdot 10^{-23}$
ISS (max)	$3.5 \cdot 10^{-25}$
Earth	$8.3 \cdot 10^{-26}$
Moon	$8.6 \cdot 10^{-26}$
Venus	$3.5 \cdot 10^{-26}$
sky (day)	$1.5 \cdot 10^{-26}$
ISS (min)	$7.3 \cdot 10^{-27}$
sky (night)	$3.6 \cdot 10^{-33}$

Table 2.2: Calculated values of the power spectral density for $\lambda = 1550$ nm.

Chapter 3

Pointing, Acquisition & Tracking

Probably one of the most demanding parts of an optical free space laser communication system is the pointing, acquisition and tracking (PAT) subsystem. Of these three, acquisition is generally considered to be the most difficult [68, 69]. Figure 3.1 gives a schematic overview of a typical opto-mechanical system needed for PAT.

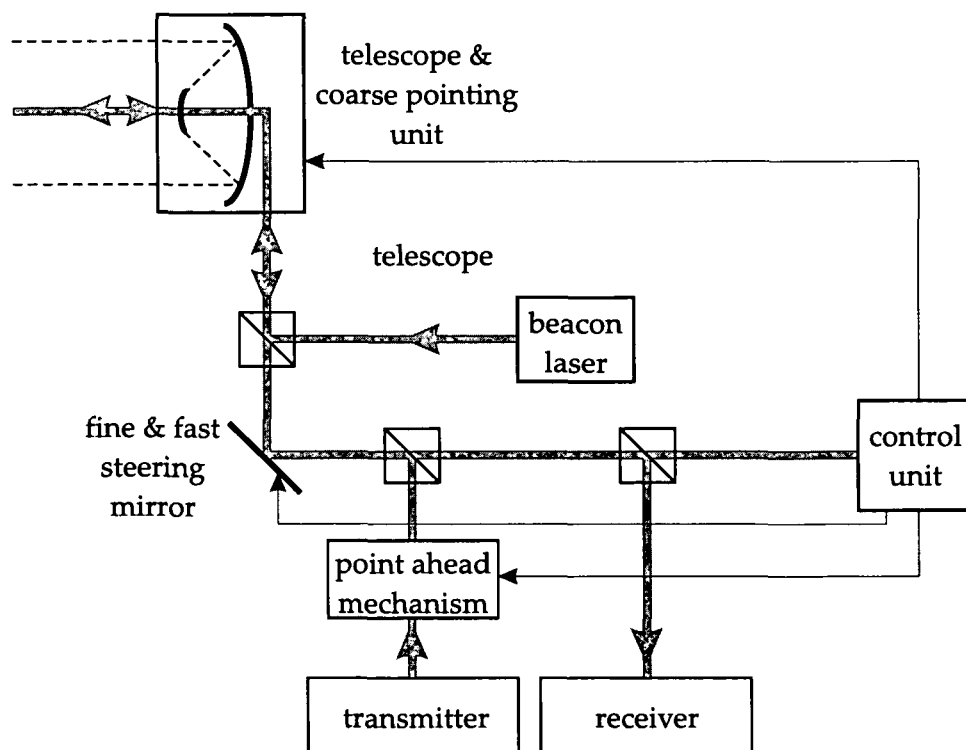


Figure 3.1: Example for a opto-mechanical system possibly implemented in a free space laser communication terminal [12].

3.1 Pointing

To precisely point its transmit beam, each terminal needs knowledge of the exact position of its counterpart. A rough estimate of this information will be calculated from the orbit parameters of the satellite. The terminal points towards the assumed position of its partner either by employing a pointing unit moving the whole telescope with a two-axis gimbal or applying a coarse pointing mirror (as indicated in Fig. 3.1). Then a beacon is activated by one or both of the terminals, providing the direction to point to before the communication signal is active. Tracking the beacon or the communication laser allows the fast steering mirror to follow the exact position of the other terminal.

To compensate for the pointing error caused by the finite speed of light and the relative velocity of the two terminals, a point-ahead angle is applied to direct the transmit beam where the partner terminal will be after the transit time (cf. Sect. 3.4). An equivalent method is to use a look-behind-off-set at the receiver [12].

3.2 Acquisition

The problem of acquisition is that usually the diameter of the beacon laser beam at the receiving terminal is much smaller than the uncertainty area of coarse pointing. This uncertainty is caused by several effects, e.g. atmospheric disturbances, attitude control errors, mechanical resonances from servos, momentum wheel movements, control jet firing, etc.

The two general approaches for acquisition are serial and parallel. For serial acquisition a narrow beam is used to scan the uncertainty area, while the receiver also scans the uncertainty region with a narrow field-of-view (FOV). For parallel acquisition, the whole uncertainty area is illuminated at once while the receiver checks the position of the transmitter with several detector elements [12]. While the serial procedure is time-consuming the parallel strategy requires high power at the transmitter and high complexity at the receiver. Acquisition should not take more than a few seconds [12] and should not ask for extensive extra hardware. There are acquisition techniques that combine serial and parallel scanning.

As an example I will present the acquisition sequence between ARTEMIS (GEO) and OGS (ground) within the SILEX system (see Fig. 3.2). ARTEMIS emits a beacon which scans the uncertainty region, providing sufficient optical energy at every possible location within the region. The OGS provides a field of view wide enough to make sure that the satellite is within it. When the scanning beacon reaches a position in which the power detected in the receiver's sensor exceeds a certain value, the uplink beam is pointed in that direction. When the GEO satellite detects the signal, it stops the scan and tries to lock its tracking loop on it. Once this initial signal acquisition is successful, both terminals try to keep the incoming signals as close as possible to the center of their respective tracking sensors (cf. following section) [70].

Generally, one or more separate lasers, operating at wavelengths differing from that of the communication laser are used to generate the beacon. It is, however, also possible to use the communication signal as beacon.

3.3 Tracking

Once the acquisition sequence is completed successfully, the terminal will make a transition into coarse tracking and finally into fine tracking mode. Coarse tracking is performed by a

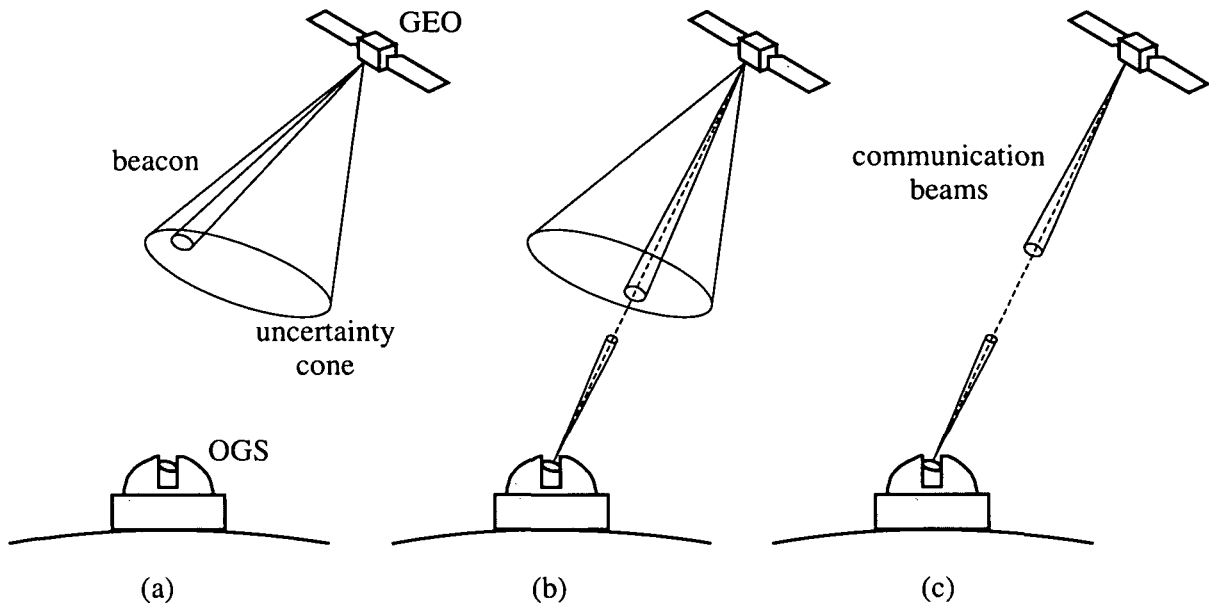


Figure 3.2: Acquisition sequence of the SILEX system: scanning (a), acquisition (b), and communication with tracking (c).

control loop (bandwidth ~ 10 Hz) driving the coarse pointing mirror. The fine tracking loop controlling the fine steering mirror (see Fig. 3.1) should have a bandwidth of ~ 1 kHz [12]. The tracking function measures the angular error between the direction of the incoming and outgoing beams¹. The difference is used as feedback for mirror pointing [71]. Mainly two forms of angle error sensors are considered: CCD-arrays and quadrant photo diodes (QPD). Sometimes CCDs are employed for coarse tracking and QPDs for fine tracking because the former offer a wider FOV and the latter are more accurate [6]. The tracking error has high impact on the link attenuation.

Depending on the scenario, the relative velocity of the terminals can reach high values. One critical issue is the maximum angular speed the tracking subsystem is capable to follow. This problem mainly concerns the coarse pointing mirror since the fast steering mirror only compensates for minor pointing errors (e.g. vibrations of the platform). Following information provided by *Contraves Space*, the maximum mutual angular speed of the terminals ranges from $0.02^\circ/\text{s}$ for a GEO-GEO link to $1.5^\circ/\text{s}$ for a LEO-ground scenario [72].

3.4 Point ahead angle

When establishing a link between two distant, fast moving terminals, a certain offset between the pointing direction for reception and transmission has to be maintained. This offset is referred to as point ahead angle (PAA). The received signal in Terminal 1 at timestamp t will come from where Terminal 2 was at timestamp $t - \Delta T$, while the transmission beam has to be pointed to where Terminal 2 will be at $t + \Delta T$ when ΔT is the time it takes the light to travel

¹A – calculated – point ahead angle has to be considered in the tracking control unit (cf. Sect. 3.4).

from Terminal 1 to Terminal 2. The resulting point ahead angle is

$$\delta = \frac{v2\Delta T}{L} = 2\frac{v}{c'} \quad (3.1)$$

where L is the distance² and v is the velocity component of the terminals perpendicular to the line of sight between the two terminals (see Fig. 3.3).

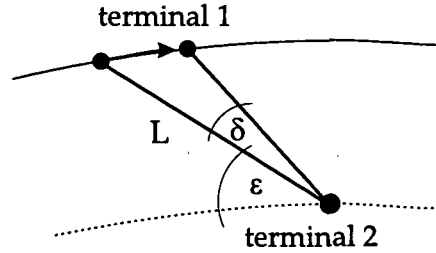


Figure 3.3: Point ahead angle.

I now want to determine v for a space-to-ground link: When considering that both terminals are in motion, the relative velocity is the difference of the velocity components perpendicular to the line of sight between the two terminals

$$v = v_s - v_g. \quad (3.2)$$

The velocity component of the space terminal perpendicular to the line of sight is

$$v_s = \omega_s(r_E + h) \cos \gamma = \omega_s(r_E + h) \sqrt{1 - \left(\frac{r_E}{r_E + h} \cos \varepsilon\right)^2}, \quad (3.3)$$

where γ is defined in Fig. 2.1, ε is the elevation angle, h is the altitude of the satellite, r_E is the radius of the Earth, and ω_s is the satellite's angular velocity $2\pi/T_{rev}$. For the ISS, the duration of one revolution is $T_{rev} = 5520$ s. With simple trigonometric calculations, the ground station's velocity perpendicular to the line of sight to the satellite reads

$$v_g = \omega_E r_E \cos \Psi \cos \xi \sin \varepsilon = \omega_E r_E \cos \Psi \cos \left(\phi_i \cos \left(\frac{\Psi}{\phi_i} \frac{\pi}{2}\right)\right) \sin \varepsilon, \quad (3.4)$$

with the angular speed of a point on the surface of the Earth $\omega_E = 2\pi/86400$ s, the stations latitude Ψ and the angle ξ as defined in Eq. (A.2)³.

The PAA as a function of the elevation angle is presented in Fig. 3.4 for the link scenario from ISS to OGS. In contrary to the link duration calculations, the influence of the ground station's geographical position is low.

For space-to-ground links, where the divergence can be expected to be in the range of $10 \mu\text{rad}$ (for $\lambda = 1550$ nm and $D_T = 15$ cm) and atmospheric turbulence has negligible influence (cf. Sect. 2.3), the point ahead angle is an important issue. For ground-to-space links turbulence may widen the laser beam to an extent that the beam divergence is larger than the PAA and a compensation becomes superfluous.

²To simplify matters, it is assumed that the variation of the distance and elevation angle during ΔT is negligible. Therefore Eq. (3.1) is only valid for small point ahead angles.

³The inclination angle of the ISS is $\phi_i = 51.6$ deg

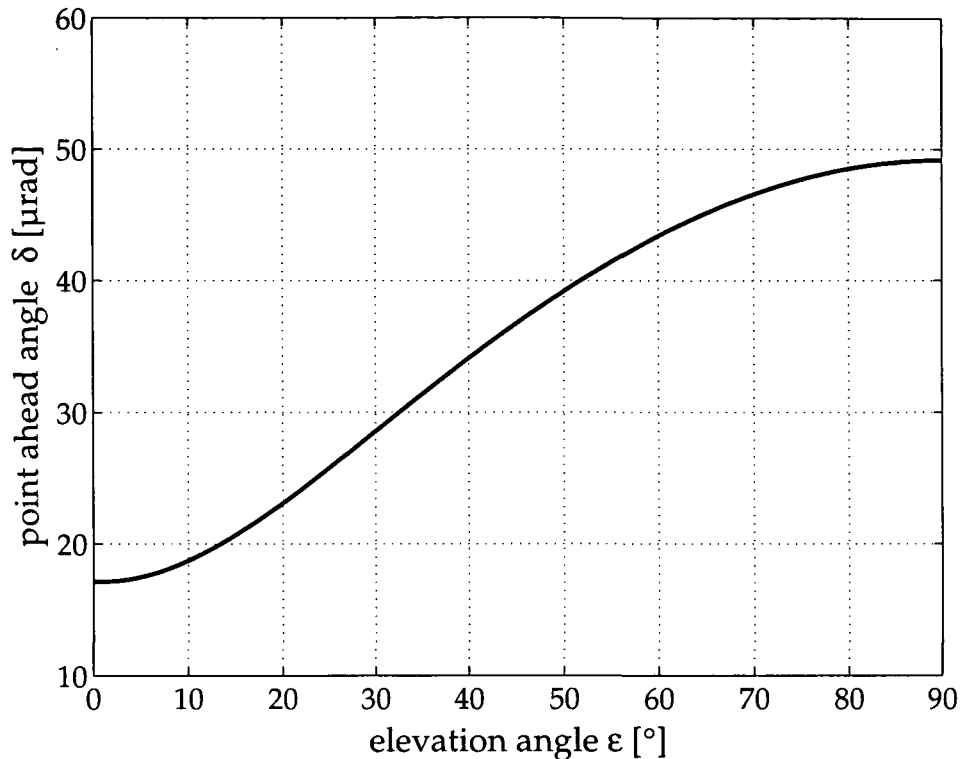


Figure 3.4: Point ahead angle as a function of elevation for ISS to OGS link.

3.5 Pointing accuracy – choice of the telescope size

When designing an optical free space communication system, the size of the telescope for both the ground and space terminal is one of the key parameters.

Considering the results presented in Fig. 2.9 or 2.10, a large telescope diameter seems desirable. However, big telescopes are not only expensive to produce and launch, they additionally result in a small divergence angle of the emitted beam. This effect, though responsible for the low link attenuation, leads to high demands on the pointing accuracy.

When assuming that the maximum affordable pointing error is, e.g., half the full divergence angle $\theta_T = \lambda/D_T$ the link attenuation is approximately increased by a factor of e^2 corresponding to some 8.7 dB, i.e. the pointing loss from Sect. 2.4 reads $L_P = 1 - e^{-2} = 0.86$. Following Eq. (2.7) the attenuation factor for diffraction limited performance due to this pointing error calculates

$$A = \left(\frac{L\lambda e}{D_R D_T} \right)^2 = \left(\frac{L\theta_T e}{D_R} \right)^2, \quad (3.5)$$

where L is the link distance, λ is the laser wavelength, D_R and D_T are receive and transmit telescope diameters, respectively, and e is Euler's constant. In contrary to Eq. (2.7) all effects but beam divergence and pointing error are neglected, namely $T_R = T_T = 1$ and $A_{atm} = 0$. The maximum pointing error, α , can then be expressed as

$$\alpha = \theta_T/2 = \frac{D_R \sqrt{A}}{2Le}. \quad (3.6)$$

Figure 3.5 illustrates the tradeoff between attenuation and maximum allowable pointing error, resulting in the choice of a telescope diameter suitable for the system requirements for $L = 400$ km. The figure is to be used as follows (for the examples I use the scale corresponding to a receive telescope diameter of $D_R = 10$ cm): When, on one hand, the pointing accuracy of the PAT system is not better than, e.g., $4 \mu\text{rad}$, it can be read off from the graph that the transmit telescope diameter must not be larger than 20 cm, resulting in a link attenuation of at least 38 dB. If, on the other hand, the maximum attenuation were, e.g., 35 dB (because of limited transmit laser power or weak receiver sensitivity), the telescope has to be larger than 30 cm in diameter, asking for a pointing accuracy better than $2.5 \mu\text{rad}$.

The system has to be designed in such a way that the maximum attenuation and the affordable pointing error correspond to a point located in the safe-to-operate region of Fig. 3.5, which is the shaded area below the solid line. When this is provided, the telescope diameter can be chosen within a range according to the top horizontal and right vertical scale (e.g. $D_R = 10$ cm, $\alpha = 4 \mu\text{rad}$, $A = 49$ dB $\Rightarrow 6 \text{ cm} \leq D_T \leq 20$ cm).

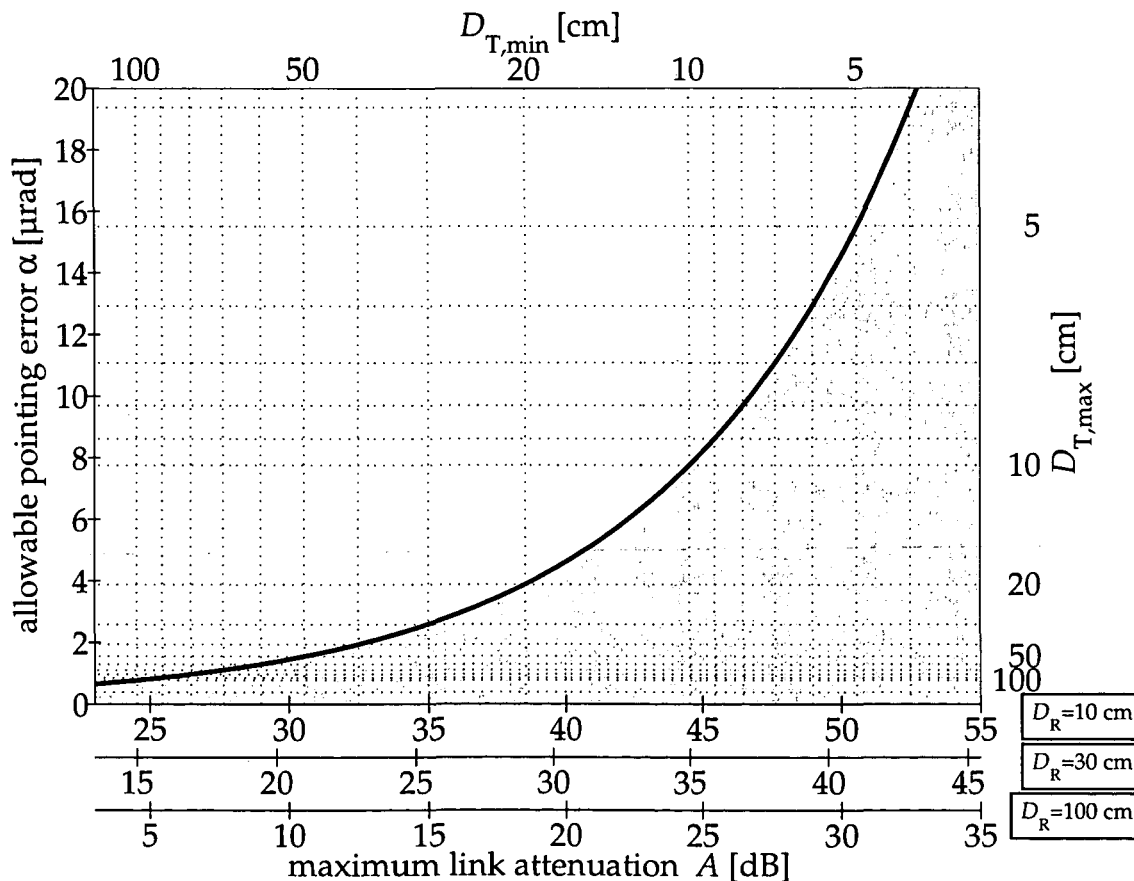


Figure 3.5: Tradeoff between maximum affordable attenuation and pointing error for different receive telescope diameters and a link distance of $L = 400$ km at a wavelength of $\lambda = 1550$ nm. The shaded area represents the safe-to-operate region, where a transmit telescope diameter D_T can be found meeting both criteria.

It is appropriate to use a large telescope at the ground station leaving the system designer a free hand to choose the telescope for the space element as small as possible. In general, the pointing accuracy can be made higher on ground. The fine pointing mirror of the OGS has an accuracy of 0.05 arcsec, corresponding to $0.24 \mu\text{rad}$ [73]. The telescope diameter is 1 m. Even for a 10 cm telescope at the space terminal, the attenuation will be below 25 dB, while a pointing error of some $8 \mu\text{rad}$ can be afforded. Unfortunately, the most accurate nadir pointing instrument onboard the ISS, the HEXAPOD, has a pointing error as large as ± 90 arcsec (± 26.2 mrad) [1]. However, the planned Japanese LCDE terminal is designed to have a pointing and tracking accuracy of better than $1 \mu\text{rad}$ [6].

3.6 Adaptive optics

The effect of atmospheric turbulence mentioned in Sect. 2.3 results in wavefront distortions of the optical beam. This leads to higher beam divergence and consequently to an increased link attenuation (cf. Eqs. (2.7) and (2.9) in Sect. 2.4).

For astronomic applications, or single-mode fiber coupling where wavefront distortions are especially harmful, this problem can be overcome by employing *adaptive optics* [74,75]. A deformable mirror, placed between the telescope and the detector, is used to compensate for these distortions. The mirror is usually deformed by piezoelectric actuators. Depending on the size of the telescope and the desired accuracy, the number of actuators and the resulting calculational effort can be considerable.

To compensate the wavefront distortion, it has to be measured first. This is done by detecting the light of "guide stars", either natural or artificially generated by a laser beam. The obtained data is fed into a control loop and the mirror is adapted in real time.

While adaptive optics is used in most of the large astronomic telescopes, I know of only one example where it is considered to improve the link properties of an optical free-space communication terminal. The ground segment of the Japanese LCDE terminal, a 1.5 m telescope located in Tokyo, is planned to be equipped with a 13-element bimorph mirror [76].

Adaptive optics is very sophisticated and envisaging a setup as simple as possible, I will surmise that the system under investigation is not equipped with this technology.

Chapter 4

Receiver Sensitivity

Following the assessment in Sect. 1.3, I am going to focus on optically preamplified direct detection receivers in combination with on-off-keying data modulation. The most important issue for free-space applications is to optimally exploit the power provided by the receiver in order to achieve a certain bit error probability (e.g. $\text{BEP} = 10^{-9}$). The limited power available aboard a space platform together with the high link attenuations ask for a high sensitivity of the receiver.

The influence of several parameters on the receiver sensitivity are investigated in the following chapter. I will present a system model for an optically preamplified direct detection receiver including detailed treatment of the noise statistics, corresponding simulation results, and measurements verifying the theoretical and computational findings. The transmitter setup is discussed elsewhere [77,78].

4.1 System setup

Besides the high achievable sensitivity, one of the major reasons to opt for an optically preamplified direct detection receiver is the possibility of employing components developed for fiber communication systems. Consequently, all parts of the receiver are assumed to be single-mode (SM) fiber-coupled.

The optical power collected by the receive telescope comprises the communication signal, noise from the transmitter (usually mainly from the booster amplifier) and noise originating from background radiation. After passing the optical free-space subsystem, schematically shown in Fig. 3.1, the input signal is coupled into a SM fiber. Ideally, the SM fiber serves as a spatial filter, reducing the incoherent noise while leaving the signal unaffected. The theoretically achievable coupling efficiency is 78% [35]. The system discussed within this chapter is represented by the box named “receiver” in Fig. 3.1.

Figure 4.1 shows the setup of an optically preamplified direct detection receiver. The fiber-coupled input signal (optical power $p(t)$) is amplified by a low-noise, high gain fiber amplifier (gain G_p , noise figure F_p). An optical bandpass (transfer function $B(f)$) is implemented to suppress noise not within the signal bandwidth. A polarization filter may be applied to additionally reduce the incoherent noise by a factor of two while leaving the signal unaffected, when the state of polarization (SOP) of the communication signal is well defined. If transmitted and received signal are at different states of polarization, a polarization filter could also be used to separate them. The optically amplified and filtered signal is then detected by a photo

diode and electrically amplified. All information but the power as a function of the time is lost. The opto-electrical conversion is represented by conversion gain C and noise equivalent power NEP . A low pass filter (transfer function $H(f)$) additionally reduces excess-band noise power. To obtain the binary data from the electrical signal, it is sampled and a gate decides between "0" and "1" by applying a certain decision threshold. The bit error probability (BEP) is then estimated with a bit error ratio tester by counting the false decisions during a certain gating period.

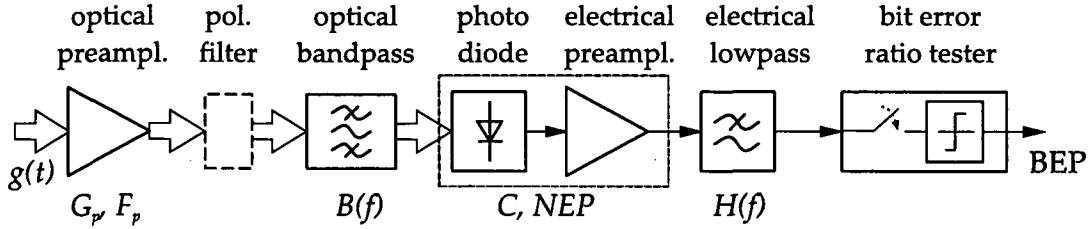


Figure 4.1: Setup of a preamplified direct detection receiver.

4.1.1 Optical input field

The optical input field, $g(t)$, comprising signal, noise originating in the transmitter, and background noise is denoted by

$$g(t) = (q(t) + n_{ASE,b})/\sqrt{A} + n_{back} = e_{in}(t) + n_{ASE,b}/\sqrt{A} + n_{back}, \quad (4.1)$$

where $q(t)$ is the transmit signal, $n_{ASE,b}$ is the amplified spontaneous emission from the transmitter's booster amplifier, n_{back} is the background noise, and A is the attenuation factor as defined in Sect. 2.4, Eq. (2.6) and Eq. (2.7) for downlink and uplink, respectively. The communication signal at the receiver input, $e_{in}(t)$, will be referred to when determining the receiver's sensitivity.

The input signal $e_{in}(t)$ is normalized to let its squared magnitude yield the optical input power ($p(t) = |e_{in}(t)|^2$). The optical power waveform representing a single "1"-bit, $p_1(t)$ is specified within the time interval $[0, (1 + \alpha)T_p]$ as

$$p_1(t) = \begin{cases} \frac{E_1}{2T_p} \left[1 - \sin\left(\frac{\pi}{\alpha T_p} \left(\left| t - (1 + \alpha)\frac{T_p}{2} \right| - \frac{T_p}{2} \right) \right) \right], & t \in \{[0, \alpha T_p] \cup [T_p, (1 + \alpha)T_p]\} \\ \frac{E_1}{T_p}, & t \in [\alpha T_p, T_p], \end{cases} \quad (4.2)$$

where E_1 denotes the optical energy for a "1"-bit, T_p is the effective pulse duration,

$$T_p = \frac{\int_{-\infty}^{\infty} p_1(t) dt}{\max\{p_1(t)\}} = \frac{E_1}{\max\{p_1(t)\}}, \quad (4.3)$$

and the "roll-off" factor α specifies the pulse shape: Varying α from 1 to 0, the pulse changes from $\cos^2(t)$ -like to rectangular. Setting $T_p = T_{bit}$ (T_{bit} being the bit duration) yields an isolated non return-to-zero (NRZ) "1"-bit, while $T_p = d \cdot T_{bit}$ produces return-to-zero (RZ) with duty cycle d . I would like to emphasize that E_1 is independent of the chosen duty cycle. Due to the normalization, the maximum of $p_1(t)$ changes according to T_p .

Examples of input signal eye diagrams for NRZ and RZ with different roll-off factors are given in Fig. 4.2. For most of the simulations performed, I used the following pulse parameters: NRZ: $\alpha = 0.4$; RZ: $d = 0.33$, $\alpha = 1$. The corresponding pulse shapes fit well to the signal generated by the transmitter used for measurements [77,78].

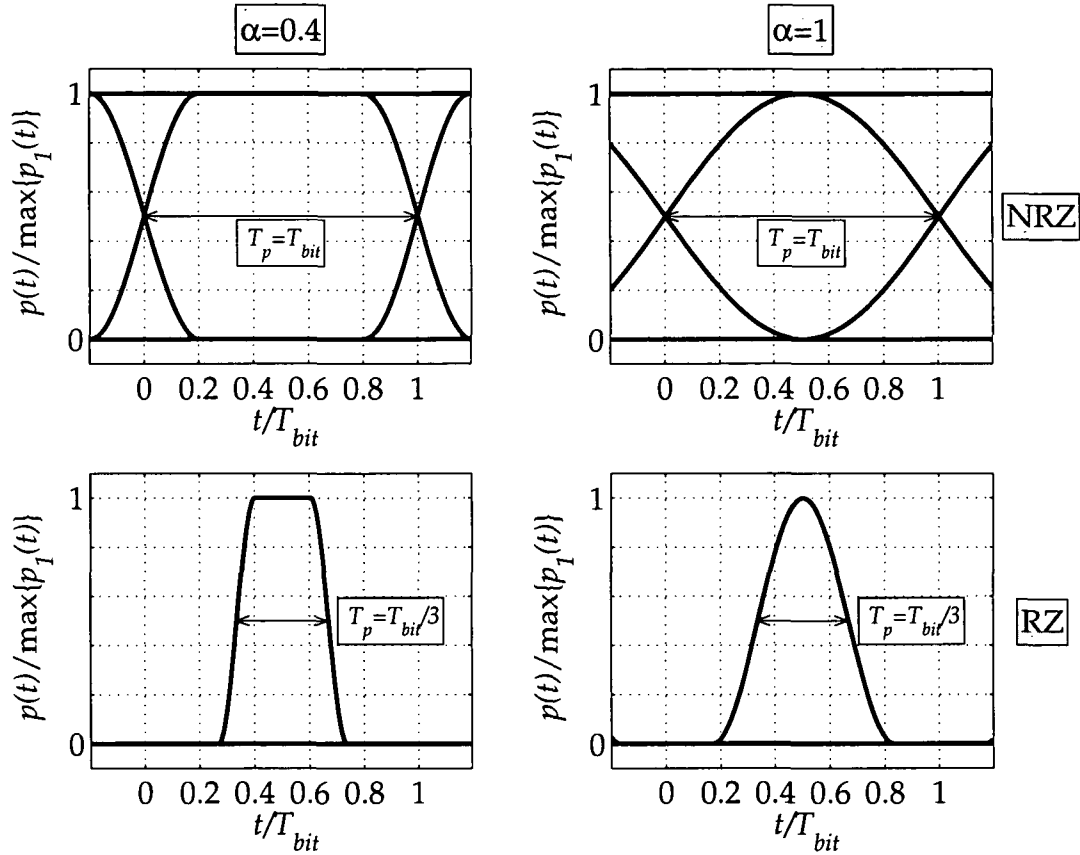


Figure 4.2: Input signal eye diagrams for NRZ and RZ ($d = 0.33$) with roll-off factors of 0.4 and 1.

The input signal $p(t)$ is obtained by arranging pulses $p_1(t)$ according to a pseudo random bit sequence (PRBS) of length $N = 2^n - 1$ in the following way (cf. Fig. 4.3 (a))

$$p(t) = \sum_{k=0}^{N-1} a_k p_1(t - kT_{bit}), \quad a_k \in \{0, 1\}, \quad (4.4)$$

with a_k the binary value of the k -th bit.

One of the key parameters deteriorating the system performance is the extinction ratio of the input signal. Low extinction ratio can not be compensated for by any measure at the receiver side.

Considering the different methods NRZ and RZ signalling may be generated in the transmitter (cf. Chapt. 5 and [32,77]), I apply two distinct definitions for the extinction ratio ζ , given in dB. For NRZ, it is the ratio of the maximum optical power for a "1"-bit to the minimum optical power for a "0"-bit, while for RZ, it is the ratio of the peak optical power for a "1"-bit to the peak optical power for a "0"-bit. Figure 4.3 (a) and (b) shows NRZ and RZ

pulse trains for infinite and finite extinction ratio. Depending on the transmitter setup, typical values for the extinction ratio are 10 – 20 dB.

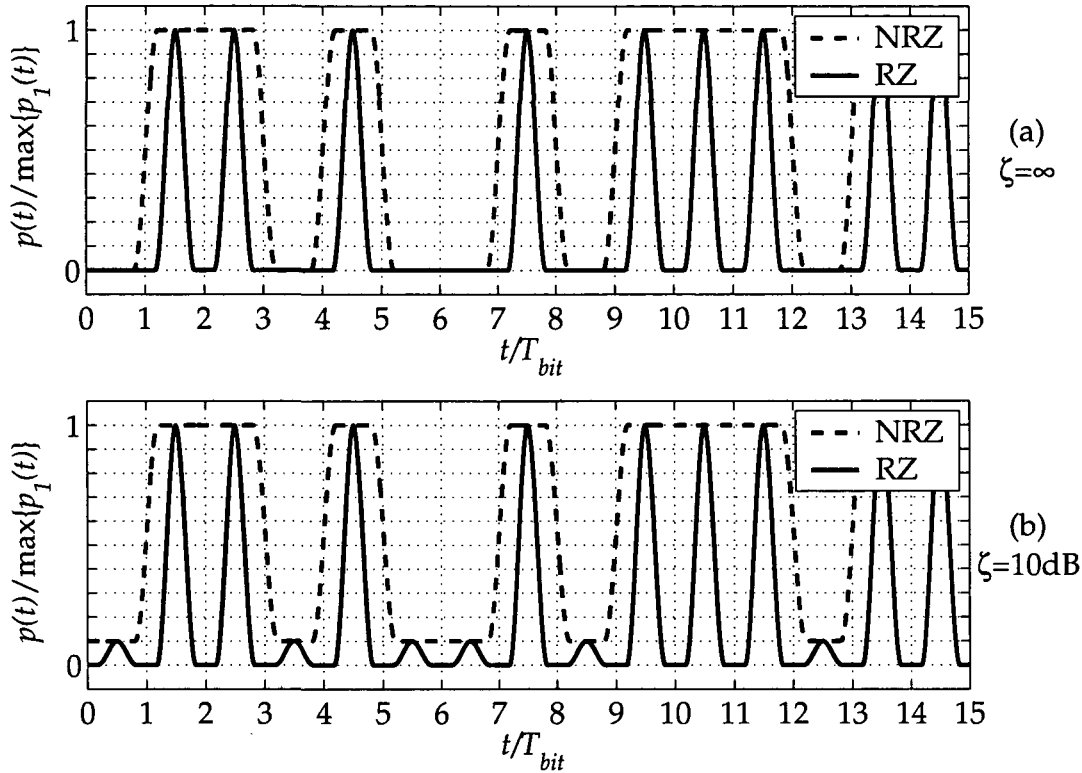


Figure 4.3: NRZ and RZ input signal for an extinction ratio of $\zeta = \infty$ (a), and $\zeta = 10\text{ dB}$ (b).

4.1.2 Optical preamplifier

The optical preamplifier amplifies the optical input field by $\sqrt{G_p}$ and introduces a circularly symmetric Gaussian noise process called amplified spontaneous emission (ASE). For $G_p \gg 1$, the power spectral density is [37]

$$N_{ASE,p} = \frac{hf}{2} G_p F_p \quad (4.5)$$

per spatial and polarization mode, where hf represents the energy of a photon. The theoretical minimum for the noise figure of optical amplifiers is 2 (3 dB). Fiber amplifiers especially designed to be used as preamplifiers have noise figures as low as $F_p = 3.3\text{ dB}$ [29]. Typical values for the power amplification are $G_p = 30 - 40\text{ dB}$.

For a well designed receiver, i.e. where the thermal noise is small compared to the ASE-induced beat noise terms (cf. Sect. 4.2), the actual value of G_p and any insertion loss of components following the preamplifier have negligible influence on the receiver's sensitivity [79].

4.1.3 Optical bandpass filter

After preamplification, the received signal is optically bandpass filtered to spectrally truncate the optical noise. The bandpass filter is assumed to be either a Fabry-Pérot filter (FPF) or a fiber Bragg grating (FBG) (in combination with a circulator to convert its bandstop characteristic into a bandpass characteristic) and is represented by its complex baseband field transfer function $B(f)$ and its complex baseband impulse response $b(t)$. I used the transfer functions

$$B_{FPF}(f) = \frac{1}{1 + j2f/B_o} \quad (4.6)$$

for the Fabry-Pérot filter (with B_o being the 3 dB-bandwidth of the filter), and

$$B_{FBG}(f) = \frac{1}{\tan[\kappa l]} \cdot \frac{-j\kappa \sin[\beta(f)l]}{j\beta(f) \cos[\beta(f)l] - (2\pi f/v_g) \sin[\beta(f)l]}, \quad (4.7)$$

for the fiber Bragg grating, [80, 81] where $\beta(f)$ stands short for

$$\beta(f) = \sqrt{(2\pi f/v_g)^2 - \kappa^2}, \quad (4.8)$$

and κ is the grating's coupling coefficient. In my simulations, κ was kept constant at a typical value [80] of 6 cm^{-1} , while the length of the grating, l , and the group velocity, v_g , were appropriately set to achieve the desired B_o at a constant sidelobe suppression ratio of $SLSR = 7 \text{ dB}$. Figure 4.4 shows magnitude and phase of the filter transfer functions as a function of the frequency normalized to the data rate R .

For a qualitative assessment of the effect of the optical bandpass on the ASE, the *power equivalent bandwidth*

$$B_{o,n} = \int_{-\infty}^{+\infty} |B(f)|^2 df \quad (4.9)$$

can be defined. Assuming the (data-) bandwidth to be equal to the filters B_o , the ratio $B_o/B_{o,n}$ is an indicator for the effectiveness of the filters noise suppression. For the FPF the ratio of signal width to power equivalent width is 63.7% while it is 85.7% for a FBG. This explains why Bragg gratings can lead to higher receiver sensitivities than Fabry-Pérot filters (see Sect. 4.4.3).

4.1.4 Photo diode module

The optically amplified and filtered signal is detected by a photo diode, electrically amplified and low-pass filtered. The detector, amplifier and filter together (referred to as *diode module*) are represented by two parameters: an overall transfer function, $H(f)$, and the *conversion gain*, C , comprising the detectors responsivity S , the gain of the electrical amplifier, and the insertion loss of the filter. It has the dimension $[A/W]$ or $[V/W]$.

For the overall transfer characteristics of the receive electronics, two cases were considered: a 5th order Bessel and a 1st order RC low pass characteristic. Bessel filters are often used because of their low overshoot and the widely linear group velocity (and therefore low pulse broadening). The transfer functions of the filters are normalized to unit area of the impulse

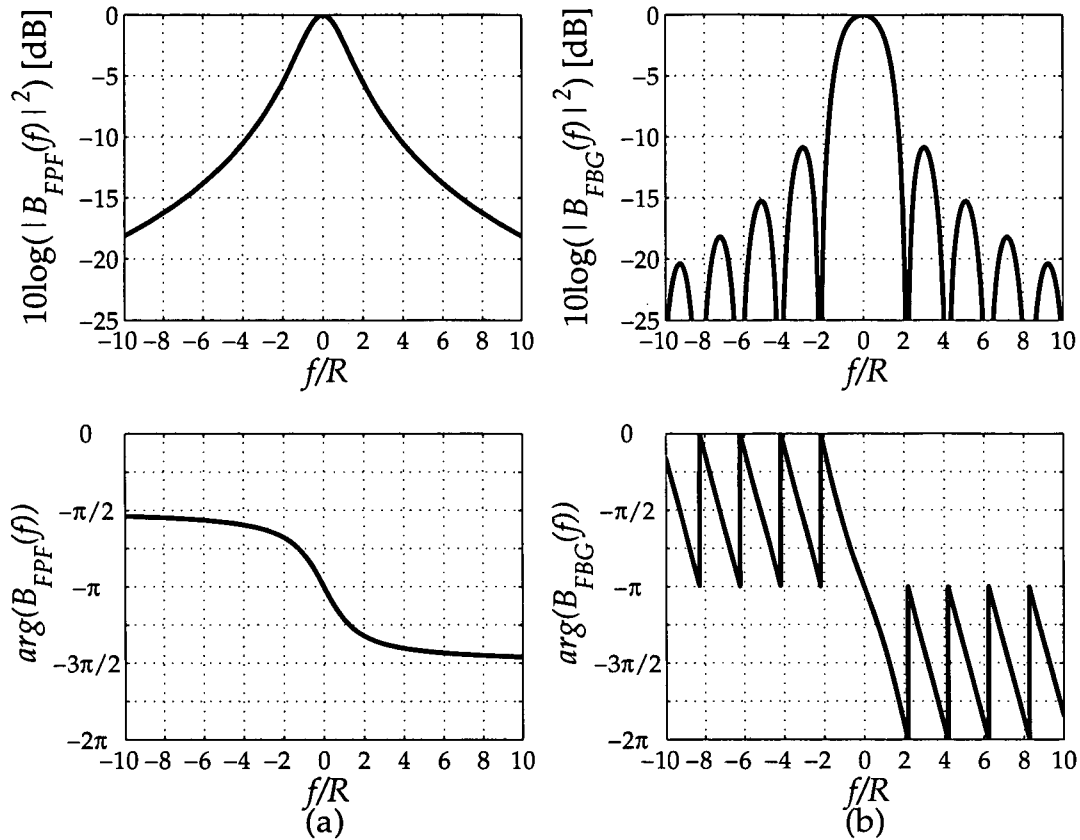


Figure 4.4: Squared magnitude and phase of the baseband field transfer function of a Fabry-Pérot filter (a) and of a fiber Bragg filter (b) as a function of the frequency normalized to the data rate R .

response¹ $h(t) \xrightarrow{\mathcal{F}} H(f)$,

$$\int_{-\infty}^{\infty} h(t) dt = H(0) = 1. \quad (4.10)$$

For the Bessel filter (BF), the transfer function is given by [83,84]

$$H_{BF}(s) = \frac{945}{js^5 + 15s^4 - 105js^3 - 420s^2 + 945js + 945} \quad (4.11)$$

with the normalized frequency

$$s = 2.52103 \frac{f}{B_{e,n}}. \quad (4.12)$$

For the RC low-pass filter (LF) $H(f)$ is given by

$$H_{LF}(f) = \frac{1}{1 + j\pi f / (2B_{e,n})}. \quad (4.13)$$

¹The symbol $\xrightarrow{\mathcal{F}}$ denotes the inverse Fourier transform, $x(t) \xrightarrow{\mathcal{F}} X(jf)$ corresponds to $x(t) = \int_{-\infty}^{\infty} X(jf) e^{j2\pi ft} df$ [82].

As in the case of the optical filter, the power equivalent width is defined as

$$B_{e,n} = \int_0^{\infty} |H(f)|^2 df. \quad (4.14)$$

Figure 4.5 shows magnitude and phase for both filter types.

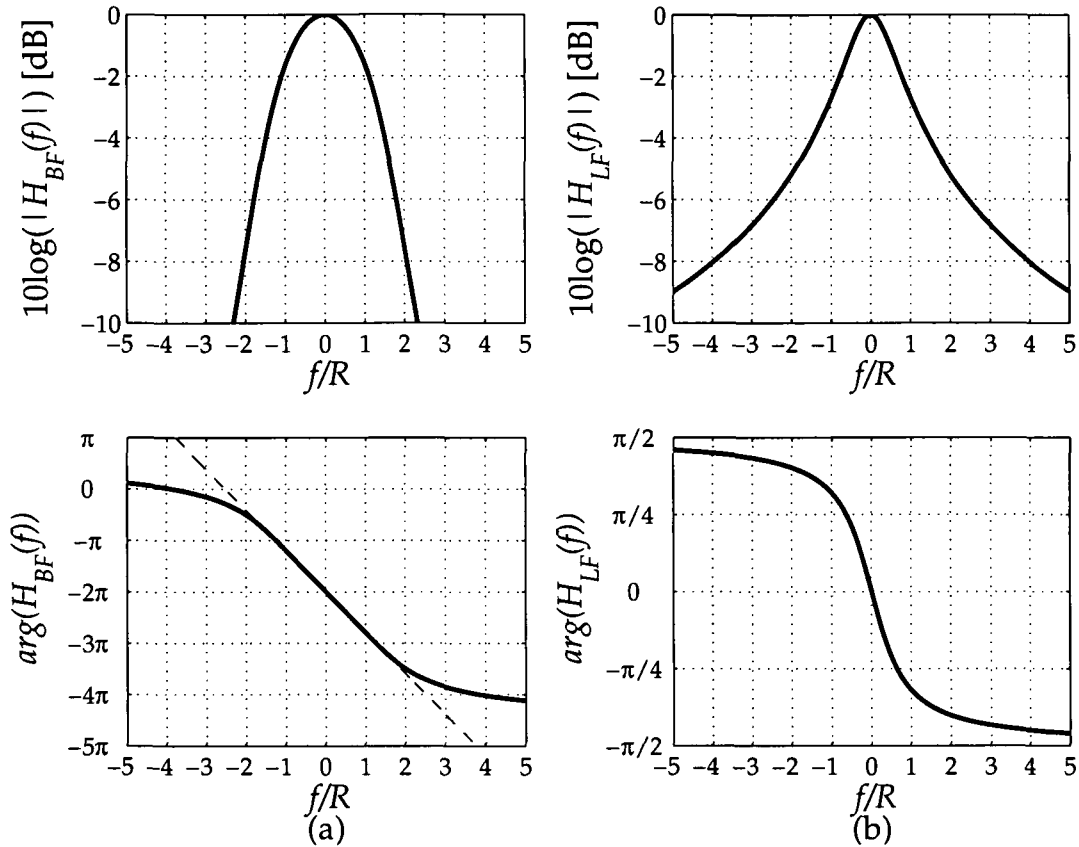


Figure 4.5: Magnitude and phase of Bessel filter of 5th order (a) and low pass filter of 1st order (b) transfer function as a function of the frequency normalized to the data rate R . Note the widely linear phase of the Bessel filter.

For the RC low pass the 3 dB bandwidth B_e is related to $B_{e,n}$ by $B_e = 2B_{e,n}/\pi$ while for the Bessel filter the 3 dB bandwidth is $B_e = 0.96B_{e,n}$.

4.1.5 Analog-to-digital conversion

The analog electrical signal is finally converted into a bit stream afflicted by a bit error probability $0 \leq \text{BEP} < 0.5$. The signal is sampled with a sampling rate R and a decision gate uses a threshold to distinguish between "0" and "1". With the signal's mean $s(t)$, the sampling instant T_s , and the decision threshold S_{th} , the k -th data bit reads

$$b_k = \begin{cases} 0 & s(kT_{bit} + T_s) < S_{th}, \\ 1 & s(kT_{bit} + T_s) \geq S_{th}. \end{cases} \quad (4.15)$$

One of the problems for the decision process is to provide a sampling rate being equal to the data rate at the transmitter. A temporal drift between transmitter and receiver can originate from one of the terminals (e.g. timing jitter of the pulse generator [77]), or from the link conditions (e.g. Doppler shift due to relative velocity of terminals). In real systems, a clock recovery has to be applied. Within the course of this work, I will assume the data clock to be perfectly available at the receiver.

4.2 Noise model

For the simulations presented here, I applied a quasi-analytical method – signal and noise are represented by their statistical properties, mean and variance. The bit error probability is then estimated from these values. The mean of the electrical signal after the diode module, specified in terms of voltage, is

$$s(t) = C \left\langle \left| \left(\sqrt{G_p} g(t) + n_{ASE,p} \right) * b(t) \right|^2 \right\rangle * h(t) \quad (4.16)$$

where $g(t)$ is the optical input field as defined by Eq. (4.1), G_p is the preamplifier's gain, $n_{ASE,p}$ is the amplified spontaneous emission from the preamplifier, C the conversion gain of the photo diode module (given in [V/W]), $b(t)$ and $h(t)$ are the impulse responses of the optical and electrical filter, respectively, and the operator $*$ the convolution, i.e.

$$(x * y)(t) = \int_{-\infty}^{\infty} x(\tau) y(t - \tau) d\tau. \quad (4.17)$$

The operator $\langle x \rangle$ denotes the expected value of a stochastic process x ,

$$\langle x \rangle = \int_{-\infty}^{\infty} \xi p_x(\xi) d\xi \quad (4.18)$$

with $p_x(\xi)$ being the probability density function of the process [85].

By applying Eq. (4.1), Eq. (4.16) expands to

$$s(t) = C \left\langle \left| \left(\sqrt{G_p} \left(e_{in}(t) + n_{ASE,b}/\sqrt{A} + n_{back} \right) + n_{ASE,p} \right) * b(t) \right|^2 \right\rangle * h(t). \quad (4.19)$$

By exploiting the facts that the signal $e_{in}(t)$ is deterministic,

$$\langle |(e_{in} * b)(t)|^2 \rangle = |(e * b)(t)|^2, \quad (4.20)$$

and the expected value of the optically filtered ASE and background noise is time invariant, and by taking into account the normalization of the diode module's impulse response, Eq. (4.10), the signal at the decision gate reads

$$s(t) = CG_p |(e_{in} * b)(t)|^2 * h(t) + C \frac{G_p}{A} P_{n,ASE,b} + CGP_{n,back} + CP_{n,ASE,p} \quad (4.21)$$

In this equation, the average of the optically filtered transmitter booster's ASE, background radiation, and the preamplifier's ASE are denoted by $P_{n,ASE,b} = \langle |(n_{ASE,b} * b)(t)|^2 \rangle = N_{ASE,b} r_b(0)$,

$P_{n,back} = \langle |(n_{back} * b)(t)|^2 \rangle = N_{back}r_b(0)$, and $P_{n,ASE,p} = \langle |(n_{ASE,p} * b)(t)|^2 \rangle = N_{ASE,p}r_b(0)$. Here N_x denotes the power spectral density of x^2 and $r_b(0)$ is the value of the optical filter's auto-correlation function

$$r_b(t) = \int_{-\infty}^{\infty} b(\tau)b^*(\tau - t)d\tau \quad (4.22)$$

at $t = 0$. The preamplifier's noise and the noise terms from background and booster amplifier can be combined to an overall noise power spectral density [86,87]

$$N_0 = G_p \left[\frac{N_{ASE,b}}{A} + N_{back} \right] + N_{ASE,p} = \frac{hf}{2} GF_{equ} \quad (4.23)$$

with the equivalent receiver noise figure,

$$F_{equ} = \frac{G_b}{A} F_b + N_{back} \frac{2}{hf} + F_p, \quad (4.24)$$

where F_b and G_b denote the noise figure and gain of the booster amplifier at the transmitter. Since in most systems the ASE from the preamplifier represents by far the dominating contribution to the overall noise power spectral density, N_0 will be referred to as "ASE" throughout the argumentations in this chapter.

The definition of the overall noise power spectral density given in Eq. (4.23), the electrical signal's mean is calculated to be

$$s(t) = CG_p |(e_{in} * b)(t)|^2 * h(t) + CN_0 r_b(0). \quad (4.25)$$

In the following, I will shortly compare two methods of calculating the variance of the electrical signal $\sigma_s(t) = \langle s^2(t) \rangle - \langle s(t) \rangle^2$: the advanced Gaussian model, where the exact variance is calculated, taking the actual filter transfer functions into account, and the standard noise model [79], assuming rectangular optical and electrical filter characteristics. While the latter is widely used throughout literature, the advanced model is computational more elaborate but leads to results better matching the experimental findings (cf. Sect. 4.5). For both methods, Gaussian noise statistics is assumed. A thorough comparison between the models has been performed in my diploma thesis [83]. It may be stated here that the standard noise model generally overestimates the variance and leads to sensitivity penalty predictions worse than confirmed through measurements (cf. Sect. 4.5 and [39,88]).

Three effects contribute to the electrical signal's variance: shot noise according to signal and ASE, beat noise terms between signal and ASE and ASE with itself, and thermal noise of the receiver electronics

$$\sigma_s^2(t) = \sigma_{shot,s}^2(t) + \sigma_{shot,ASE}^2(t) + \sigma_{s-ASE}^2(t) + \sigma_{ASE-ASE}^2(t) + \sigma_{elec}^2(t). \quad (4.26)$$

Independent of the model applied, electronic noise is defined by the diode module's noise equivalent power (NEP), usually given in $[W/\sqrt{\text{Hz}}]$ [47], the corresponding variance is given by [32]

$$\sigma_{elec}^2 = C^2 \cdot NEP^2 \cdot B_{e,n}. \quad (4.27)$$

²The power spectral density of the background radiation N_{back} is defined by Eq. (2.19), the ASE power spectral density for both transmitter and receiver amplifier is given by Eq. (4.5).

4.2.1 Advanced Gaussian model

For the advanced Gaussian model, the derivation of the individual contributions to the variance of the electrical signal at the decision gate are presented elsewhere [77, 87, 89]. Here I will cite only the results. The shot noise according to signal and ASE result to be

$$\sigma_{shot,s}^2 = SR_T^2 G_p q (|e_{in} * b(t)|^2 * h^2(t)), \quad (4.28)$$

and

$$\sigma_{shot,ASE}^2 = 2SR_T^2 M_{pol} q P_{n,ASE} B_{e,n}, \quad (4.29)$$

respectively. Here, q denotes the elementary charge of an electron, $1.602 \cdot 10^{-19}$ As, $S = \eta q / (hf)$ [A/W] is the photo diode's responsivity, R_T is the resistance that converts the current-output of the photo diode into a voltage, and $P_{n,ASE} = N_0 r_b(0)$ is the overall noise average. The number of ASE-modes reaching the detector is denoted M_{pol} . In a single-mode system there is only one spatial mode, resulting in $M_{pol} = 2$, taking two polarization modes into account. If a polarization filter is implemented (see Fig. 4.1), M_{pol} is one. The variance originating from beating between signal and ASE is

$$\sigma_{s-ASE}^2(t) = 2C^2 N_0 \text{Re} \left\{ \int_{-\infty}^{\infty} \int_{-\infty}^{\infty} e_f(\tau) e_f^*(\bar{\tau}) r_b(\tau - \bar{\tau}) h(t - \tau) h(t - \bar{\tau}) d\tau d\bar{\tau} \right\}, \quad (4.30)$$

where $e_f(t) = \sqrt{G}(e_{in} * b)(t)$ is the optically amplified and filtered field, while beating of ASE with itself results in

$$\sigma_{ASE-ASE}^2 = M_{pol} C^2 N_0^2 \int_{-\infty}^{\infty} |r_b(\tau)|^2 r_h(\tau) d\tau. \quad (4.31)$$

Here, $r_h(t)$ is the electrical filter's autocorrelation function corresponding to the definition of Eq. (4.22).

4.2.2 Standard model

The noise contributions corresponding to Eq. (4.26) are as follows [79, 90]: The shot noise according to signal and ASE read

$$\sigma_{shot,s}^2 = 2qSR_T^2 p(t) B_{e,n}, \quad (4.32)$$

and

$$\sigma_{shot,ASE}^2 = 2M_{pol} q N_0 B_o SR_T^2 B_{e,n}, \quad (4.33)$$

respectively. The variance originating from beating between signal and ASE is

$$\sigma_{s-ASE}^2(t) = 4CN_0 s(t) B_{e,n}, \quad (4.34)$$

while beating of ASE with itself results in

$$\sigma_{ASE-ASE}^2 = M_{pol} C^2 N_0^2 B_{e,n} (2B_o - B_{e,n}). \quad (4.35)$$

4.3 Calculating the receiver sensitivity

With the expressions for signal and noise denoted in the previous section available, the BEP at a sampling time T_s and for a decision threshold S_{th} calculates [31]

$$\text{BEP}(T_s, S_{th}) = \frac{1}{2^n - 1} \left\{ \sum_{k_0} \frac{1}{2} \operatorname{erfc} \left[\frac{S_{th} - s(T_s + k_0 T_{bit})}{\sqrt{2} \sigma_s (T_s + k_0 T_{bit})} \right] + \sum_{k_1} \frac{1}{2} \operatorname{erfc} \left[\frac{s(T_s + k_1 T_{bit}) - S_{th}}{\sqrt{2} \sigma_s (T_s + k_1 T_{bit})} \right] \right\}, \quad (4.36)$$

where the indices k_0 and k_1 are used to distinguish between the $2^{n-1} - 1$ "0"-bits and the 2^{n-1} "1"-bits of the PN sequence and

$$\operatorname{erfc}(x) = \frac{2}{\sqrt{\pi}} \int_x^\infty \exp(-t^2) dt \quad (4.37)$$

is the complementary error function. To take ISI into consideration with sufficient accuracy, it is necessary that the length of the bit sequence is at least $2^7 - 1$ [91].

Finally, the receiver sensitivity n_s is calculated, defined as the required average number of photons per bit at the optical amplifier input to achieve $\text{BEP} = 10^{-9}$; unless stated otherwise, the results presented in this work are given in terms of a sensitivity penalty γ_q relative to the quantum limit n_q ,

$$\gamma_q = 10 \log(n_s/n_q) \text{ [dB]}, \quad (4.38)$$

where n_q evaluates to 43.6 photons/bit using the Gaussian approximation with optimized decision threshold for $M_{pol} = 2$ [31]. The corresponding theoretically optimum optically preamplified receiver structure consists of a matched optical filter and no post-detection electrical filtering.

Note that different results for γ_q as a function of the receiver bandwidths may be obtained if the receiver sensitivity is defined via other BEP values, since these require other input power levels (see Fig. 4.6). For the breadboard described in the following chapter, a BEP of 10^{-6} was aimed at, while for some telecom applications the standard is $\text{BEP} = 10^{-12}$ or even better.

4.4 Simulation results

4.4.1 Decision threshold and sampling instant

The BEP after the decision process is a function of the sampling instant T_s and the decision threshold S_{th} (cf. Eq. (4.36)). Figure 4.7 shows an example of such a dependency for NRZ and RZ coded input signals [83]. There is a distinct minimum for the BEP, showing a mutual dependence on both parameters. The BEP as a function of the decision threshold exhibits the expected "V" shape³, the minimum according to the sampling instant is comparatively flat. For RZ signals, the optimum decision threshold is very low with an extremely steep gradient towards lower threshold values. This is an indication that little ISI is present and the noise of the "1"-bits dominates the "0"-bit noise for this format. I will investigate this in the following chapter.

³It has been shown that the actual value of the optimum decision threshold differs significantly from the predictions resulting from the applied calculation method [92–96], the interpretations given here are just of qualitative nature.

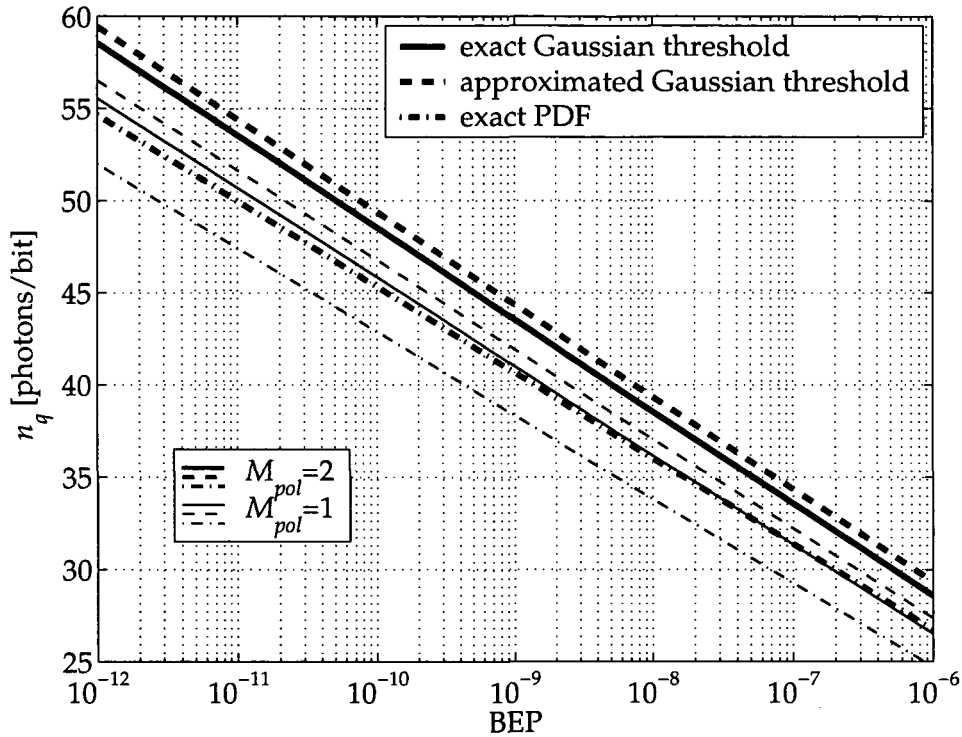


Figure 4.6: Quantum limit n_q in photons per bit as a function of the desired bit error probability for one and two polarizational modes ($M_{pol} = 1$, and $M_{pol} = 2$, respectively). The results obtained for the exact threshold and the approximated threshold for Gaussian noise are represented by the solid and dashed lines, respectively [31, 92], while the dashed-dotted lines show the results obtained when considering the photocurrent's exact probability density function (PDF) [93].

The contour plots below the surface in Fig. 4.7 give lines for constant BEP values differing by two orders of magnitude. These lines may also be interpreted as “error rate pattern” [97], a generalized form of the eye diagram. It gives the tolerance concerning T_s or S_{th} when aiming at a certain BEP.

The sensitivity penalty to be expected when applying suboptimum sampling instant or decision threshold can be read off from Fig. 4.8 for NRZ and RZ signalling. The reason for the optimum sampling instant being so “late” compared to the input signal (the maximum of the input signal is at $T/T_{bit} = 0.5$, cf. Fig. 4.2, where the optimum sampling instant is at about $T/T_{bit} = 1.25$) is the time delay introduced by the optical and (mainly) the electrical filter. The sampling instant therefore strongly depends on the filter bandwidth.

For both the simulation and the measurement presented within this work, sampling instant and decision threshold were optimized to reach minimum BEP for every single receiver configuration and according to the actual input power. The optimum decision threshold is a function of the input power because of the balance between beat noise terms due to signal and ASE and ASE with itself. Higher input power levels will lead to higher signal-dependent noise, i.e. σ_{s-ASE}^2 , and therefore to higher optimum values for the threshold.

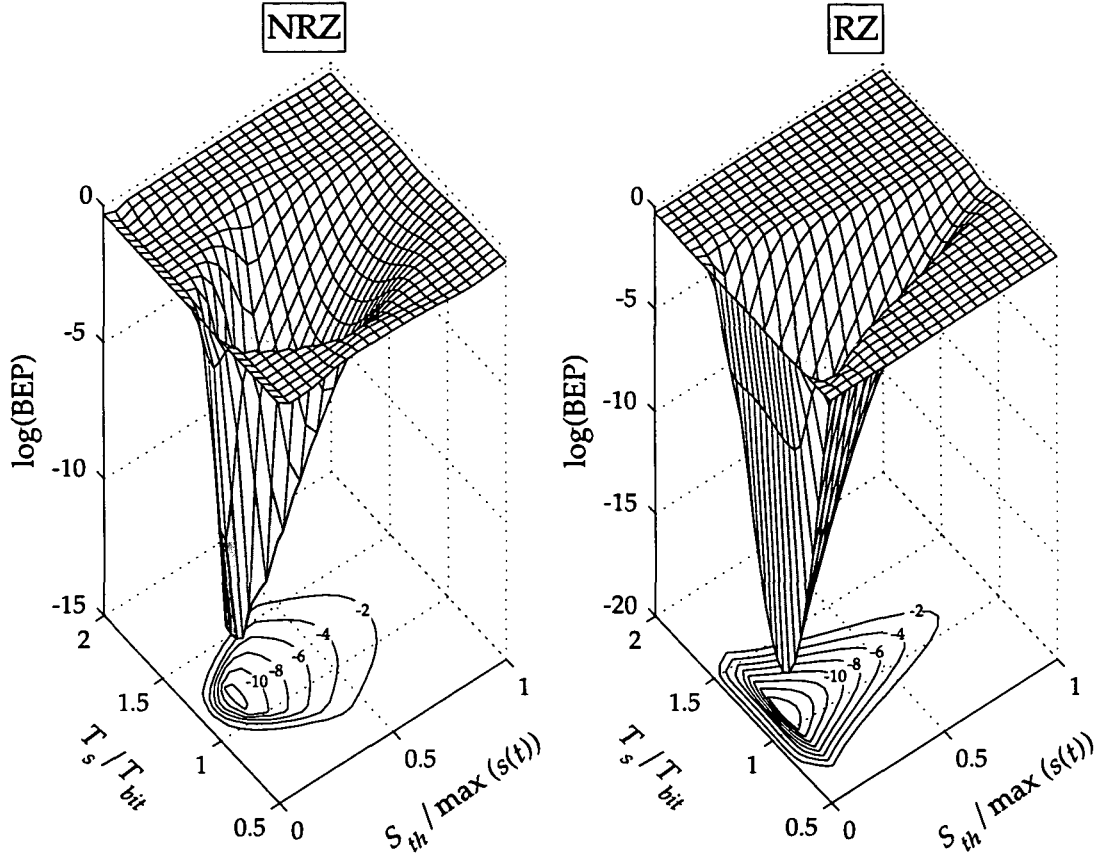


Figure 4.7: BEP as a function of sampling instant and decision threshold for NRZ and RZ input signals. The bandwidth of the optical and electrical filter is $B_o = 2.5R$ and $B_{e,n} = 0.8R$ with a Bragg filter and Bessel filter, respectively.

4.4.2 Filter bandwidth optimization

In this section, I will present simulation results concerning the different effects leading to tradeoffs between narrowband and broadband optical and electrical filters and the mutual influence of these two parameters. The considerations result in an optimum choice of optical and electrical filter bandwidth [88,98,99].

The input signal is a PRBS with the length of $2^7 - 1$ at a data rate of $R = 10$ Gb/s. For the time being, the input signal is assumed to be noise-free (no background radiation and no transmitter noise), and the pulses are ideal NRZ or RZ pulses with infinite extinction ratio as shown in Fig. 4.3 (a). The preamplifier's gain is 38 dB, its noise figure is 3.3 dB. The insertion loss of the optical filter (FBG) is 5 dB, resulting in an overall optical gain of 33 dB. I used a Bessel characteristic for the electrical filter. The broadband *pin* photodiode is followed by a broadband electrical preamplifier (both assumed to have infinite bandwidth) in order to yield an overall conversion gain of 1350 V/W as well as a noise equivalent power of $NEP = 2.96 \cdot 10^{-11}$ W/ $\sqrt{\text{Hz}}$. Table 4.1 lists the simulation parameters used to obtain the presented results.

The main objective of the optical filter is to reduce the amount of out-of-band ASE reach-

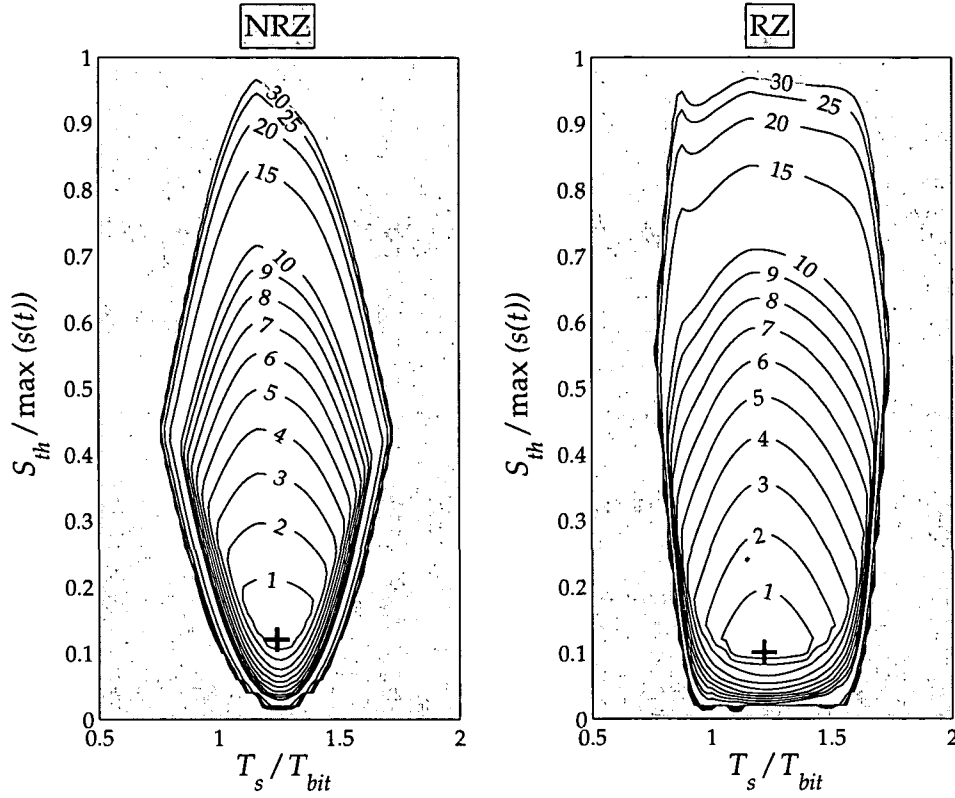


Figure 4.8: Sensitivity penalty in dB relative to the value for optimum T_s and S_{th} as a function of sampling instant and decision threshold for NRZ and RZ signals. Penalties larger than 30 dB are not shown. The parameters are equal to those used for Fig. 4.7.

	Symbol and Value	Description
input signal	$R = 10 \text{ Gb/s}$ $N = 2^7 - 1$ $\lambda = 1550 \text{ nm}$ $\zeta = \infty$ $M_{pol} = 2$ $N_{back} = 0 \text{ W/Hz}$	data rate length of the PRBS wavelength extinction ratio number of polarization modes spectral density of the background radiation
optical amplifier	$G_p = 38 \text{ dB}$ $F_p = 3.3 \text{ dB}$	gain of the preamplifier EDFA noise figure of the preamplifier EDFA
optical filter	$IL = 5 \text{ dB}$ $SLSR = 11 \text{ dB}$ $ \kappa = 3 \text{ cm}^{-1}$	insertion loss of optical filter side lobe suppression ratio (for fiber Bragg grating) coupling coefficient (for fiber Bragg grating)
diode module	$C = 1350 \text{ V/W}$ $NEP = 2.96 \cdot 10^{-11} \text{ W}/\sqrt{\text{Hz}}$	conversion gain of the diode module noise equivalent power of diode module

Table 4.1: Parameters used for simulations.

ing the detector, which in turn lowers the ASE-ASE beat noise⁴. Until recently optical band-

⁴To a good approximation [79], the ASE-ASE beat noise is linearly proportional to the optical bandwidth, while

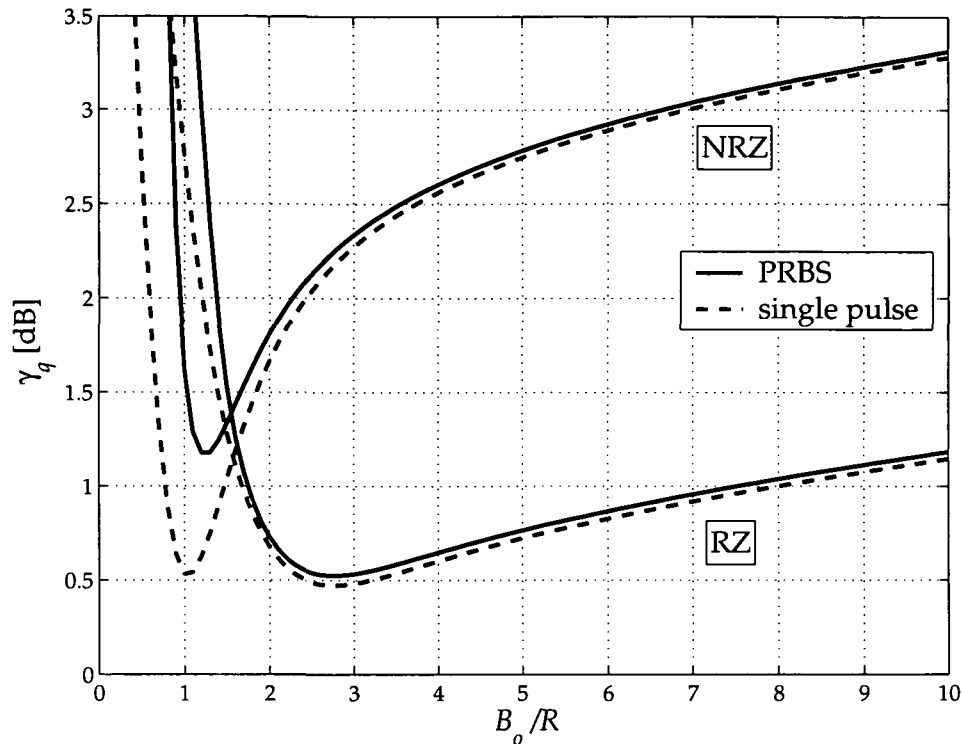


Figure 4.9: Sensitivity penalty vs. optical filter bandwidth for NRZ and RZ ($d = 0.33$) coded signals. Solid lines represent results for a PRBS, while dashed lines stand for the single-pulse case. The electrical bandwidth is kept constant at $B_e = 0.77R$.

pass filters were chosen as narrow as possible. However, the increase of data rates to ranges beyond 10 Gb/s combined with the availability of optical filters with bandwidths on the order of 10 GHz has led to technically realizable situations in which narrowband optical filters start to deteriorate receiver performance. For RZ, optical filters with bandwidths too small mainly reduce the signal energy, while for NRZ they significantly increase intersymbol interference (ISI).

Figure 4.9 illustrates the trade-offs to be made when optimizing the *optical* filter bandwidth: The receiver sensitivity penalty γ_q is given as a function of the optical bandwidth B_o for both NRZ-coding and RZ-coding with 33% duty cycle ($d = 0.33$). The electrical filter bandwidth is kept constant at $B_e = 0.77R$. The dashed curves apply to the ISI-free single-pulse case, which is obtained by sampling only a single, isolated "1"-bit and a single, isolated "0"-bit. Decreasing the optical bandwidth from $10R$ initially improves receiver sensitivity, both for RZ and NRZ, due to reduced ASE-ASE beat noise. If chosen below $2.7R$ for RZ (below $1R$ for NRZ), the penalty increases significantly. For the single-pulse case, this increase can be attributed solely to energy truncation brought by the optical filter [86, 98]. To quantitatively assess the influence of ISI on system performance, I now compare the single-pulse case to the results for a PRBS (solid lines in Fig. 4.9). For high optical bandwidths, the ISI-free curves very close to the curves resulting for the PRBS, indicating the absence of ISI. Mov-

the signal-ASE beat noise is independent of the optical bandwidth (cf. former section).

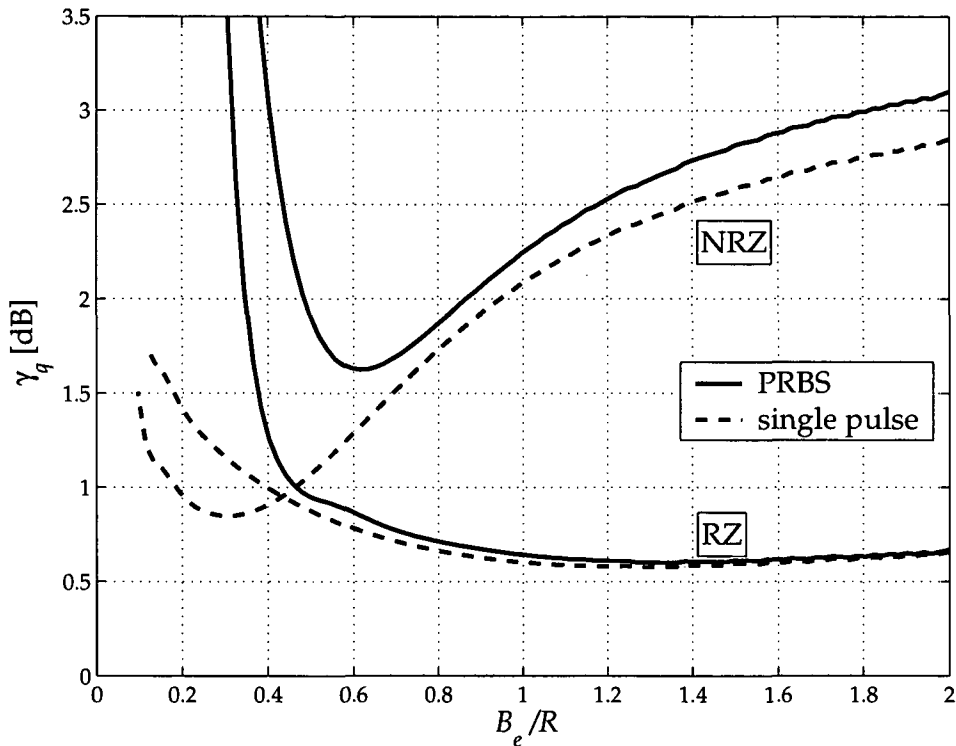


Figure 4.10: Sensitivity penalty vs. electrical filter bandwidth for NRZ and RZ ($d = 0.33$) coded signals. Solid lines represent results for a PRBS, while the dashed lines stand for the single-pulse case. The optical bandwidth is kept constant at $B_o = 2R$.

ing towards smaller bandwidths, the NRZ curves start to separate at a bandwidth of about $B_o = 3R$. This is where the deteriorating effect of ISI sets in. For NRZ, the optimum optical bandwidth in the presence of ISI ($B_o = 1.3R$) is higher than for the ISI-free case ($B_o = 1R$), which shows that a trade-off between ISI for too high B_o and ASE-ASE beat noise for too low B_o has to be made for NRZ. For RZ-coding, on the other hand, there is almost no difference between the results for the PRBS and the single-pulse case for $B_o \geq 1.5R$, leading to the conclusion that ISI plays a minor role in optimizing the optical bandwidth for RZ. In this case, it is rather the energy reduction accompanying too narrow optical filtering that has to be compromised with noise; RZ pulses with a duty cycle of 33% roughly correspond to a spectral width of $3R$, which is close to the optimum optical bandwidth of $B_o = 2.7R$ (for both PRBS and single pulse case).

The trade-offs to be made when optimizing the *electrical* filter bandwidth, can be understood when observing the dependence of the sensitivity penalty γ_q on B_e for constant optical bandwidth ($B_o = 2R$), as shown in Fig. 4.10. Again, the dashed curves apply for the single-pulse case, while the solid lines take into account ISI. The difference between the ISI-free case and the PRBS case for NRZ at high B_e reflects the ISI brought by the optical filter (for $B_e = 0.77R$, the difference can also be read off from Fig. 4.9, at $B_o = 2R$). In the case of NRZ, decreasing B_e from $2R$ improves the sensitivity due to reduced detection noise, until at $B_e = 0.65R$ the sensitivity starts to degrade because of ISI, marked by the beginning separation of the dashed and solid NRZ-curves at $B_e = 0.8R$. At $B_e = 0.3R$, the ISI-free curve also

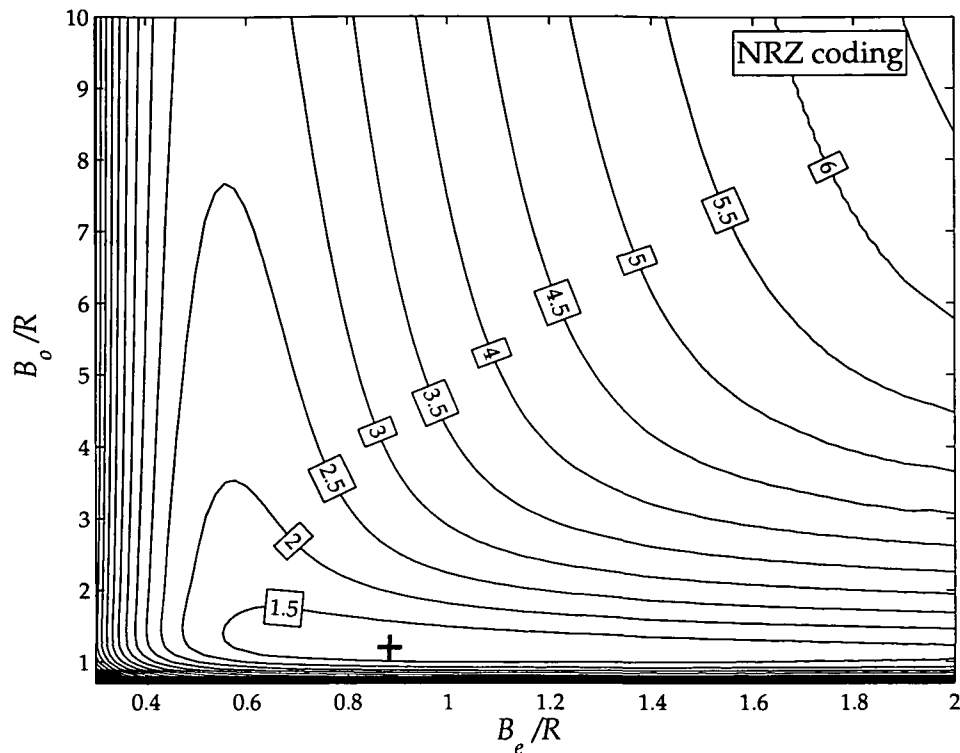


Figure 4.11: Receiver sensitivity penalty γ_q relative to the quantum limit as a function of optical and electrical bandwidth, B_o and B_e for NRZ-coding. The contour lines are separated by 0.5 dB.

starts to degrade, which can be attributed to the signal-independent noise terms (ASE-ASE beat noise and thermal noise) overtaking the signal-dependent noise term (signal-ASE beat noise) [91]. For RZ, ISI is seen to set in only at $B_e = 0.5R$, which is significantly lower than the optimum value ($B_e = 1.5R$). Thus, as in the case of the optical bandwidth, the receiver sensitivity for NRZ coding is limited by ISI, while for RZ, the optimum receiver performance is found by trading detection noise against pulse energy reduction due to too narrowband electrical filtering.

I can thus identify ISI being the main reason, why RZ outperforms NRZ by 1 – 2 dB at optimized bandwidths; for the ISI-free case, the optimum NRZ performance is much closer to that of RZ. This finding is specific to receivers limited by signal-dependent noise, and contrasts the behavior of receivers limited by signal-independent noise, since the latter show significant improvement due to employment of RZ coding (“RZ gain”) even for the ISI-free case [90].

To identify the optimum bandwidth constellation, the mutual dependence of the receiver sensitivity on *optical and electrical* filter bandwidth is investigated. Figures 4.11 and 4.12 display the sensitivity penalty γ_q vs. both B_o and B_e for NRZ and RZ, respectively. The contour lines (lines of constant γ_q) are separated by 0.5 dB in both plots. The plots not only reveal the optimum bandwidths, they also provide an overview of system tolerances regarding bandwidth variations, which are considerably different for NRZ and RZ: In general, RZ is much more tolerant to suboptimum receiver bandwidths than NRZ. Further, both for RZ and NRZ,

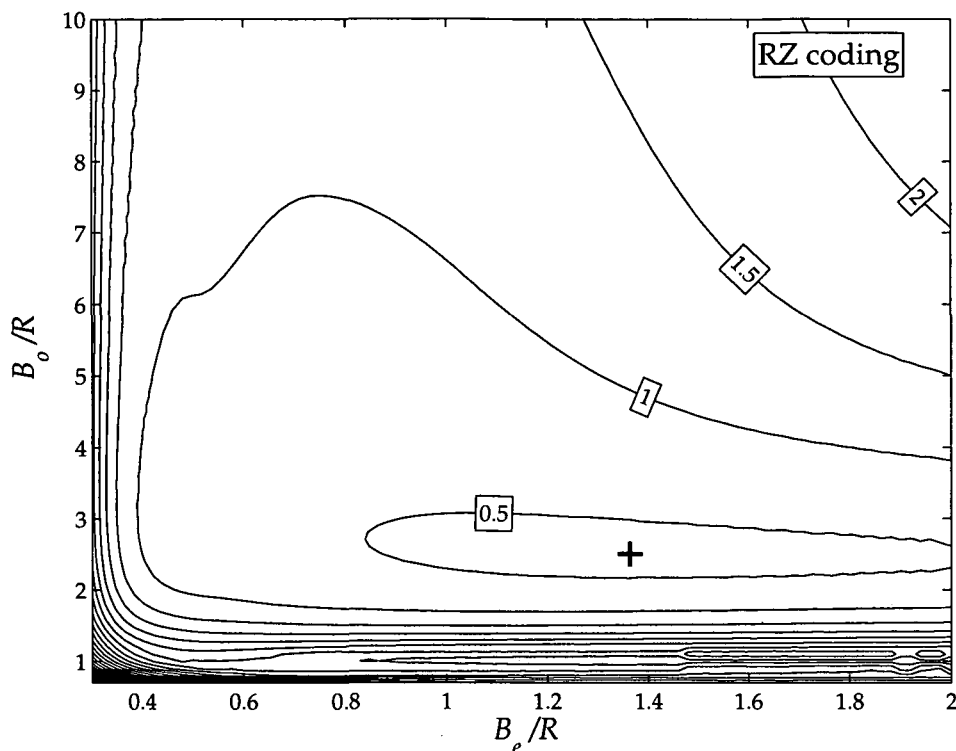


Figure 4.12: The same as Fig. 4.11 but for RZ coding.

choosing bandwidths larger than the optimum has less consequences on system performance than excessive narrowband filtering [39, 89, 94, 98, 100, 101]. For NRZ coding, Fig. 4.11 shows that the choice of the electrical bandwidth B_e becomes more critical if broadband, suboptimum optical filters are used. In this case, the optical filter is of little influence, regarding both signal distortion (ISI) and ASE noise reduction. Under these circumstances, B_e is the only parameter to affect ISI and, consequently, has to be chosen carefully. Using an electrical filter of about $B_e = 0.6R$, the influence of B_o on receiver performance is rather weak.

Over a wide range of electrical bandwidths (from $0.5R$ to $2R$) the optimum optical bandwidth is quite independent of the actual B_e employed. The optimum electrical bandwidth is $0.6R$ for optical filter bandwidths larger than $3R$. However, to maximize system performance, the electrical bandwidth has to be significantly increased to $B_e = 0.9$ as B_o approaches its optimum. This owes to the fact that detection noise due to ASE is already reduced to a large extent by optical filtering. Since the beating of signal-ASE and ASE-ASE are by far the dominating noise sources, any further reduction of noise power by means of electrical filtering is of little effect on performance. Reducing B_e will rather introduce unwanted degradations due to ISI. Thus, the electrical bandwidth primarily has to be chosen to avoid ISI (and *not* for noise reduction). As a consequence, the influence of B_e is less pronounced with optimum optical filtering, provided that B_e lies within a range of about $0.8R$ up to $2R$. To put it into other words, filtering in the optical domain is more effective than filtering in the electrical domain, as this reduces ASE bandwidth *and* ASE power, whereas electrical filtering only acts on the receiver noise bandwidth [89].

4.4.3 Influence of filter characteristics

After having shed some light on the effects leading to optimum filter bandwidths, I now will investigate the influence of the filter characteristics of both optical and electrical filter on the receiver performance. In Figs. 4.13 and 4.14 the sensitivity penalty is displayed as a function of optical and electrical filter bandwidth for different combinations of filter characteristics (FBG and FPF optical filter and BF and LF electrical filter) for NRZ and RZ coding, respectively.

When comparing the cases for different **optical filters**, the receivers employing FBG filters appear to be more sensitive towards suboptimum bandwidth choice than those with FPF filters, independent of the electrical filter type and the coding scheme. This can be attributed to the fact that the FBG's transfer function has steeper edges and is therefore spectrally more efficient (cf. Sect. 4.1.3): Too narrowband or too broadband filtering with the FBG results in higher signal energy reduction or increased ASE collection, respectively. Additionally, there is a slight sensitivity improvement compared to FPF optical filtering because the transfer function of the FBG better matches the signal's spectrum. These statements are confirmed by the numerical results of optimum sensitivity penalty, corresponding optical and electrical filter bandwidths and the bandwidth tolerances presented in Tabs. 4.2 and 4.3.

The performance for the two **electrical filter** characteristics is nearly equal. The main difference is that for the LF, the sensitivity penalty for small bandwidths is more moderate than for the BF. This is a consequence of the LF's power equivalent width being higher for equal 3 dB bandwidth (cf. Sect. 4.1.4). When employing a diode module with suboptimum bandwidth it is better to choose a LF characteristic than BF characteristic. The BF on the other hand leads to slightly higher sensitivity values.

I would like to add some remarks on the bandwidth tolerances as given in the Tabs. 4.2 and 4.3. In some cases the tolerance for the optical or electrical bandwidth can take on extremely high values (e.g. $\Delta B_o = 13.7/R$ for the FPE/BF/RZ scenario or $\Delta B_e = 7.2/R$ for FBG/BF/NRZ). In these cases, the receiver sensitivity is nearly independent of the choice of this filters bandwidth provided that it is higher than a certain value and that the bandwidth of the other filter is chosen accordingly.

Observing the shape of the sensitivity isolines in Figs. 4.13 and 4.14 a general design guideline can be established, as already stated in the previous chapter: Independent of the pulse shape and filter combination, there can always be chosen an optical filter bandwidth, for which – even if suboptimum – the receiver performance is nearly independent of the electrical filter bandwidth (as long as it is higher than a minimum value). Keeping in mind that one has practically free hand for the optical bandwidth (at least in a single-channel system) it is advisory to adjust this parameter according to the electrical bandwidth of the receiver.

However, too narrow optical filters may impose problems when the exact wavelength of the transmit laser is not known or exerts fluctuations. At 10 Gb/s, $\Delta f = 1.2R$ corresponds to $\Delta\lambda = 100$ pm. The accuracy of the matching between laser frequency and filter transfer function has to be higher by an order of magnitude to avoid deteriorating effects (cf. Sect. 5.2). Frequency fluctuations e.g. due to Doppler shifts as a consequence of the relative velocity of transmitter and receiver terminals can amount to several gigahertz [102].

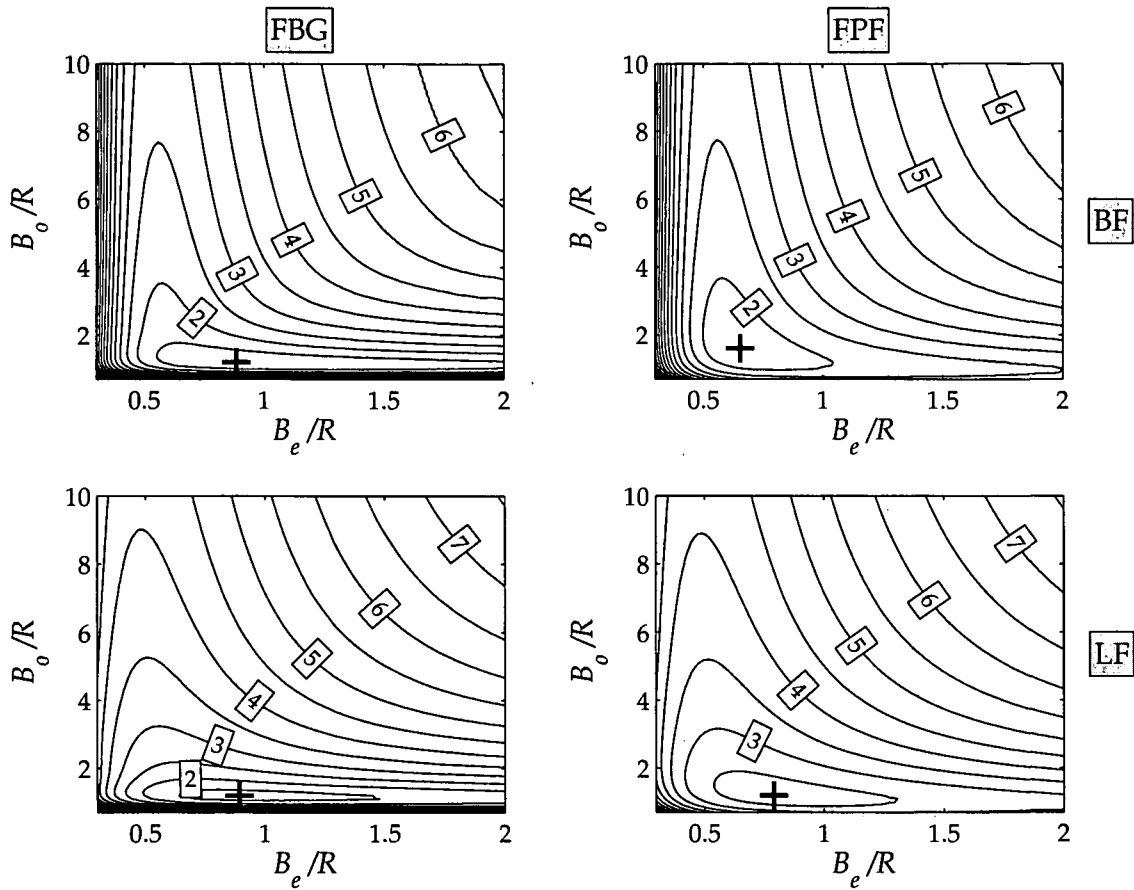


Figure 4.13: Sensitivity penalty vs. optical and electrical bandwidth for different combinations of filter characteristics for NRZ coding (FBG ... fiber Bragg grating, FPF ... Fabry-Pérot filter, BF ... 5th order Bessel filter, LF ... low-pass filter).

		FBG	FPF	
NRZ	$\gamma_{q,min}$	= 1.2 dB	$\gamma_{q,min}$ = 1.6 dB	BF
	$B_{o,opt}$	= 1.2/R	$B_{o,opt}$ = 1.6/R	
	ΔB_o	= 1.1/R	ΔB_o = 6.6/R	
	$B_{e,opt}$	= 0.9/R	$B_{e,opt}$ = 0.7/R	
	ΔB_e	= 7.2/R	ΔB_e = 0.9/R	LF
	$\gamma_{q,min}$	= 1.3 dB	$\gamma_{q,min}$ = 2.3 dB	
	$B_{o,opt}$	= 1.2/R	$B_{o,opt}$ = 1.2/R	
	ΔB_o	= 0.8/R	ΔB_o = 2.3/R	
$B_{e,opt}$	= 0.9/R	$B_{e,opt}$ = 0.8/R		
ΔB_e	= 3.1/R	ΔB_e = 2.2/R		

Table 4.2: Minimum sensitivity penalty with corresponding optimum optical and electrical filter bandwidths and the bandwidth tolerances, where ΔB_o and ΔB_e stand for the range the optical and electrical bandwidth may be varied accepting a sensitivity penalty of less than 1 dB.

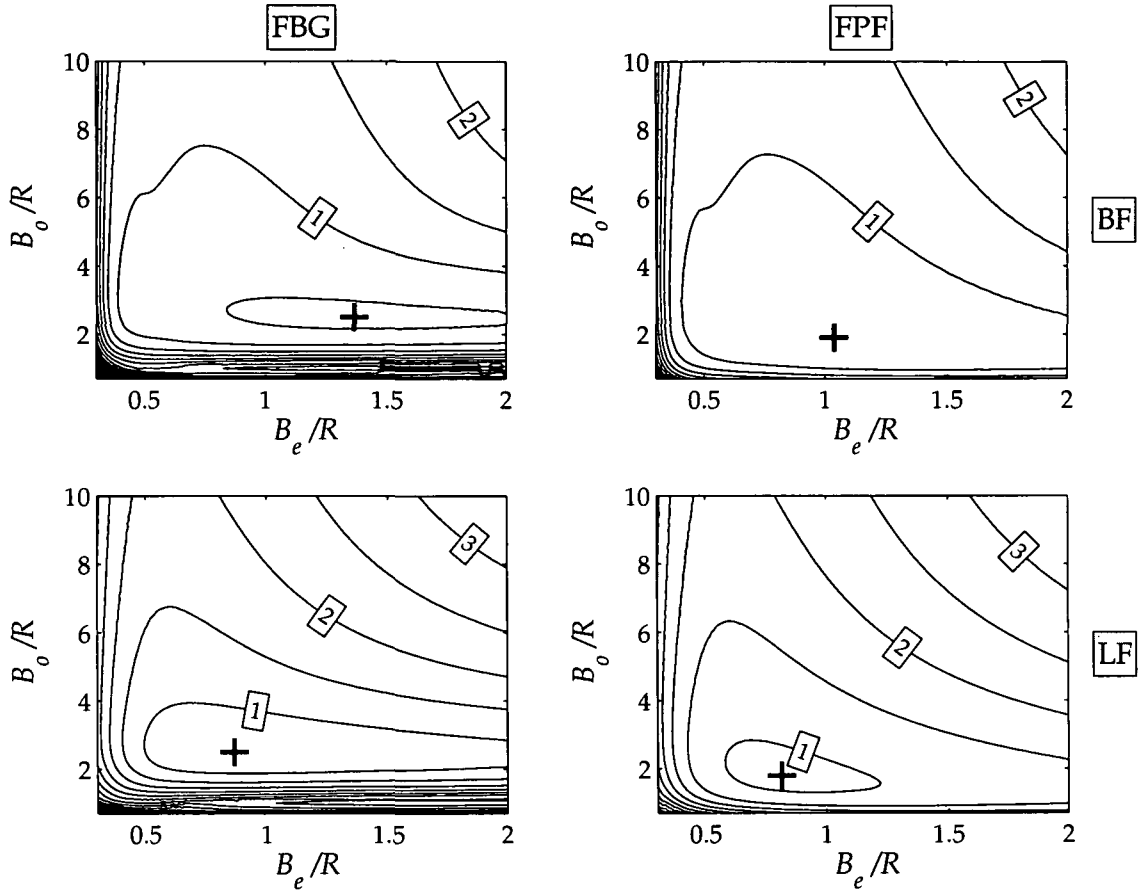


Figure 4.14: As Fig. 4.13, but for RZ coding.

		FBG	FPF		
RZ	$\gamma_{q,min}$	= 0.4 dB	$\gamma_{q,min}$ = 0.6 dB	BF	
	$B_{o,opt}$	= 2.5/R	$B_{o,opt}$ = 1.9/R		
	ΔB_o	= 6.3/R	ΔB_o = 13.7/R		
	$B_{e,opt}$	= 1.4/R	$B_{e,opt}$ = 1.0/R		
	ΔB_e	= 21.2/R	ΔB_e = 4.4/R	LF	
	$\gamma_{q,min}$	= 0.6 dB	$\gamma_{q,min}$ = 0.9 dB		
	$B_{o,opt}$	= 2.5/R	$B_{o,opt}$ = 1.8/R		
	ΔB_o	= 5.0/R	ΔB_o = 7.7/R		
$B_{e,opt}$	= 0.9/R	$B_{e,opt}$ = 0.8/R			
ΔB_e	= 4.7/R	ΔB_e = 3.1/R			

Table 4.3: As Tab. 4.2, but for RZ coding.

4.4.4 Polarization filter

Implementing a polarization filter in the receiver following the optical bandpass filter will increase the receiver sensitivity. The effect of the polarization filter is to reduce the ASE-ASE beat noise by a factor of two. However, in a well-designed receiver, the ASE-ASE beat noise is by a factor of 20 smaller than the signal-ASE beat noise. The possible sensitivity gain, therefore, is lower than 0.5 dB.

When a polarization filter is used, the SOP of the transmit and the receive signal have to be set and controlled. For this purpose all fibers should be birefringent. The additional hardware effort is not worth while the gained system performance.

If a two-way link is established, it is imperative to use as much hardware as possible for both transmission and reception to save on weight. Isolation between transmit and receive signal can be provided by using different SOP. If the system is designed such, a polarization filter is mandatory anyway.

4.4.5 Influence of transmitter properties

To this point, ideal input pulses were assumed, noise free and with infinite extinction ratio. I will now investigate the influence of certain transmitter characteristics on the receiver sensitivity. The extinction ratio will be excluded because in the next chapter measurements and simulation results concerning suboptimum extinction ratio are presented; additionally, a thorough treatment of this topic can be found in [78].

Duty cycle

In the previous sections, a duty cycle of $d = 0.33$ was used for all simulations involving RZ-coding. Here, I investigate the influence of the RZ duty cycle on receiver sensitivity. This duty cycle dependence of the RZ gain is particularly interesting for optically preamplified receivers, where – in contrast to receivers limited by signal-independent noise – the RZ gain tends to a finite limit as the receiver sensitivity approaches the quantum limit [90].

Figure 4.15 shows the receiver sensitivity penalty with respect to the quantum limit, γ_q , as a function of the inverse duty cycle $1/d$ for raised cosine RZ pulses, a fiber Bragg grating as an optical filter, and a 5th-order Bessel electrical low-pass filter. The dashed curve represents the results obtained when jointly optimizing optical and electrical filter bandwidths for each duty cycle, while the solid curve applies for optimized optical bandwidth only, keeping the electrical bandwidth constant at its optimum value for NRZ ($d = 1$), i.e. $B_e = 1R$. It can be seen that by optimizing optical and electrical bandwidths for each input pulse duration, the receiver sensitivity can be steadily increased when reducing the pulse duty cycle. The receiver sensitivity then asymptotically approaches the quantum limit, however, with the serious drawback of significantly increased demands on electrical receiver bandwidth for little gain in receiver performance. It can be seen that choosing, for example, $d = 0.1$ increases the performance by just 0.1 dB as compared to $d = 0.3$, and from the inset in Fig. 4.15 at the same time requires an electrical bandwidth of about $B_e = 5R$. This represents a very broadband receiver, especially at data rates exceeding 10 Gb/s. Additionally, optimum sampling of such short pulses is a formidable task and will place heavy demands with respect to allowable timing jitter. On the other hand, if the electrical receiver bandwidth is kept fixed at a technologically reasonable value (e.g. at the optimum bandwidth for NRZ reception), and only B_o is optimized as d is decreased, best performance is achieved for duty cycles between

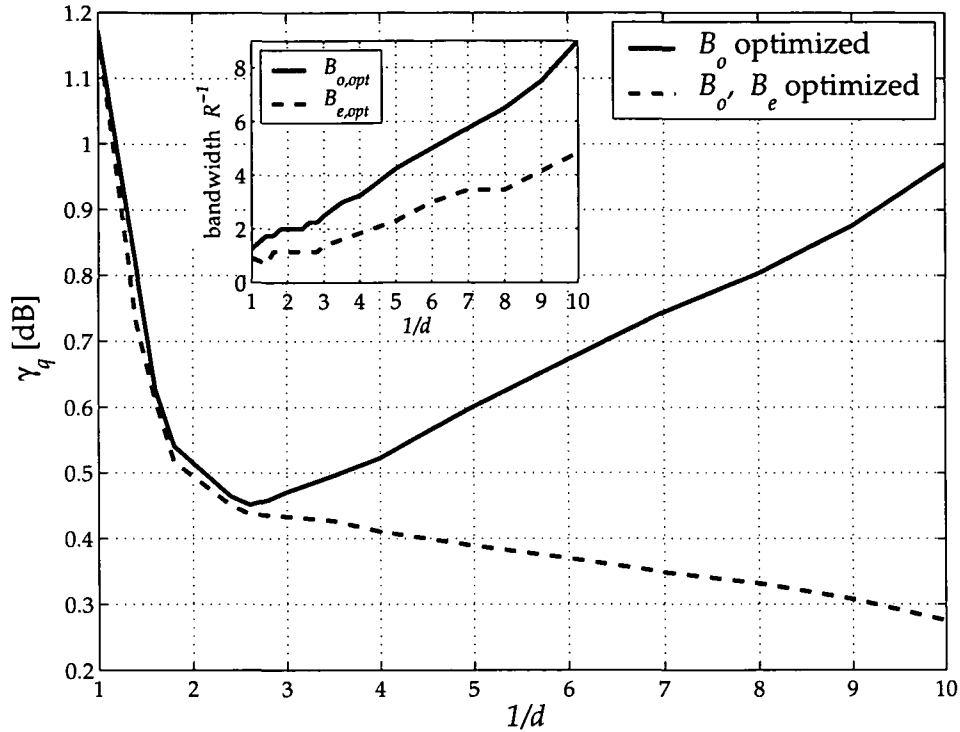


Figure 4.15: Sensitivity penalty vs. $1/d$ the inverse of the RZ duty cycle. The dashed curve represents the results for optimized optical and the electrical filter bandwidths, while the solid curve applies for fixed electrical filter bandwidth, kept at $B_e = 1R$, the optimum value for NRZ ($d = 1$). The inset shows the optimum optical and electrical bandwidths for the different duty cycle values.

0.5 and 0.33 (solid line in Fig. 4.15). Adjusting the optical filter bandwidth B_o is no problem in practice, since broad optical bandpass filters are easily available. Thus, a RZ duty cycle around 33% is optimum from a receiver point of view. Luckily, this number coincides with the duty cycle inherent to the most widely established RZ pulse source, a sinusoidally driven Mach-Zehnder modulator [32].

Figure 4.16 shows the gain of RZ coding over NRZ as a function of optical and electrical filter bandwidths. Note that the RZ gain is almost independent of the optical filter bandwidth over a wide range of B_o . For optical bandwidths in excess of $2R$ the RZ gain increases both for higher and lower electrical bandwidths than $0.6R$ (which is optimum for NRZ). This fact illustrates the advantage of RZ especially at low electrical bandwidths, which are often a limiting design parameter in high data rate systems.

Transmitter amplifier and background noise

For the results presented to this point, any external noise source was neglected. I now will quantify the influence of background radiation, as introduced in Sect. 2.5, and of ASE produced by the power amplifier at the transmitter. These noise sources have the effect that the equivalent noise figure of the system, as defined in Eq. (4.24), increases. In Fig. 4.17, the sensitivity penalty as a function of the background spectral density for absent booster amplifier

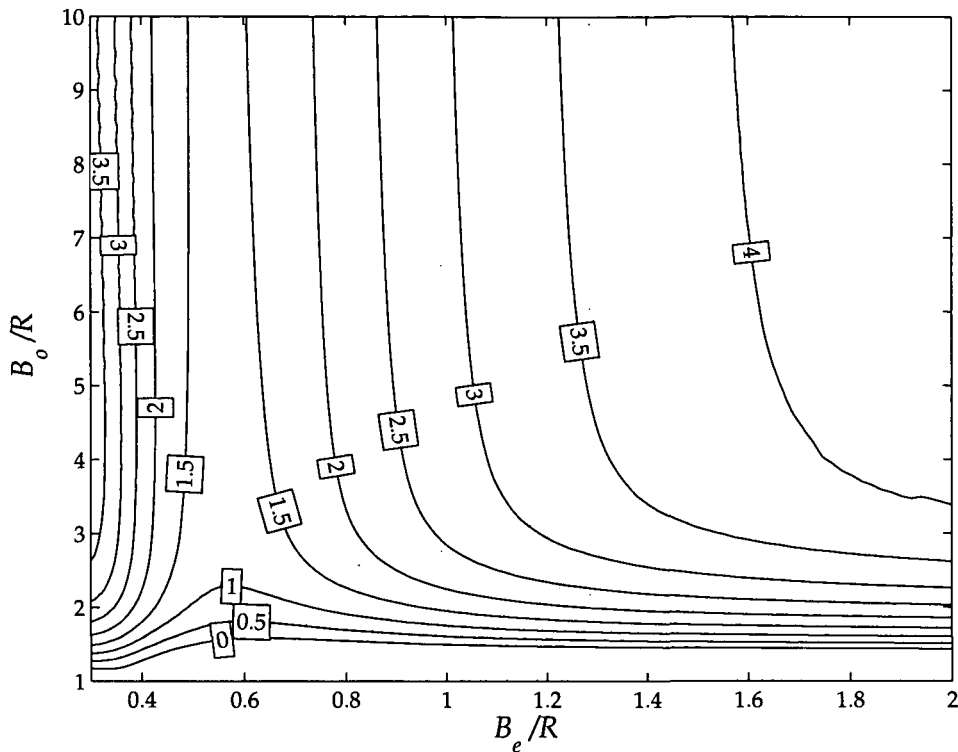


Figure 4.16: Contour plot of the sensitivity improvement due to RZ coding (RZ gain) in dB as a function of optical and electrical filter bandwidth for $d = 0.33$.

noise and of the gain of the booster amplifier for absent background radiation is shown. Results are presented for NRZ and RZ coding, however the qualitative behavior is equal for both cases (i.e. the sensitivity difference is nearly independent of the background noise). I assumed FBG and BF optical and electrical filtering, respectively. The noise figure of the booster amplifier is $F_b = 5$ dB.

No sensitivity penalty has to be expected for background radiation power spectral densities below 10^{-20} W/Hz. If a diffraction limited telescope or single mode fiber coupling is assumed, the sun, the strongest background noise source by several orders of magnitude, results in a penalty of only 0.7 dB. This makes me draw the conclusion that the influence of background radiation is negligible for optically preamplified direct detection receivers.

The lower horizontal axis represents the difference between the booster amplifier's gain G_b and the link attenuation A . The two axes are connected via

$$G_b - A = 10 \log(N_{back} 2/hf) - F_b. \quad (4.39)$$

For the presented results, the noise figure of the booster amplifier is assumed to be $F_b = 5$ dB. It is obvious that in a well designed system the link attenuation has to be higher than the transmitter booster gain by an order of magnitude unless severe sensitivity penalties will arise. However, with a coarse link budget of the system (in logarithmic scale)

$$P_R = P_T - A = P_{mod} + G_b - A \quad (4.40)$$

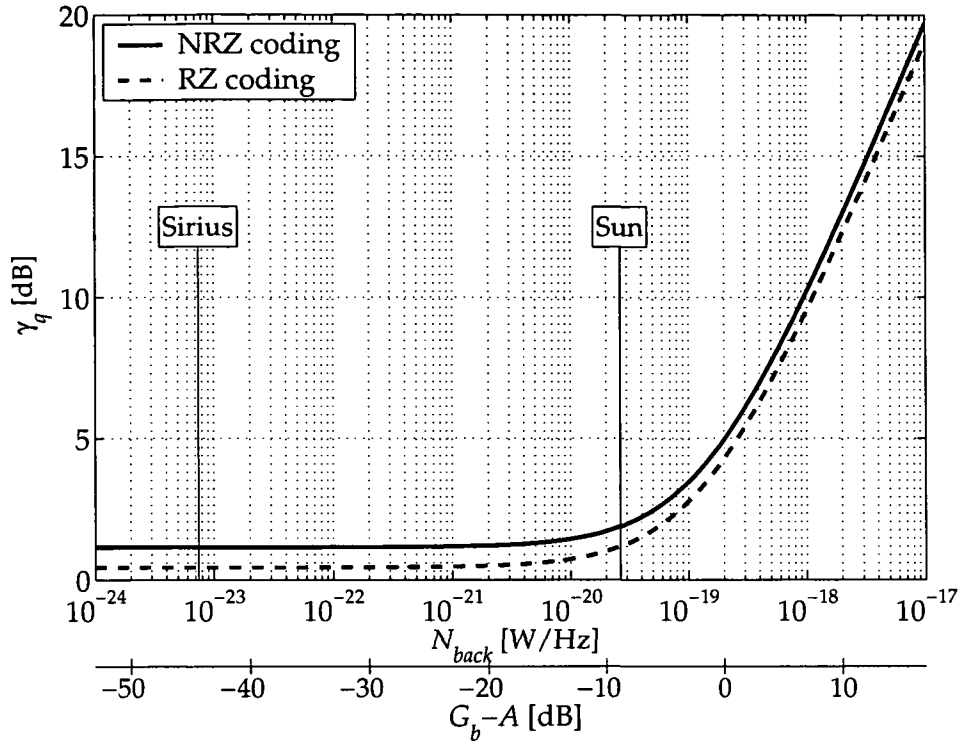


Figure 4.17: Sensitivity penalty vs. background power spectral density (upper horizontal axis) and difference between booster gain G_b and link attenuation A (lower horizontal axis) for NRZ (solid line) and RZ (dashed line) input signal. The background radiation from the Sun and Sirius (corresponding to the upper horizontal axis) is indicated for comparison.

where the power of the modulated communication signal before the booster amplifier can assumed to be in the range of $P_{mod} = 0$ dBm, and a receiver with a sensitivity close to the quantum limit (corresponding to about $P_R = -42$ dBm at a data rate of 10 Gb/s), the difference $G_b - A$ is some -42 dB. Even for less sensitive receivers or weaker communication signals, the ASE produced by the booster amplifier will cause no deterioration of the system performance.

Figure 4.17 illustrates how the receiver sensitivity to a good approximation solely depends on the equivalent noise figure defined in Eq. (4.24): At $G_b - A = 0$, the overall noise power spectral density is⁵

$$N_0 = N_{ASE,p} + N_{ASE,b}G_p/A = \frac{hf}{2}G_p(F_p + F_b), \quad (4.41)$$

where the sum of preamplifier and booster noise figure amounts to 7.2 dB, 3.9 dB higher than the noise figure of the preamplifier which is exactly the penalty shown in the figure at this point.

⁵Absence background radiation $N_{back} = 0$ is assumed.

4.5 Measurements

4.5.1 Experimental setup

To experimentally confirm the theoretical findings presented in this chapter, I set up a back-to-back communications system consisting of a (N)RZ transmitter, a preamplified direct detection receiver and a bit error ratio tester. The experiments were performed in close cooperation with my two colleagues, Martin Strasser and Martin Pauer, who used the breadboard to conduct separate experiments of which the results are laid down in their theses [77,78].

A schematic of the setup is depicted in Fig. 4.18. The purpose of the experiments was to find the dependence of the receiver sensitivity on the optical and electrical filter bandwidth and thus verify the calculations performed. Additionally, I tried to approach the quantum limit as close as possible. The setup was very complex, regardless of a possible implementation in a space-based terminal⁶.

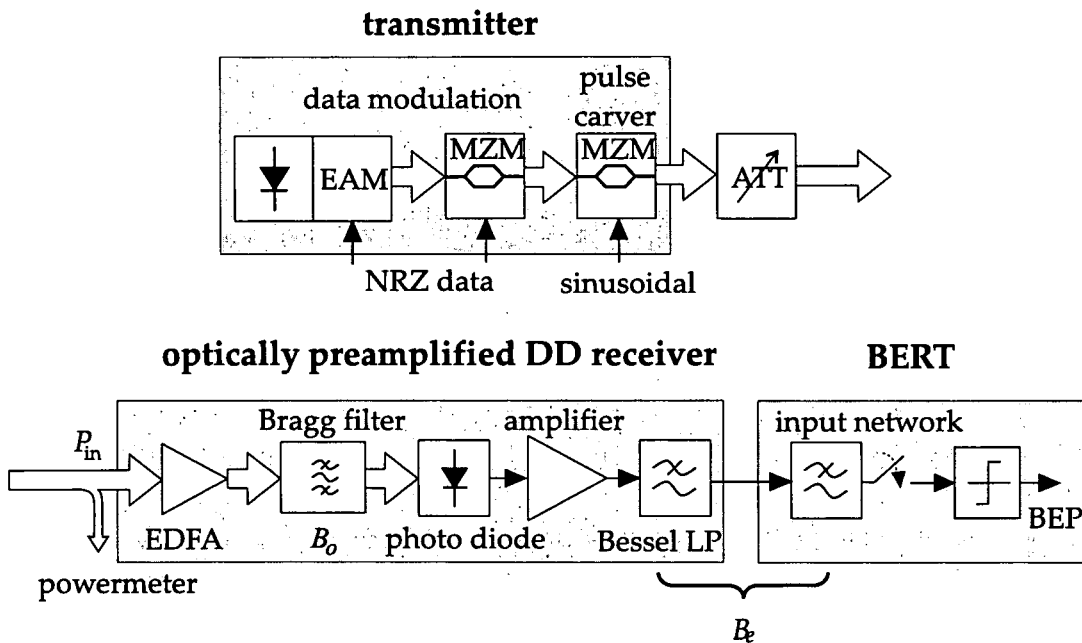


Figure 4.18: Experimental setup including (N)RZ transmitter, preamplified direct detection receiver, and bit error ratio tester (BERT).

Transmitter

A pseudo-random bit sequence (PRBS) of length⁷ $2^7 - 1$ at data rates of up to 10 Gb/s was used to modulate the light from a distributed feedback laser (DFB) operating at a wavelength of 1550 nm. To achieve high extinction ratio, the NRZ modulation was performed in two

⁶See the following chapter for experiments with a more realistic breadboard

⁷To keep simulation durations within reasonable limits, I restricted the length of the PRBS to $2^7 - 1$. For the experimental verification of our calculational results, I basically chose the same length for the measurements. A PRBS with the increased length of $2^{31} - 1$ leads to penalties of less than 0.4 dB compared to the shorter one when using the same experimental setup [99].

steps, namely using an electroabsorption modulator (EAM) integrated with the DFB, in combination with a dual-drive LiNbO₃ Mach-Zehnder modulator (MZM). For RZ coding, a third MZM was employed for pulse carving. It was sinusoidally driven to produce RZ pulses with 33% duty cycle.

Receiver

To set the receiver input power for BEP measurements, a variable attenuator was inserted between the transmitter and receiver. The received input signal was amplified by an EDFA, providing high gain (38 dB) at a low noise figure (3.3 dB). To spectrally curtail the EDFA's ASE, an optical bandpass was implemented. I employed Bragg filters of different bandwidths to optimize system performance. A broadband (50 GHz) *pin* photodiode performed opto-electronic conversion, followed by an electrical low-noise amplifier with a bandwidth of 18 GHz. A 5th order Bessel low-pass together with the finite bandwidth of the bit error ratio test set (BERT) determined the electrical bandwidth of the receiver. The bandwidth of the Bessel filter was varied in order to achieve best receiver sensitivity. The overall conversion gain amounted to 1350 V/W.

The pattern generator and the BERT were driven by the same clock signal; sampling instant and decision threshold were optimized for each measured data point.

4.5.2 Results

Using the experimental setup described, I measured the receiver sensitivity n_s for various combinations of optical and electrical filter bandwidths. The results are shown in Figs. 4.19 and 4.20, together with the corresponding simulations, expressed in terms of sensitivity penalty relative to the quantum limit, γ_q , being 40.7 photons/bit⁸.

In Fig. 4.19, I present the receiver sensitivity for NRZ and RZ coding as a function of the optical filter bandwidth B_o at a data rate of $R = 10$ Gb/s. The electrical bandwidth was kept constant at $B_e = 0.6R$ for NRZ coding, and $B_e = 0.9R$ in case of RZ coding. These values of B_e correspond to an effective electrical bandwidth, since it turned out that the finite bandwidth of the BERT input network could not be neglected. Relying on data provided by the manufacturer of the BERT, the BERT is modeled as a 1st order low-pass with a cut off frequency of $f_c = 13.5$ GHz in the simulations. With this adjustment, the agreement between measurement and simulation could be considerably improved. Note the excellent match between experimental results (bullets, triangles) and simulation (lines). In particular, I experimentally confirmed the fairly moderate sensitivity degradation for higher-than-optimum optical bandwidths, and the severe penalties for too narrow filter choices. For RZ coding, I achieved a sensitivity of 52 photons/bit (± 2 photons/bit measurement uncertainty⁹, indicated in the figure by the vertical lines at each measured point) at the optimum optical bandwidth, but using a slightly suboptimum electrical filter. This is about 1.1 dB off the quantum limit and represented, to my knowledge, the best reported receiver sensitivity at a data rate of 10 Gb/s [39, 99].

⁸The value of 40.7 photons per bit corresponds to the "physical" quantum limit to which the measurements refer, represented by the line named "exact PDF" in Fig. 4.6. The simulations are referred to the same quantum limit here, whereas the value for the model applied is 43.6 photons per bit.

⁹The measurement uncertainty of the receiver input power is $\Delta P_r = \pm 0.18$ dBm, as guaranteed by the manufacturer of the power meter employed. Because of the relation $x_{dB} = 10 \log x_{lin}$ and $\Delta x_{dB} = \Delta x_{lin} \cdot 10 / (x_{lin} \ln 10)$, the corresponding tolerance in photons per bit is $\Delta n_s = \Delta P_r n_s \ln(10) / 10$ as can be easily derived.

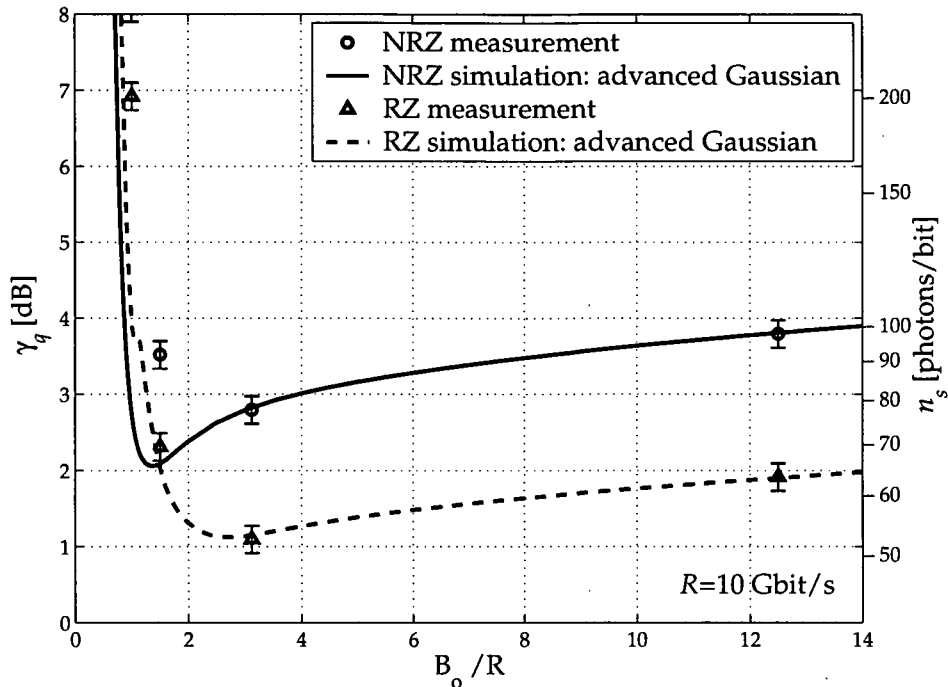


Figure 4.19: Measured (bullets, triangles) and simulated (curves) dependence of receiver sensitivity for NRZ and RZ coding on optical (B_o) and electrical (B_e) bandwidth. The results are plotted as a function of the optical bandwidth at a constant electrical bandwidth of $B_e = 0.75R$ (NRZ) and $B_e = 0.9R$ (RZ). The intervals indicated by the vertical lines represent the measurement uncertainty of ± 0.18 dB.

In Fig. 4.20, the sensitivity versus (effective) electrical bandwidth B_e at a constant optical bandwidth of $B_o = 2.86R$ for NRZ and $B_o = 3.12R$ for RZ, respectively, is presented. Additionally, I show simulation results using advanced Gaussian noise statistics (thick lines) and standard noise approximations (cf. Sect. 4.2) (thin lines). To get around the above mentioned problems associated with the limited bandwidth of the BERT input network, the measurements had to be taken at a reduced data rate of $R = 3.5$ Gb/s for NRZ, since the delicate influence of ISI on NRZ performance can only be accurately accounted for in simulation if the overall impulse response of the electronics is known sufficiently well. In contrast, the prediction of RZ performance is far less influenced by slightly uncertain electrical filter characteristics, since it is an energy truncation effect rather than ISI that limits its performance. Note that while the simulations using advanced Gaussian noise statistics (thick lines) excellently reproduce the measured results, the simulations using the frequently employed approximations for signal-ASE beat noise and ASE-ASE beat noise may be off by up to 3 dB, especially at large bandwidths B_e (thin lines).

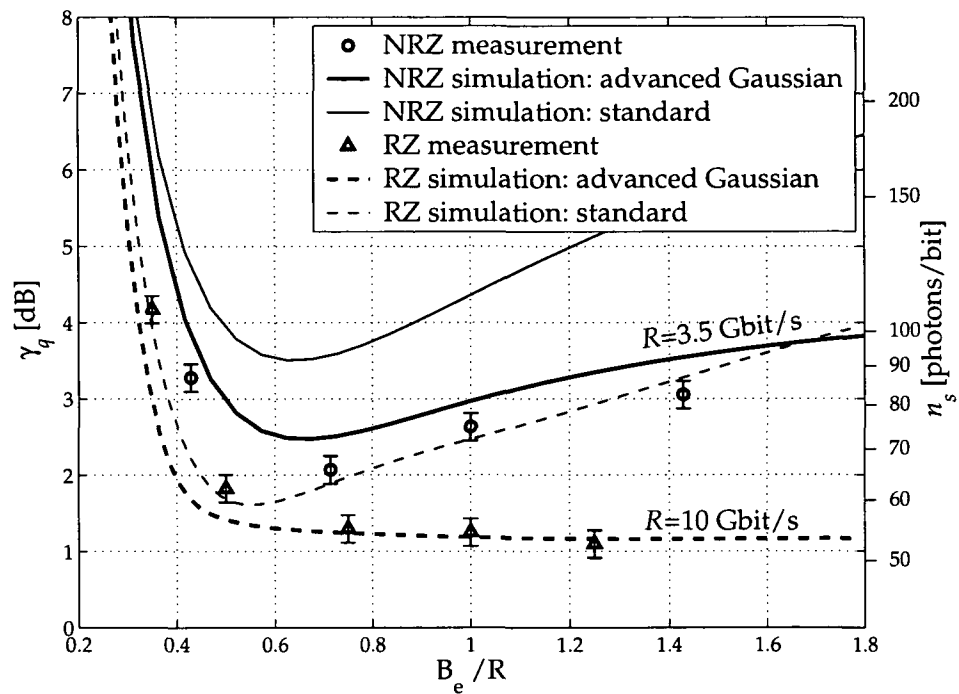


Figure 4.20: As Fig. 4.19, but here, the electrical bandwidth is varied at a constant optical bandwidth of $B_o = 2.86R$ (NRZ) and $B_o = 3.12R$ (RZ).

Chapter 5

Breadboarding a System Employing Commercial Devices

Based on the findings of the previous sections, I designed and set up a breadboard to investigate the transmission aspects of free-space optical data links based on fiber-amplification and direct detection. The breadboard consisted of a transmitter with 1 Watt optical output power and of an optically pre-amplified receiver, both operating at a wavelength of 1 550 nm and with a data rate of 10 Gb/s. The main objective was to determine the receiver sensitivity in a system where the key elements (DFB laser with integrated electro-absorption modulator, booster and preamplifier EDFAs, optical filter, receiver front-end) are implemented with commercially available devices, most of them developed for terrestrial fiber links.

The results presented are part of a project carried out for ESA. More detailed descriptions, especially on the design of the breadboard and the employed devices can be found in [29] and [103].

5.1 Breadboard Setup

According to the block diagram (Fig. 5.1) the breadboard is set up as follows:

A DFB laser (distributed feed back) with an integrated electro-absorption modulator (EAM) served as transmitter source with on-off-keying capability. The electrical signal source was a pattern generator, providing an NRZ-coded signal. For RZ coding the breadboard was modified (see Sect. 5.2.3). The modulated data signal was amplified by a polarization maintaining booster EDFA to achieve an output power of 1 W at the output of the transmitter. A polarization controller was used to provide a linear state of polarization at the input of the booster EDFA¹.

Link attenuation due to space loss was simulated in the laboratory. I chose to use the natural beam divergence of the light radiated from the single-mode fiber output of the booster EDFA in combination with a distant fiber input end for coarse and a variable pigtailed attenuator for fine attenuation adjustment.

The receiver input signal was monitored for average power. An EDFA was used to optically preamplify the receiver input signal. The signal was then optically bandpass filtered.

¹The polarization maintaining property of the booster amplifier was not exploited for this setup. By maintaining a certain SOP of the transmit signal, one could enhance the system setup by applying a polarization filter at the receiver and thus reducing the amount of noise. Isolation between transmit and receive signal could be provided by employing different SOP (cf. Sect. 4.4.4).

The optical-to-electrical conversion was done by a diode module consisting of a photodiode and a transimpedance amplifier.

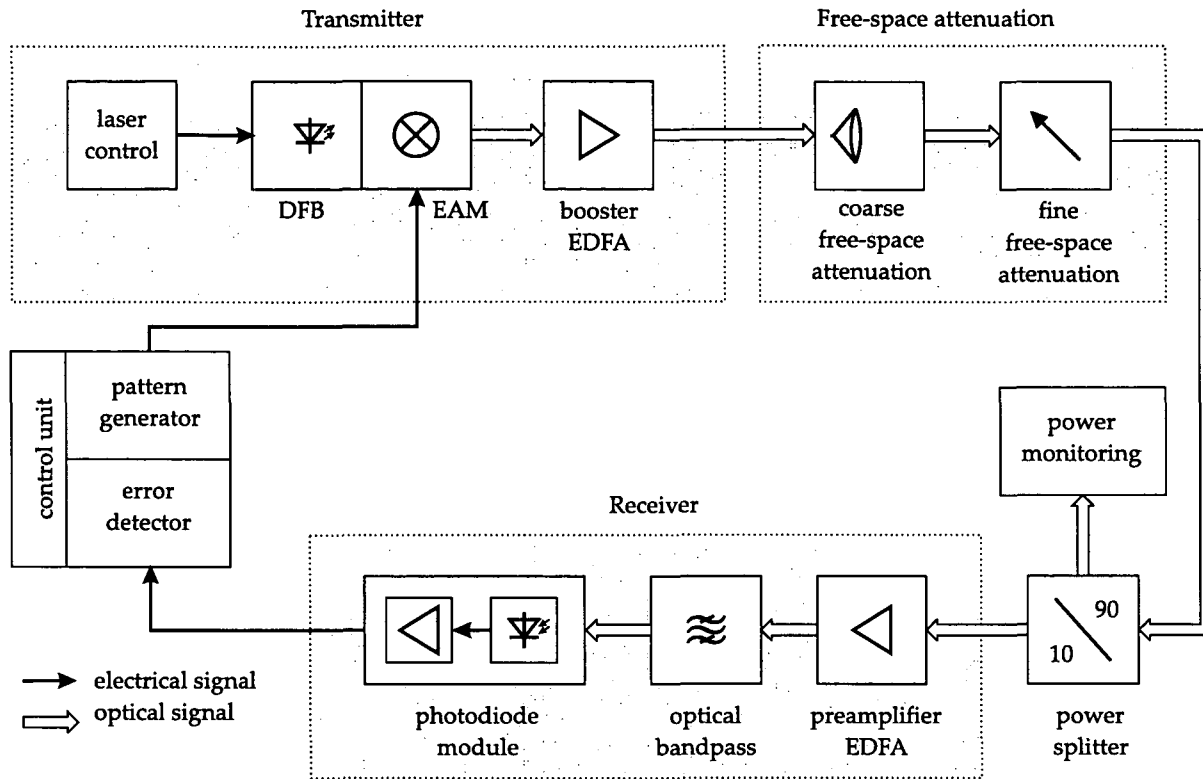


Figure 5.1: Block diagram of breadboard setup.

Transmitter

In optical sources modulated at 10 Gb/s, sufficiently low chirp and small carrier linewidth can today only be obtained by a combination of a continuously operating DFB laser and an external modulator. Two types of modulators are commercially available: electro-absorption modulators (EAM) using multiple *quantum well* structures with electrical-field-modified band gaps and Mach-Zehnder devices based on LiNbO_3 or InGaAsP using the electro-optical effect. Although Mach-Zehnder modulators provide better extinction ratios and rise-times, I chose an EAM for the breadboard. EAMs are available integrated with the DFB-lasers and therefore represent a more compact realization. The DFB/EAM module implemented is a product from ALCA TEL, type A 1915LMM, providing some 3 dBm output power and requiring 2 V modulation voltage.

A pattern generator from *hp*, type 70843A, provided an NRZ-coded signal at $R = 10 \text{ Gb/s}$ with a modulation voltage of $U_m = 1.8 \text{ V}_{pp}$ and an offset of $U_b = -0.25 \text{ V}$. The booster EDFA from IPG, type EAD-1-C-PM, has a maximum output power of 1 W and a noise figure of $F_b = 5 \text{ dB}$.

Receiver

The optical preamplifier EDFA was from OPREL, type OFP 14W. This device has a small-signal gain of $G_p = 38$ dB and a noise figure of $F_p = 3.3$ dB. This makes possible low noise amplification of the received data signal.

After the EDFA the signal passes an optical band-pass filter to reduce the broadband amplified spontaneous emission (ASE) generated by the EDFA. The results of the previous chapter show that there is an optimum bandwidth for this filter, depending not only on data rate but also on signal shape and on electrical bandwidth of the diode module. To invert the band-stop characteristic of the employed fiber Bragg gratings to the desired bandpass characteristic, a circulator (New Focus, model CIR10CN32A-00) was used. Four different Bragg gratings were implemented to experimentally verify the computational results: one from TECOS (bandwidth² $FWHH = 0.08$ nm) and three from AOS ($FWHH = 0.13$ nm, $FWHH = 0.25$ nm, and $FWHH = 1$ nm).

The most important parameters of the subsequent diode module are bandwidth, conversion gain and noise. Most commercially available products with an integrated amplifier have bandwidths in the range of the data rate. There are receivers with larger bandwidths, but they provide low conversion gain. On the other hand our simulations show that electrical bandwidths close to the data rate are optimum anyway. Both, the low cutoff frequency and the high conversion gain, make any subsequent electrical devices like a low pass filter and an RF output amplifier unnecessary. The lower cut-off frequency of the receiver should be much smaller than the spectral width of the longest "1" or "0" to be expected. Assuming pseudo random bit sequences with the length³ $N = 2^7 - 1$ this would be approximately 80 MHz. Most of the commercially available modules meet this criterion. A diode module from LUCENT (2860-C) was implemented. The bandwidth of this device is 8 GHz, the electrical noise at the output amounts to $1.8 \cdot 10^{-8}$ V/ $\sqrt{\text{Hz}}$ and the conversion gain is 3 800 V/W. An error detector from hp (70843A) was used to measure the bit error probability of the received data.

Free-space loss simulation

In the breadboard, the space loss was simulated and implemented in the following way: The booster amplifier's fiber output radiated into free space. After a distance of a few millimeters the diverging beam was partially coupled into the input fiber of variable attenuator (hp 8156A). A fiber directional coupler (from FOCCI) with splitting ratio 10:90 allows to monitor power, polarization, and wavelength. For the overall free-space attenuation I aimed at some 70 dB. Together with the booster's gain of about 30 dB, I arrive at $G_b - A \approx -40$ dB. When observing Fig. 4.17, this lets me conclude that booster ASE has no influence on the breadboard's performance.

²I will refer to optical bandwidths expressed in wavelength units with $FWHH$ (full-width half height), but use B_o in the frequency domain.

³See footnote Sect. 4.5.

5.2 Receiver sensitivity measurements and simulations

To determine the highest possible receiver sensitivity with the setup described, I optimized the following parameters:

- laser drive current I_d ,
- laser emission wavelength λ ,
- peak-to-peak modulation voltage U_m ,
- modulator bias voltage U_b ,
- bandwidth of the optical bandpass filter, $FWHH, B_o$.

Sampling instant and decision threshold of the error detector had to be optimized for each measurement separately. A pseudo random bit sequence with $2^7 - 1$ bits was transmitted.

A bit error probability of $BEP = 10^{-6}$ was aimed at. All results are given in terms of the sensitivity penalty relative to the quantum limit obtained from the exact calculation ("exact PDF" in Fig. 4.6), amounting to $n_q = 26.7$ photons per bit

5.2.1 Simulation

Parallel to the measurements, I performed simulations for comparison with the results obtained by the measurements. For this purpose, the simulation method presented in Chapt. 4 was applied with parameters adapted to the breadboard setup addressed in this chapter (cf. Tab. 5.1).

	Symbol and Value	Description
input signal	$R = 10 \text{ Gb/s}$ $N = 2^7 - 1$ $\lambda = 1549.16 \text{ nm}$ $\zeta = 10.81 \text{ dB}$ $M_{pol} = 2$ $N_{back} = 0 \text{ W/Hz}$	data rate length of the PRBS wavelength extinction ratio number of polarization modes spectral density of the background radiation
optical amplifiers	$G_b = 30 \text{ dB}$ $F_b = 5 \text{ dB}$ $G_p = 38 \text{ dB}$ $F_p = 3.3 \text{ dB}$	gain of the booster EDFA noise figure of the booster EDFA gain of the preamplifier EDFA noise figure of the preamplifier EDFA
optical filter	$FWHH, B_o$ $IL = 5 \text{ dB}$ $SLSR = 11 \text{ dB}$ $ \kappa = 3 \text{ cm}^{-1}$	bandwidth insertion loss at center wavelength (including circulator) side lobe suppression ratio of the fiber Bragg grating coupling coefficient of the fiber Bragg grating
diode module	$C = 3800 \text{ V/W}$ $NEP = 4.74 \cdot 10^{-12} \text{ W}/\sqrt{\text{Hz}}$ $B_e = 8 \text{ GHz}$	conversion gain of the diode module noise equivalent power of diode module electrical bandwidth of the receiver module

Table 5.1: Parameters used for simulations.

5.2.2 Measurements with NRZ-coded input signal

The receiver sensitivity penalty γ for four different filters is shown in Fig. 5.2 as a function of the laser center wavelength. For these results, the setting of the modulator bias and the modulation voltage was such that the extinction ratio amounted to $\zeta = 10.8$ dB.

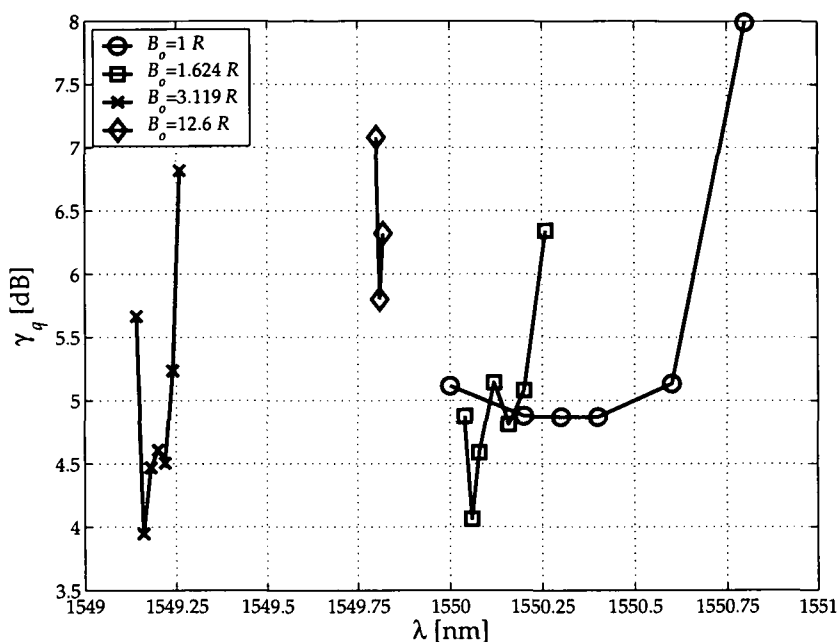


Figure 5.2: Receiver sensitivity penalty γ_q for different optical bandpass filters vs. laser wavelength at $BEP = 10^{-6}$. The extinction ratio is $\zeta = 10.8$ dB.

The receiver sensitivity as a function of the optical filter bandwidth can be extracted from this figure. Figure 5.3 shows this dependence explicitly together with the corresponding simulation results. The four values for the different filters are presented together with the interval of measurement uncertainty of $^4 \pm 0.18$ dB. The filter with $B_o = 16.24$ GHz appears to be the best choice, the filter with $B_o = 31.19$ GHz leads to comparable performance. The broadest filter is suboptimum because of the high amount of noise due to ASE passing to the diode module. The consequence of a too small filter bandwidth is pulse distortion leading to ISI and signal energy rejection, resulting in a clear sensitivity penalty.

Increasing the filter bandwidth from its optimum value results in less sensitivity degradation than decreasing it by the same amount. Therefore, broader filters have to be preferred.

Taking into account the chosen scale of the ordinate, the simulation agrees well with the measurement. The deviations are some 0.5 dB for broad filters, 0.1 dB for the optimum bandwidth and about 1 dB for the narrowest filter.

Deviations for the two filters with the smaller bandwidths may be caused by suboptimum laser wavelength setting and filter modeling. Any asymmetry of the filters was not simulated. Such an asymmetry leads to distortion with effects equal to that of intersymbol interference, resulting in higher optimum bandwidth. Other reasons for the discrepancy may be imperfect modeling of the electrical filter characteristics: Both the diode module and the

⁴For the ANRITSU power meter used, this is the accuracy guaranteed by the manufacturer.

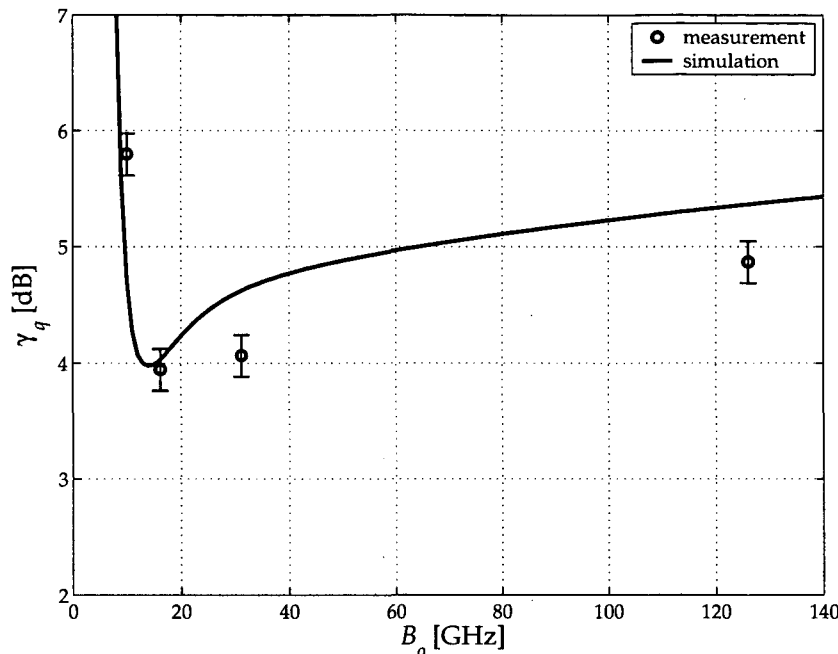


Figure 5.3: NRZ coding: Receiver sensitivity penalty γ for the four optical filters available at $BEP = 10^{-6}$. The intervals indicated by the vertical lines represent the measurement uncertainty of ± 0.18 dB. The extinction ratio is $\zeta = 10.8$ dB.

bit error detector have been modeled as Bessel filters after measuring the magnitude of the transmission functions. No information on the phase was available. Another reason for the difference between measurements and simulation could be attributed to imperfect modeling of the transmit signal's pulse shape.

To determine the influence of the extinction ratio of the transmit pulse, the modulation voltage and the bias of the modulation voltage were varied and the bit error probability vs. receiver input power was measured. Figure 5.4 shows the sensitivity as a function of the extinction ratio ζ . The maximum extinction ratio I could achieve was $\zeta = 11.8$ dB. This led to a receiver sensitivity penalty relative to the quantum limit of $\gamma_q = 3.2$ dB.

In Fig. 5.4 I also included simulation results. Measurements and simulation were performed for an optical bandwidth of $B_o = 16$ GHz, they differ by less than 0.5 dB. The deviation of the measurement point for $\zeta = 11.8$ dB may be caused by the noise of the oscilloscope used for extinction ratio measurements, which introduces measurement inaccuracy especially for high extinction ratios, where the zero-bit power is low. Another issue is the chirp (i.e. signal frequency fluctuations) introduced by the EAM which lead to performance degradation, especially for the narrow optical filter employed here.

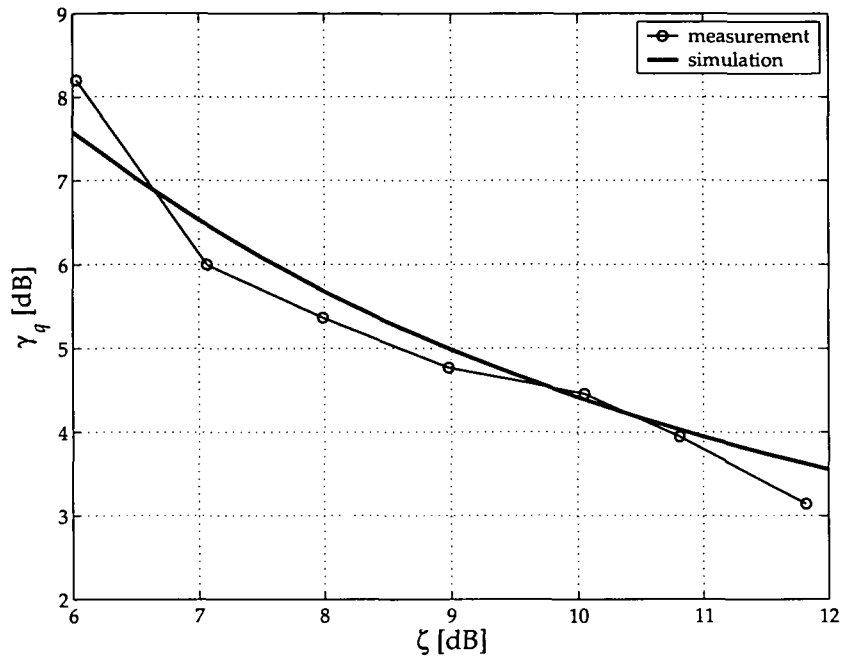


Figure 5.4: Receiver sensitivity penalty γ vs. extinction ratio ζ for the optical filter bandwidth $B_o = 16.24$ GHz at $BEP = 10^{-6}$.

5.2.3 Measurements with RZ-coded input signal

To generate an RZ-coded transmit signal some modifications in the transmitter were necessary (see Fig. 5.5). The EAM now serves as data modulator (cf. insets (a) and (b)), while a Mach-Zehnder modulator (MZM) fed with a sinusoidal voltage of frequency equal to the data rate acts as NRZ-RZ converter (inset (c)). The bias of the MZM was chosen such that the resulting pulse form is a sine-square shaped RZ pulse with a duty cycle of about $d = 0.5$, as shown in inset (d) of Fig. 5.5. The duty cycle is defined as the ratio of pulse duration (full width half maximum) and bit duration T_{bit} (cf. Sect. 4.1). A polarization control was implemented to properly set the input SOP of the MZM.

For RZ-coded signals, the same measurements and simulations as for NRZ were performed. Figure 5.6 presents the measurement and calculation results for the receiver sensitivity as a function of the optical filter bandwidth for RZ coding (the results for NRZ coding are also displayed for comparison). In contrast to NRZ coding, the experimentally determined optimum filter bandwidth is now $B_o = 31$ GHz. The corresponding sensitivity is some 1 dB better than that for NRZ coding in case of equal extinction ratio of $\zeta = 10.8$ dB but optimum filter bandwidth.

For RZ coding the difference between the measurements and calculation is less than 0.5 dB for large optical filter bandwidths. For narrow filters the differences are larger which may be explained by imperfect pulse and filter modeling. In both the simulation and measurement, RZ leads to better system performance.

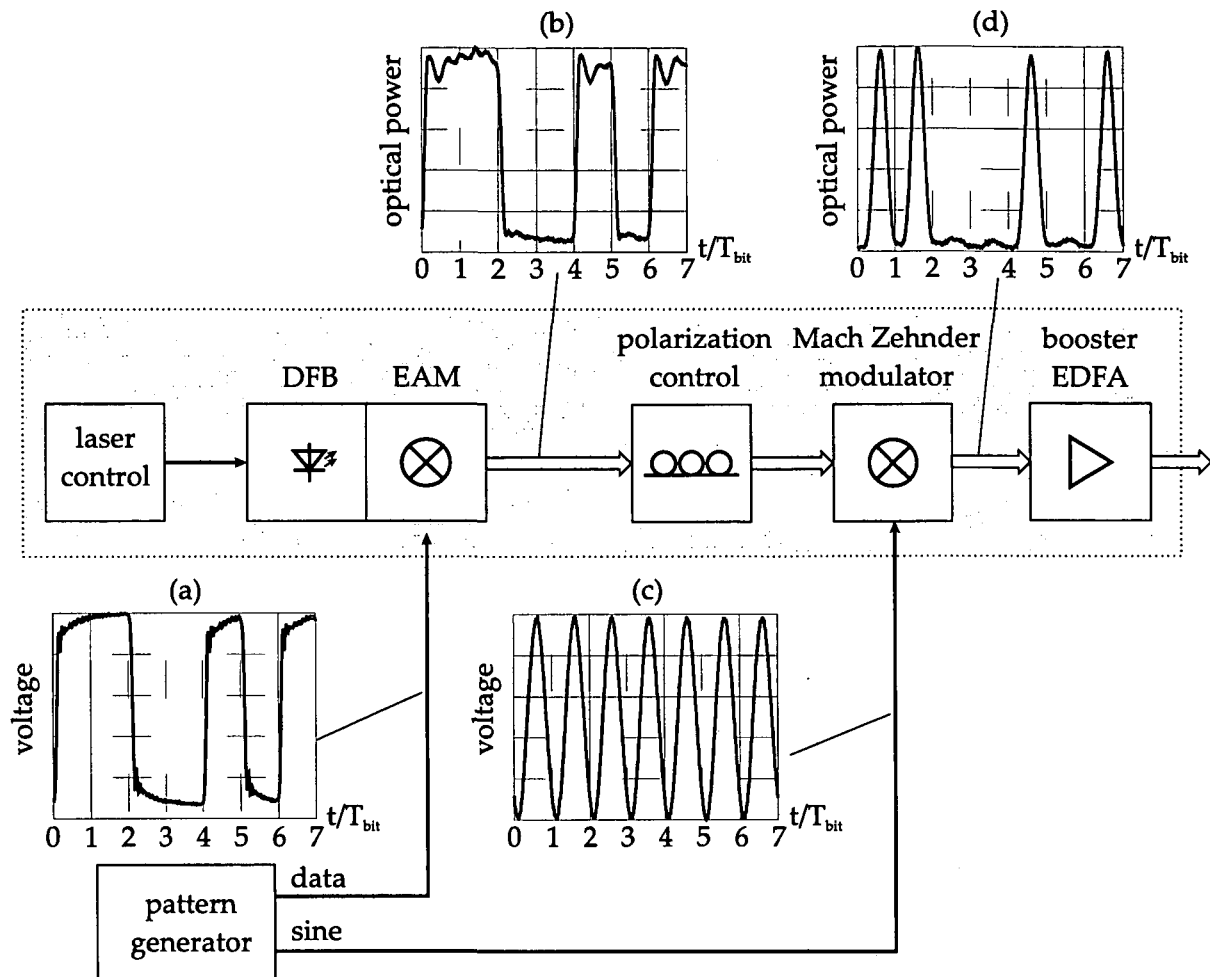


Figure 5.5: Block diagram of the breadboard transmitter for RZ modulation. The insets (a) and (c) show the modulation voltages for the electro-absorption modulator (EAM) and the Mach-Zehnder modulator, respectively. (b) gives the optical power after the EAM, while (d) shows the RZ coded transmit signal. (T_{bit} ... bit duration).

5.3 Discussion

5.3.1 Transmitter

Measurement and simulation results show that one of the most critical parameters for system performance is the transmit pulse extinction ratio ζ (cf. Fig. 5.4). A pronounced sensitivity degradation is to be expected when ζ becomes less than 10 dB. To avoid this, the modulation voltage, the modulator bias, and the laser drive current have to be adjusted and controlled precisely. With the DFB+EAM modules investigated here, the maximum extinction ratio obtained was 11.8 dB. A better pulse shape of the electrical signal driving the modulator than that generated by the available pattern generator may result in less signal distortion and a higher extinction ratio. An additional modulator, driven with the data signal, may improve the extinction ratio and thus lead to higher system sensitivity.

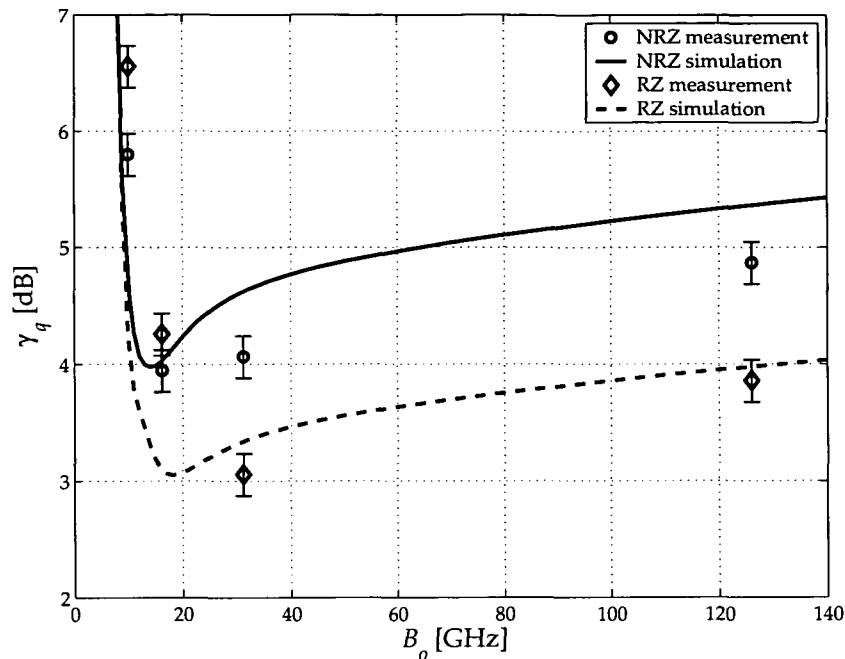


Figure 5.6: NRZ and RZ coding: Calculated receiver sensitivity penalty relative to the quantum limit, γ_q , vs. optical filter bandwidth B_o at $\text{BEP} = 10^{-6}$. The circles and diamonds represent the measurement results obtained with the available optical filters for NRZ and RZ coding, respectively.

Both measurements and simulation showed that laser emission wavelength deviations of 20% of the bandwidth B_o of the optical filter result in a sensitivity penalty of 1 dB. For the breadboard, a temperature stabilized laser diode mount from ILX Lightwave (type LDT 5412) was used to control the laser wavelength, providing sufficient wavelength stability. The optimum optical filter bandwidth for the breadboarded system is in the range of 15 to 20 GHz.

Considering the link level budget assumed for the breadboard, the influence of the booster EDFA's ASE is negligible. For small link distances (i.e. lower path attenuations) the booster EDFA's noise may become the dominating parameter influencing the system performance (cf. Sect. 4.4.5 and [86]).

Because of the high output power and the high power density at the output fiber of the booster EDFA, precautions have to be undertaken to avoid the fiber facet getting contaminated, which could result in totally damaging the cleaved facet.

5.3.2 Receiver

In a well-designed setup the preamplifier EDFA causes the dominating noise in the receiver. Therefore its noise figure should approach the theoretical limit of 3 dB as closely as possible.

The optical bandpass was a critical component in the receiver setup. Its temperature dependent center wavelength and its bandwidth strongly influence the receiver sensitivity. Considering the results presented in Fig. 5.2 as well as temperature drift of the filter center wavelength and variations of the optical carrier frequency due to temperature changes and

possibly Doppler shift, it is recommended to use filters with higher than optimum bandwidths. Another, technically-demanding, approach to overcome these problems is to actively control the center wavelength of the filter.

The insertion loss of the circulator/grating combination plays a minor role because it attenuates the optical signal in the same way as the optical noise, and because the electrical noise is, in general, negligible.

For the breadboarded system, the data clock signal was taken from the pattern generator and fed to the error detector. In a real system, a clock recovery of its own will have to be implemented, as it is standard in terrestrial fiber systems. The sampling instant and the decision threshold for the error detector were optimized manually for every measurement. The sampling instant, which is not that critical, could be fixed relative to the recovered clock signal. Using an automatic power control at the input of the photo-diode module could mitigate the problem of threshold optimization, since the decision threshold could then be set once and its optimum value would not change significantly for different receiver input power levels.

5.4 Effects leading to the difference to the quantum limit

The best sensitivity results achieved in experiment and simulation are some 3.1 dB worse than the quantum limit. I investigated the individual contributions of the effects leading to this difference by performing calculations with modified simulation parameters.

Setting the electrical noise and the noise from the booster EDFA zero, assuming ideal noise properties of the preamplifier EDFA ($F_p = 3$ dB, polarization filter implemented) and the transmit pulse (rectangular with infinite extinction ratio) leads to 0.5 dB sensitivity penalty relative to the quantum limit. The reason for this is that the optical Bragg filter and the electrical Bessel filter are not matched to the signal pulse shape.

For a realistic noise figure of the preamplifier EDFA ($F_p = 3.3$ dB), a receiver setup without polarization filter, realistic electrical noise ($N_0 = 1.8 \cdot 10^{-8}$ V/ $\sqrt{\text{Hz}}$) and including the influence of booster ASE, a 1 dB sensitivity penalty has to be expected.

Taking into account, finally, the measured extinction ratio and pulse shape in the simulation lead to a sensitivity penalty of 3.1 dB. This indicates that the transmit signal shape is the most important parameter influencing system performance.

Chapter 6

Quantum Communications in Space

Within the last years there evolved several possibilities of making use of nonclassical quantum effects for communications applications that would not be possible classically [104,105]. One example is *Quantum cryptography*. This application takes advantage of entanglement and the *no-cloning theorem*¹ to share a key between two partners of which no other party can gain any information [106].

Many aspects of quantum communication in space are common with classical optical free-space communication. Examples are pointing, acquisition, and tracking, link loss and availability, background radiation, and influence of the atmosphere. In the following, I will outline an experimental scenario for free space quantum key distribution (QKD) with entangled photons employing the ISS and analyze critical parameters.

6.1 Principles of quantum key distribution with entangled photons

Truly secret communication has been dreamt of throughout history. When transmitting an encrypted message, there are two possibilities for an eavesdropper to gain the information: breaking the cipher or obtaining the key. The first attack can be repulsed by using a random key and applying the Vernam cipher [107]. In 1949 Shannon proved that a message coded this way is safe provided that the key is secret, truly random, has the same length as the message, and is used only once [108].

The problem of secret key distribution can be overcome by using quantum physics. The first quantum protocol for transmission of a random, secret key, BB84, was proposed by Bennett and Brassard in 1984 [109]. While this protocol relies on single photon quantum states, I will discuss the possibility of employing entangled photons for this purpose in the following. One advantage of using photon pairs is that the deteriorating effects of dark counts and background counts can be almost eliminated because there are two spatially separated receivers and ideally only photons identified to belong to a pair are considered. Furthermore, the safety against eavesdropping is enlarged [106] and more flexible scenarios employing an independent transmitter can be established (cf. Sect. 6.3).

¹As a general rule, no quantum state can be copied with arbitrary precision [104].

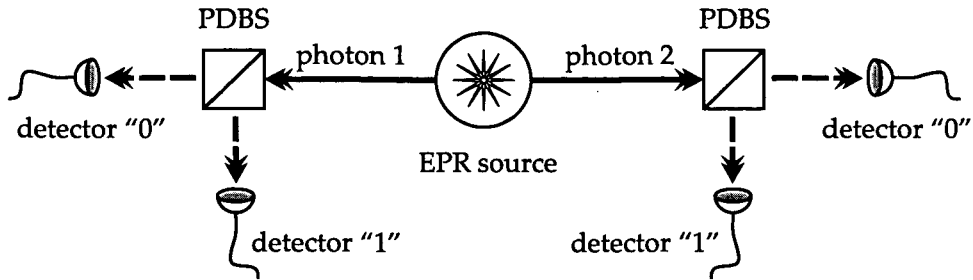


Figure 6.1: Principle of entanglement (PDBS ... polarization dependent beam splitter).

6.1.1 Quantum entanglement

The term “entanglement” was first introduced by Erwin Schrödinger [110]. Its counterintuitive conceptual implications have been pointed out in the seminal paper by Einstein, Podolsky, and Rosen (EPR) [111]. These authors prove that quantum entanglement leads to a contradiction of classical assumptions underlying a complete physical theory, namely locality and realism.²

Entanglement is a very strong form of correlation. If, e.g., two particles are maximally entangled, all properties of the individual particles are encoded completely in the correlations between them. As a consequence, the property of each particle remains undefined (up to its measurement). Consider two particles emitted simultaneously by a source (a so called *EPR source*) to be entangled with respect to a certain property. Through the measurement of one of the two particles, not only the property of the measured particle is obtained but also, instantaneously, the property of the distant particle.

The scenario is outlined in Fig. 6.1 schematically for two photons entangled with respect to polarization. After being generated by the source, the photons impinge on one of the detectors after passing a polarization dependent beam splitter. As long as the other photon has not been detected the result of the measurement is perfectly random. If one photon is detected, the other instantaneously takes on the orthogonal polarization, leading to an inverse measurement result, provided that the same measurement basis (e.g. $0^\circ/90^\circ$ SOP) is applied. This is true for any orientation of the polarization dependent beam splitter chosen in the experiment [104].

6.1.2 Quantum key distribution protocol

For distributing a secret key between two partners A(lice) and B(ob) by employing entangled photons a setup similar to the one shown in Fig. 6.1 may be used. To prevent eavesdropping, the measurement basis has to be switched arbitrarily between at least two states of polarization (e.g. $0^\circ/90^\circ$ and $+45^\circ/-45^\circ$, relative to a predefined reference). The source emits a series of entangled photons directed to the two receivers. When the photon of the first pair arrives at Alice, she chooses randomly one basis and receives a random result. If Bob incidently chose the same basis, he deterministically obtains a result orthogonal to the one Alice

²In 1964 John Bell provided an experimentally accessible bound on the correlations imposed by a local realistic theory, the so-called Bell inequality, and showed that quantum theory violates these bounds [112]. The first experimental verification of a violation of Bell’s inequality by entangled photons has been achieved by Freedman and Clauser [113] and has later been confirmed under more stringent conditions [114, 115].






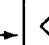
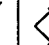
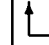
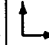
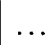


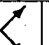

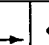
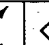

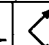
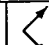
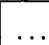
Alice's basis											...
Alice's result	0	1	0	1	1	0	0	0	1	1	...
Bob's basis											...
Bob's result	1	0	1	0	1	0	1	1	0	1	...
key	0		0	1			0				...

Table 6.1: Creation of the secret and random key in a QKD system.

did. If he chooses a different basis, his result is random³ (cf. Tab. 6.1). After receiving a photon, Alice and Bob exchange the basis settings via a classical communication channel. Each of the two partners compares his settings with the settings of the other and deletes all bits where the settings were different. The remainder is the *sifted* key (one of the two has to invert his result, in Tab. 6.1 it is Bob). Alice and Bob now can cipher their message using this key and then transmit it over classical communication channels.

If an eavesdropper (Eve) wants to get the key, she would try to catch one of the entangled photons. But according to the no-cloning theorem, she is not able to obtain the state of the photon and produce a perfect copy. If she detects one of Alice's photons and sends a different photon not entangled to Bob's one to Alice, the correlation between Alice's and Bob's result vanishes. This can easily be checked by sharing a subset of the key via public channel and compare the results. If the error probability exceeds a certain value, the presence of an eavesdropper can be assumed [104, 105].⁴

6.2 State-of-the-art of quantum key distribution

The first experimental demonstration of QKD was achieved in 1989 by Bennett and Bessette [117], employing a protocol based on single photons. Quantum key distribution based on entangled photons has been experimentally realized for the first time by Jennewein et al. [116].

Usually the partners willing to exchange private information are spatially separated, they may reside in, e.g., different cities. There are two ways of distributing a quantum key over considerable distances: the first is to establish a free-space link and the second is to use silica fibers as channel for the photons. The latest realizations of QKD (cf. Tab. 6.2) rely on the latter possibility and were able to bridge some 100 km, limited by photon absorption [118]. In-line amplifiers or regenerators as employed in classical optical transmission systems cannot be used for quantum communication protocols because any form of amplification destroys the unique properties of the photons, i.e. entanglement. First QKD systems are commercially available by now (e.g. [119, 120]). Table 6.2 lists some recent QKD experiments.⁵

³Of course, the individual outcome for Bob alone (i.e. without knowing Alice's setting) is always completely random. Only the correlations are deterministic!

⁴There are more sophisticated methods to detect Eve, based on violating Bell's inequality, laid down in e.g. [106, 116]

⁵When comparing different QKD schemes, one may cite the bit rate of the corrected key and the link distance. It is, however, equally important to take into account any difference in the photon sources, the propagation medium, and in protocols.

group	ref.	channel	net key rate	distance	year
Geneva University	[121]	fiber	—	10 km	1998
Los Alamos National Laboratory	[122]	free-space	3 kb/s	1.6 km	1999
University of Vienna	[116]	fiber	530 b/s	350 m	2000
QinetiQ	[123]	free-space	71 – 685 b/s	1.9 km	2001
Geneva University, ID-Quantique	[124]	fiber	44 – 4 300 b/s	67 km	2002
Los Alamos National Laboratory	[125]	free-space	400 b/s	9.5 km	2002
CNRS (France)	[126]	free-space	7.7 kb/s	50 m	2002
LMU Munich, QinetiQ	[127]	free-space	1.5 – 2 kb/s	23.4 km	2002
Toshiba	[128]	fiber	—	100 km	2003
MagiQ	[119]	fiber	—	120 km	2003

Table 6.2: QKD experiments.

A state of the art entangled photon source has typical dimensions of $100\text{ cm} \times 80\text{ cm} \times 25\text{ cm}$. Space qualification has not yet been reached. Required developments include space qualification of the pumping diode laser, further miniaturization and stabilization of the optics modules and that of radiation-hard optics. Space qualified Si-APD detectors have been used in the SILEX experiment, however, they do not operate in the single-photon counting mode.

In order to establish quantum cryptography networks on a global scale, it is essential to distribute single photons or entangled photons over distances exceeding the ones realizable in fiber systems by more than an order of magnitude. Optical free-space links could provide a unique solution to this problem since they allow in principle for much larger unamplified propagation distances of photons due to the low absorption of the atmosphere in certain wavelength ranges. Free-space optical links have been studied and successfully implemented already for several years for their application in quantum cryptography based on single photons [125, 127, 129]. Also the possibility of using space-based terminals has been considered [130–133]. Links exploiting the benefits of entanglement-based QKD, especially employing the ISS as platform for a terminal were discussed recently [58, 134–136] and are pursued in ongoing ESA studies [137].

6.3 Quantum communication scenarios comprising the ISS

One may distinguish the cases in which the transmitter of entangled photons is located on ground or aboard the ISS. These scenarios will allow various applications to be discussed below.

6.3.1 Earth-based transmitter terminal

The scenarios involving an Earth-based transmitter terminal allow to share quantum entanglement between a ground station and the ISS or between the ISS and another satellite. In the most simple case, a straight uplink to one ISS-based receiver (see Fig. 6.2 a) is used to perform secure quantum key distribution between the transmitter and the receiver. Here, one of the photons of the entangled pair is being detected right at the transmitter site. Shared entanglement between two distant parties can also be achieved by directing each of the photons of an

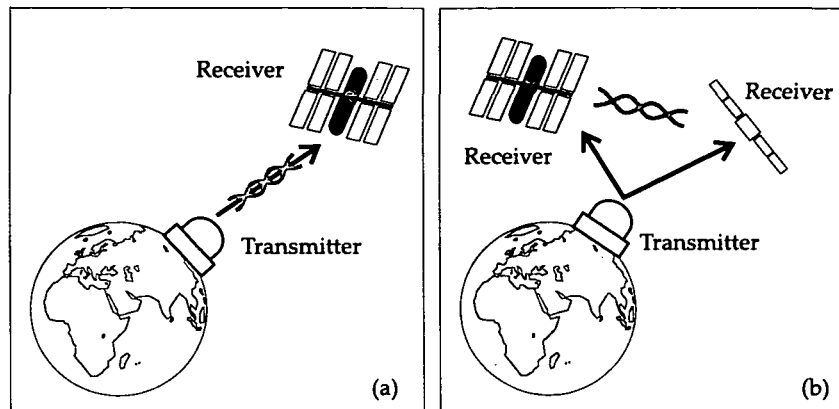


Figure 6.2: Scenarios for quantum communication with Earth-based transmitter terminals.

entangled pair either towards another Earth-based station and the ISS or towards two separate space-based receivers (see Figs. 6.2 b). However a secure link between two satellites on its own seems to be not very promising, but could serve as part of a more complex scenario.

6.3.2 ISS-based transmitter terminal

A transmitter with an entangled photon source placed on a space-based platform not only allows increased link distances because of reduced influence of atmospheric turbulence (see Sect. 2.3) but also leads to more flexible scenarios. A simple downlink allows to establish a QKD protocol (see Fig. 6.3 a). In this configuration, a key exchange between two ground stations is also possible. To this end each of the two ground stations has to establish a separate quantum key with the ISS at different times. Since the space terminal has access to both keys, it can transmit a logical combination of the keys which can then be used by either ground station or both ground stations such that they arrive at the same key. Note that the key is not generated simultaneously at both receiver stations. By applying this scenario a quantum key exchange can be performed, in principle, between arbitrarily located ground stations at different times.⁶ However, this scheme imposes the same high security constraints onto the source as are required for the two ground stations. The use of entangled states sent simultaneously to two separate ground stations (Fig. 6.3 b) or a ground station and a satellite (Fig. 6.3 c) allows instantaneous key exchange between two communicating parties on ground and guarantees that the transmitter has no information about the shared key. Therefore, no security requirement has to be imposed onto the source; in principle, the source could even be in the hands of a potential eavesdropper [131, 134, 135].

6.4 Quantum key distribution between two ground stations using the ISS

Most of the potential applications will ask for secure communication between two ground-based partners. It is therefore the aim to distribute a quantum key between two ground stations (configuration (c) of Fig. 6.3). This scenario has several advantages compared to the

⁶Provided that a link between the ISS and the ground station is not impossible due to the geographical position of the ground station.

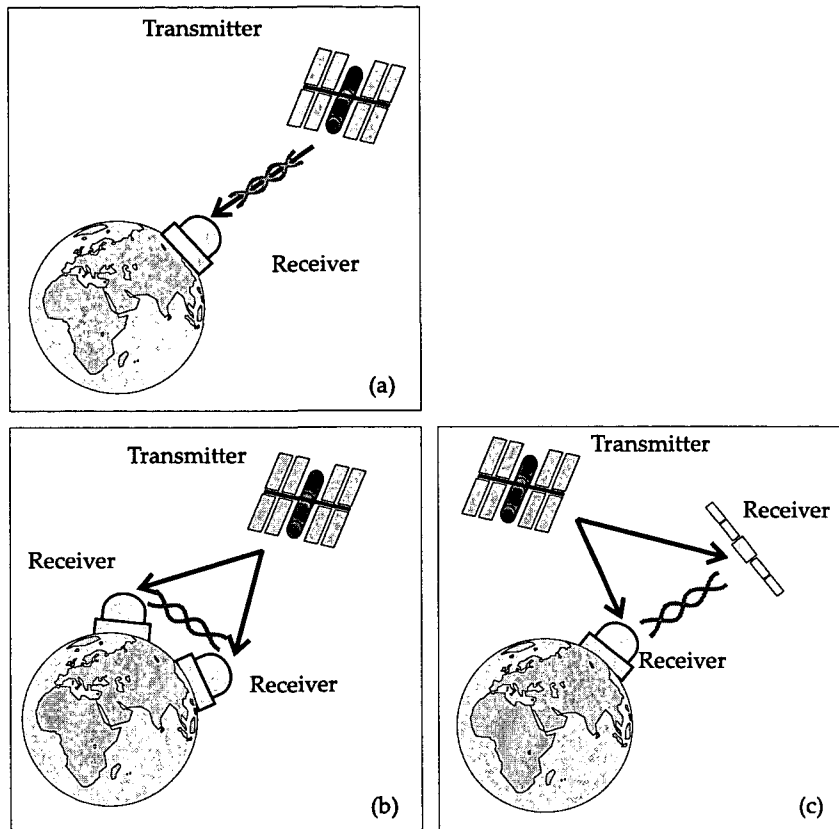


Figure 6.3: Scenarios for quantum communication with space-based transmitter terminals.

others discussed in Sect. 6.3: The transmitter can by no chance obtain any information about the key the receivers exchange. In addition, the scenario provides high flexibility, because none of the two partners sharing the secret key has to possess an entangled-photon source. One and the same transmitter may distribute keys to several pairs of communication partners at different times. If the transmitter terminal is additionally equipped with a reception module, QKD between the transmitter and a ground station (scenario (a) from Fig. 6.3) can be realized as well.

The transmitter terminal aboard the ISS has to comprise a source of entangled photons and two separate telescope and PAT subsystems directing the photons towards two ground stations provided both are within reach. A simultaneous link between ISS and two ground stations will only be available for a few minutes per day at most [58,137]. During this time, the acquisition sequence as well as the key distribution as outlined in Sect. 6.1 have to take place. When distributing pairs of entangled photons from a space-based source to two different ground stations, it has to be identified which of the detected photons “belong” to each other; the receivers must be synchronized with the transmitter. To set up a QKD protocol it is therefore mandatory to establish conventional communication links between all three partners in addition to the two quantum channels: Synchronization and comparison of the received key may be established via classical optical or RF links. For this purpose one could use the beacon laser implemented for pointing and acquisition and thus save on hardware [58,134]. The exchange of the encrypted data between the ground stations may be performed via classical channels, e.g. optical fiber.

The receiver terminals on ground must be able to detect single-photons and perform quantum-state measurements. They also have to be capable of tracking the ISS on its low orbit which asks for fast angular motions of the telescope (up to $1.0^\circ/\text{s}$ azimuth and up to $0.2^\circ/\text{s}$ elevation) [52]. This is not self-evident especially for ground stations with large telescopes, e.g., the OGS.

As outlined in, e.g., [134], the overall link attenuation, i.e. the entire loss for *both* space-to-ground links, must not exceed 60 dB. (This value results from a minimum signal-to-noise ratio determined by the repetition rate of the entangled-photon-source and the dark-count ratio of the detectors employed.) Thus, the attenuation for each space-to-ground link must not exceed 30 dB. Because of the low orbit of ISS, attenuation factors as low as this can be achieved, especially when considering a ground telescope not too small (see Fig. 2.10).⁷

6.5 Assessment

Quantum communication represents a fundamentally new technology. I will now make assessments of the critical aspects of this concept as seen from an engineering point-of-view.

Data rate: Ultimate security can only be guaranteed if the key is of the same length as the message to be encrypted. This means that the maximum net data rate is limited to the speed the key is generated with, which is proportional to (but less than half of) the pair production rate of the entangled photon source. Today, this value is as low as some tens of kb/s [58]. I may therefore say that security comes at the price of very stringent data-rate limitation.

Synchronization: The synchronization between transmitter and the two receivers has to be as accurate as some 10 ns [58]. This value scales with the pair production rate. A possible solution for this problem is to use the beacon laser for synchronization but one has to consider the different propagation properties of the atmosphere when the beacon laser is operated at a wavelength different from the entangled photons.

Link availability: The availability of a simultaneous link between the ISS and two ground stations is low [58, 137]. For a commercial application where the user decides when he likes to obtain a key independent to the actual position of the ISS, a network of satellites bearing entangled photon sources has to be set up. Another possibility is the implementation of MEO-based or even GEO-based transmitter terminals, where the access conditions more favorable. However, the large distances of such scenarios would ask for an increased in tolerable link attenuation.

Security: Since the key generated as described still has an error probability greater than zero (QBER, *quantum bit error rate*) due to, e.g., dark counts in the receiver, background radiation, or synchronization errors, there is a non-vanishing probability of an undisclosed eavesdropper to be present. Certain measures have to be carried out to make this probability sufficient low (e.g. *privacy amplification* [105]).

⁷The best sources of entangled photons available today are based on spontaneous parametric down conversion and operate at 810 nm [58]. At this wavelength the divergence is smaller than for 1 550 nm and therefore the link attenuation is reduced by some 6 dB (cf. 2.6).

Appendix A

Link duration between the ISS and a ground station

In the following the duration of mutual visibility between the ISS and a ground station will be derived as a function of five parameters: the satellite's inclination ϕ_i and altitude h , the ground station's latitude Ψ , the minimum elevation angle ε_{min} , and the longitudinal shift of the actual orbit Δ_{long} . The latter is the longitudinal difference between the ground station and the nadir of the ISS when in maximum elevation (ε_{max}) seen from the ground station (see Fig. A.1). Depending on the station's latitude Ψ , the angle δ depends on Δ_{long} in the following

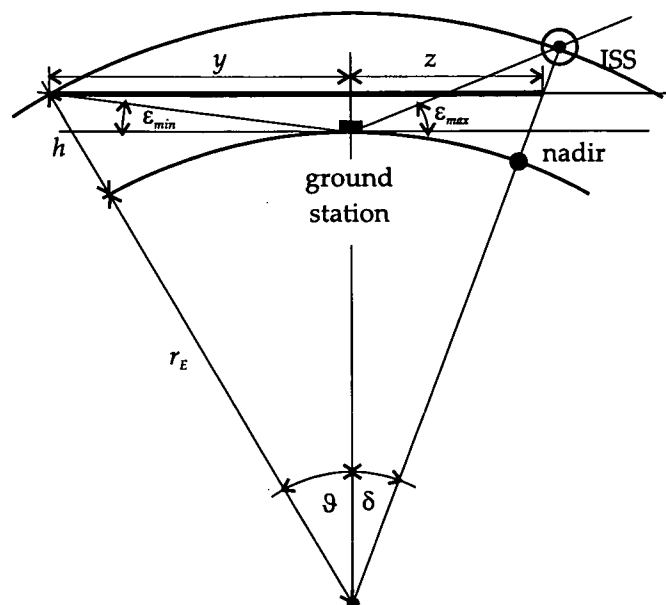


Figure A.1: ISS passing a ground station (perpendicular to the drawing-plane). The angle δ corresponds to the longitudinal shift Δ_{long} ; ε_{max} is the maximum elevation angle of the actual orbit. The minimum elevation angle ε_{min} depends on atmospheric properties or the surrounding landscape of the ground station. (r_E ... Earth radius)

way:

$$\delta = \arcsin \left(\sin \Delta_{long} \frac{\cos \Psi}{\sin \xi} \right). \quad (\text{A.1})$$

Here, ξ is the angle between the path of the nadir of the ISS and a line parallel to the equator (as shown in Fig. 2.3). It depends on the inclination angle of the ISS ($\phi_i = 51^\circ$) and the latitude of the ground station,

$$\xi = \phi_i \cos \left(\frac{\Psi \pi}{2} \right). \quad (\text{A.2})$$

To obtain the distance x as shown in Fig. A.2, I need to know the auxiliary variables y and z depending on the parameters listed above. From Fig. A.1 we see that

$$y = (r_E + h) \sin \vartheta, \quad (\text{A.3})$$

where

$$\vartheta = \arccos \left(\frac{r_E}{r_E + h} \cos \varepsilon_{min} \right) - \varepsilon_{min} \quad (\text{A.4})$$

was obtained by applying the law of sines. After a short derivation we get

$$z = \sqrt{(r_E + h)^2 - y^2} \tan \delta = (r_E + h) \cos \vartheta \tan \delta. \quad (\text{A.5})$$

This leads to

$$x = \sqrt{y^2 - z^2} = (r_E + h) \sqrt{1 - \frac{\cos^2 \vartheta}{\cos^2 \delta}}. \quad (\text{A.6})$$

Together with the angular velocity of the ISS, $\omega_s = 2\pi/T_{rev} = 1,1 \text{ mrad/s}$ (the duration of one revolution, T_{rev} , is about 92 minutes), we now can calculate the possible link duration

$$T = \frac{2}{\omega_s} \arcsin \left(\frac{x}{r_E + h} \right) = \frac{T_{rev}}{\pi} \arcsin \left(\sqrt{1 - \frac{\cos^2 \vartheta}{\cos^2 \delta}} \right). \quad (\text{A.7})$$

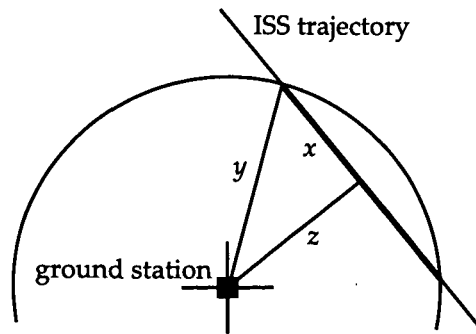


Figure A.2: Simplified version of Fig. 2.3 to illustrate the calculation of the possible link duration. The lengths y and z have been shown in Fig. A.1.

Appendix B

Abbreviations, constants, and symbols

B.1 List of abbreviations

ASE	amplified spontaneous emission
APD	avalanche photo diode
ARTEMIS	advanced relay and technology mission satellite
BERT	bit error ratio tester
BF	Bessel filter
CCD	charge coupled devices
DD	direct detection
DFB	distributed feed-back
DPSK	differential phase shift keying
DRTS	data relay test satellite
EAM	electro-absorption modulator
EDFA	Erbium-doped fiber amplifier
EPR	Einstein, Podolsky, and Rosen
ESTEC	European Space Research & Technology Center
ESA	European Space Agency
FBG	fiber Bragg grating
FOV	field of view
FPF	Fabry-Pérot filter
FSK	frequency shift keying
GEO	geostationary orbit
ISI	intersymbol interference
ISL	intersatellite link
ISS	International Space Station
ISSERT	International Space Station engineering research and technology development program
ITU	International Telecommunication Union
JEM	Japanese experimental module
JPL	Jet Propulsion Laboratory
LCDE	laser communications demonstration experiment
LCE	laser communications equipment
LEO	low Earth orbit
LF	low-pass filter
LO	local oscillator

LUCE	laser utilizing communications equipment
MEO	medium earth orbit
MZM	Mach-Zehnder modulator
NASA	National Aeronautics and Space Administration
NRZ	non return-to-zero
OCD	optical communication demonstrator
OCDHRLF	optical communication demonstration and high-rate link facility
OGS	ESA's optical ground station at Tenerife
OICETS	optical inter-orbit communications engineering test satellite
OOK	on-off-keying
PAA	point ahead angle
PAT	pointing, acquisition, and tracking
PDBS	polarization dependent beam splitter
PDF	probability density function
PRBS	pseudo random bit sequence
PSK	phase shift keying
QBER	quantum bit error rate
QKD	quantum key distribution
QPD	quadrant photo diode
PN	pseudo noise
PRBS	pseudo random bit sequence
RF	radio frequency
RZ	return-to-zero
SILEX	semiconductor intersatellite link experiment
SLSR	side lobe suppression ratio
SM	single-mode
SNR	signal-to-noise ratio
SOLACOS	solid state laser communications in space
SOP	state of polarization
SROIL	short range intersatellite link
STRV	space technology research vehicle
TDRSS	tracking and data relay satellite system
TSX	tri-service experiments
TUV	University of Technology, Vienna
WDM	wavelength-division-multiplex

B.2 List of physical and mathematical constants

$c = 2.9979 \cdot 10^8$ m/s	free space light velocity
$q = 1.602 \cdot 10^{-19}$ As	elementary charge
$e = 2.7183$	Euler's constant
$h = 6.6262 \cdot 10^{-34}$ Js	Planck's constant
$j = \sqrt{-1}$	imaginary unit
$k = 1.3807 \cdot 10^{-23}$ J/K	Boltzmann's constant

B.3 List of astronomical data

$I_0 = 3.1 \cdot 10^{-9} \text{ W/m}^2$	reference visible irradiance
$AU = 149.597 \cdot 10^6 \text{ km}$	astronomical unit (distance Earth ↔ Sun)
$r_E = 6\,377 \text{ km}$	radius of the Earth
$r_{Sun} = 696 \cdot 10^3 \text{ km}$	radius of the Sun
$r_{Moon} = 1\,734 \text{ km}$	radius of the Moon
$r_{Venus} = 6\,052 \text{ km}$	radius of the Venus
$d_{Moon} = 0.00257 \text{ AU} = 384\,400 \text{ km}$	average distance Earth ↔ Moon
$d_{Venus} = 0.277 \text{ AU}$	average distance Earth ↔ Venus
$T_{Sun} = 5\,900 \text{ K}$	temperature of the Sun
$T_{Sirius} = 11\,000 \text{ K}$	temperature of the Sirius

B.4 List of Latin symbols

a	altitude of a ground station above sea level
a_k	original binary value of k-th bit
\mathcal{A}	albedo of celestial body
A	attenuation factor
A_{eff}	body's area as seen from the receiver
A_{rec}	receiver's area
A_{FP}	beam area at receiver
b_k	detected binary value of k-th bit
$b(t)$	optical filter's complex baseband impulse response
$B(f)$	optical filter's baseband field transfer function
B_e	3 dB-bandwidth of the electrical filter
$B_{e,n}$	power equivalent width of the electrical filter
B_o	3 dB-bandwidth of the optical filter
$B_{o,n}$	power equivalent width of the optical filter
BEP	bit error probability
C	conversion gain of photo diode module
C_n^2	structure constant
$C_{n,0}^2$	structure constant on ground
d	duty cycle
D_R	diameter of receive telescope
D_S	diameter of radiation source
D_T	diameter of transmit telescope
$e_{in}(t)$	communication signal at the receiver input
$e_f(t)$	optically amplified and filtered field
E_1	optical energy for a "1"-bit
f	frequency
F_{equ}	equivalent noise figure
F_b	noise figure of the booster amplifier at the transmitter
F_p	noise figure of the optical preamplifier
FWHH	full width half height (expressed as wavelength) of optical filter
$g(t)$	optical field at receiver input
G_b	gain of the optical booster amplifier at the transmitter

G_p	gain of the optical preamplifier
h	altitude of a satellite, height above ground
$h(t)$	impulse response of photo diode module
$H(f)$	transfer function of photo diode module
\mathcal{H}	spectral irradiance
I_d	laser drive current
IL	insertion loss of optical filter
k_1	gain reduction factor
l	length of fiber Bragg grating
L	distance between ground station and satellite
L_p	pointing loss
m	number of spatial modes
M_{pol}	number of polarization modes
n_s	receiver sensitivity (given in photons per bit)
n_q	quantum limit
$n_{ASE,b}$	amplified spontaneous emission from the transmitter's booster amplifier
$n_{ASE,p}$	amplified spontaneous emission from the preamplifier
n_{back}	background noise
$n(\mathcal{R})$	refractive index
n_0	constant tributary of refractive index
$n_1(\mathcal{R})$	tributary of refractive index dependent on location
N	length of pseudo random bit sequence
NEP	noise equivalent power
N_0	overall noise power spectral density
$N_{ASE,b}$	booster amplified spontaneous emission power spectral density
$N_{ASE,p}$	preamplifier amplified spontaneous emission power spectral density
N_{back}	background radiation power spectral density
NEP	noise equivalent power of diode module
$N(\lambda)$	spectral radiance
$p(t)$	optical input power
$p_1(t)$	optical power waveform representing a single "1"-bit
$p_x(\xi)$	probability density function of stochastic process x
$P_{n,back}$	average of the optically filtered background radiation
$P_{n,ASE}$	overall incoherent noise average
$P_{n,ASE,b}$	average of the optically filtered transmitter booster's ASE
$P_{n,ASE,p}$	average of the optically filtered preamplifier's ASE
P_T	mean power at transmitter output
P_R	mean power at receiver input
$q(t)$	optical communication signal at transmitter output
r_0	Fried parameter
$r_b(t)$	optical filter's autocorrelation function
$r_h(t)$	electrical filter's autocorrelation function
R	data rate, distance between receiver and source of background radiation
R_T	resistance converting the current-output of a photo diode into a voltage
\mathcal{R}	point in three dimensional space
s	normalized frequency
$s(t)$	mean of the electrical signal after the diode module

S	responsivity of a photo diode, (spatial) power density
S_{th}	decision threshold
$SLSR$	side lobe suppression ratio
t	time
T	link duration, temperature
T_A	atmospheric transmissivity
T_{bit}	bit duration
T_{eff}	effective temperature of celestial object
T_p	effective pulse duration
T_{rev}	duration of one revolution of a satellite
T_s	sampling instant
T_{se}	effective surface temperature for self emission
T_T	transmission factor of transmit telescope
T_R	transmission factor of receive telescope
U_b	offset voltage of modulation signal
U_m	peak-to-peak voltage of modulation signal
v	relative velocity between two terminals
v_g	velocity component of the ground station, group velocity
v_{pw}	pseudo wind speed for the H-V model
v_s	velocity component of the satellite
x	auxiliary variable to calculate link duration
y	auxiliary variable to calculate link duration
z	auxiliary variable to calculate link duration

B.5 List of Greek symbols

α	auxiliary angle, affordable pointing error, roll-off factor of pulses
$\beta(f)$	design parameter for fiber Bragg gratings
δ	angle corresponding to Δ longitude
Δ longitude	longitudinal shift of actual orbit
ΔT	time it takes the light to travel from Terminal 1 to Terminal 2
ϵ	elevation angle (measured from equator)
γ	auxiliary angle
γ_q	sensitivity penalty relative to the quantum limit
λ	optical wavelength
ϕ_i	inclination of satellite's orbit
κ	coupling coefficient of fiber Bragg grating
Ψ	geographic latitude
θ_{atm}	divergence angle resulting from the atmosphere
θ_{DL}	planar diffraction limited field-of-view
θ_{FOV}	planar angle of the receiver field-of-view
θ_G	Gaussian beam divergence angle
θ_T	divergence angle resulting from the transmit telescope
ϑ	auxiliary angle to calculate link duration
$\sigma_s^2(t)$	variance of electrical signal at input of decision gate
$\sigma_{shot,s}^2(t)$	variance according to signal-shot noise
$\sigma_{shot,ASE}^2(t)$	variance according to ASE-shot noise

$\sigma_{s-ASE}^2(t)$	variance according to signal-ASE noise
$\sigma_{ASE-ASE}^2(t)$	variance according to ASE-ASE noise
$\sigma_{elec}^2(t)$	variance according to electronic noise
ζ	extinction ratio
ξ	angle between the path of the nadir of the ISS and a line parallel to the equator
ω_E	angular velocity of point on surface of the Earth
ω_s	angular velocity of satellite
ω_0	beam radius
Ω_{DL}	diffraction limited receiver field-of-view
Ω_{FOV}	receiver field-of-view
Ω_R	solid angle subtended by the receiver at the source
Ω_S	solid angle subtended by the source at the receiver

Bibliography

- [1] W. Carey, D. Isakeit, M. Heppener, K. Knott, and J. Feustel-Büechl, "The International Space Station European users guide," European Space Agency, ISS User Information Centre (MSM-GAU), ESTEC, Tech. Rep., 2001.
- [2] NASA. (2003, May) Space network online information center. [Online]. Available: <http://nmsp.gsfc.nasa.gov/tdrss/tdrsshome.html>
- [3] A. Dickinson, G. Oppenhäuser, J. Sandberg, K. R. Derbyshire, A. G. Bird, L. Balestra, P. Flament, and F. Falbe-Hansen, "The Artemis programme," *esa bulletin*, vol. 91, pp. 32–39, 1997.
- [4] NASDA. (2003, May) "KODAMA" Data Relay Test Satellite. [Online]. Available: <http://www.nasda.go.jp/projects/sat/drts/>
- [5] Y. Arimoto, "Possibility of high-speed optical feeder-link and its demonstration experiment," in *Proc. LEOS, IEEE Laser and Electro-Optics Society 12th Annual Meeting*, vol. 1, November 1999, pp. 45–46.
- [6] J. Uchida and Y. Arimoto, "Feasibility study on the tracking of geodesic satellites in laser communications demonstration experiment," in *Proc. SPIE, Free-Space Laser Communication Technologies XIII*, vol. 4272, January 2001, pp. 28–37.
- [7] G. G. Ortiz, M. Jeganathan, J. V. Sandusky, and H. Hemmati, "Design of a 2.5 Gbps optical transmitter for the international space station," in *Proc. SPIE, Free-Space Laser Communication Technologies XI*, vol. 3615, January 1999, pp. 179–184.
- [8] S. G. Lambert and W. L. Casey, *Laser Communications in Space*. Artech House, 1995.
- [9] M. Katzmann, *Laser satellite communications*. Prentice-Hall, 1987.
- [10] V. W. S. Chan, "Intersatellite optical heterodyne communication systems," *The Lincoln Laboratory Journal*, vol. 1, no. 2, pp. 169–186, 1988.
- [11] W. R. Leeb, "Coherent optical space communications," *Lecture Notes in Control and Information Sciences*, 1992.
- [12] V. W. S. Chan, "Optical space communications," *J. Select. Topics Quantum Electron.*, vol. 6, no. 6, pp. 959–975, 2000.
- [13] H. P. Lutz, "Optical communications in space – twenty years of ESA effort," *esa bulletin*, vol. 91, pp. 25–31, 1997.

- [14] T. T. Nielsen, "Pointing, acquisition and tracking system for the free space laser communication system SILEX," in *Proc. SPIE, Free-Space Laser Communication Technologies VII*, vol. 2381, January 1995, pp. 194–205.
- [15] G. Planche, B. Laurent, J. Guillen, V. Chorvalli, and E. Desplats, "SILEX final ground testing and in-flight performances assessment," in *Proc. SPIE, Free-Space Laser Communication Technologies XI*, vol. 3615, January 1999, pp. 64–77.
- [16] A. Yamamoto, T. Hori, T. Shimizu, and K. Nakagawa, "Japanese first optical inter-orbit communications engineering test satellite (OICETS)," in *Proc. SPIE, Space Optics 1994: Space Instrumentation and Spacecraft Optics*, vol. 2210, April 1994, pp. 30–38.
- [17] M. Wittig, "Optical space communications: How to realize the second generation of small optical terminals," *Space Communications*, vol. 12, pp. 55–89, 1994.
- [18] R. N. Wilson, *Reflecting Telescope Optics I*. Springer, 1996.
- [19] E. Korevaar, R. J. Hofmeister, J. Schuster, C. Chow-Miller, P. Adhikari, H. Hakakha, D. Cuthbert, and R. Ruigrok, "Design of satellite terminal for BMDO lasercom technology demonstration," in *Proc. SPIE, Free-Space Laser Communication Technologies VII*, vol. 2381, January 1995, pp. 60–71.
- [20] E. Korevaar, J. Schuster, H. Hakakha, R. Stieger, P. Adhikari, B. Riley, C. Moursund, J. Koontz, A. Lath, and M. Barclay, "Design of ground terminal for STRV-2 satellite-to-ground lasercom experiment," in *Proc. SPIE, Free-Space Laser Communication Technologies IX*, vol. 3266, January 1997, pp. 153–164.
- [21] I. I. Kim, B. Riley, N. M. Wong, M. Mitchell, W. Brown, H. Hakakha, P. Adhikari, and E. J. Korevaar, "Lessons learnt from the STRV-2 satellite-to-ground lasercom experiment," in *Proc. SPIE, Free-Space Laser Communication Technologies XIII*, vol. 4272, January 2001, pp. 1–15.
- [22] T. Wiesmann and H. Zech, "Optical space communications systems," in *Proc. 26th European conference on optical communications, ECOC*, September 2000, pp. 25–28.
- [23] B. Hespeler, K. Schmid, and M. Schnurr, "Inter satellite link – tracking front end "ISL-TFE"," Bosch SatCom GmbH," European Space Agency Contract Report, ESA, Contract No. 13321/98/NL/US, Final Report, 2000.
- [24] L. Bartelt-Berger, F. Heine, U. Hidebrand, D. Lange, T. Schwager, S. Seel, and B. Smutny, "1 W laser transmitter for intersatellite links," in *Proc. 26th European conference on optical communications, ECOC*, September 2000, pp. 29–30.
- [25] K. Pribil, K. Kudielka, K. Ruzicka, and P. Serbe, "A coherent analog communication system for optical intersatellite-links," in *AIAA '01, 19th AIAA International Communications Satellite Systems Conference*, vol. Session 39, 512, April 2001, pp. 1–6.
- [26] C. Chen and J. Lesh, "Overview of the optical communications demonstrator," in *Proc. SPIE, Free-Space Laser Communication Technologies VI*, vol. 2123, January 1994, pp. 85–95.

- [27] J. V. Sandusky, M. Jeganathan, G. G. Ortiz, A. Biswas, S. Lee, G. Parker, B. Liu, D. Johnson, J. DePew, and J. R. Lesh, "Overview of the preliminary design of the optical communication demonstration and high-rate link facility," in *Proc. SPIE, Free-Space Laser Communication Technologies XI*, vol. 3615, January 1999, pp. 185–191.
- [28] K. Pribil and J. Fleming, "SOLACOS high datarate satellite communication system verification program," in *Proc. SPIE, Space Optics 1994: Space Instrumentation and Spacecraft Optics*, vol. 2210, April 1994, pp. 38–48.
- [29] M. Pfennigbauer, W. R. Leeb, P. J. Winzer, and O. Wallner, "Fiber amplified free space laser communications ("FALCO")," Institut für Nachrichtentechnik und Hochfrequenztechnik, TU Wien, "European Space Agency Contract Report, ESTEC, Contract No. 14459/00/NL/JSC, Data Package, 2001.
- [30] R. W. Kaliski, S. M. Genco, D. Thompson, B. Breshears, T. O'Conner, K. M. Miller, E. W. Taylor, A. D. Sanchez, J. E. Winter, and R. Ewart, "Laser communication intersatellite links realized with commercial off-the-shelf technology," in *Proc. SPIE, Free-Space Laser Communication Technologies XI*, vol. 3615, January 1999, pp. 170–178.
- [31] G. Einarsson, *Principles of lightwave communications*. John Wiley & Sons, Inc., 1996.
- [32] P. J. Winzer, "Optical transmitters, receivers, and noise," *Wiley Encyclopedia of Telecommunications*, J.G.Proakis (ed.), pp. 1824–1840, 2002.
- [33] B. E. A. Saleh and M. C. Teich, *Fundamentals of Photonics*. John Wiley & Sons, Inc., 1991.
- [34] M. A. Itzler *et al.*, "High-performance, manufacturable avalanche photodiodes for 10 Gb/s optical receivers," in *Proc. OFC, Optical Fiber Communication*, vol. FG5, March 2000, pp. 126–128.
- [35] O. Wallner, P. J. Winzer, and W. R. Leeb, "Alignment tolerances for plane-wave to single-mode fiber coupling and their mitigation by use of pigtailed collimators," *Applied Optics*, vol. 42, 2002.
- [36] H. Hemmati, "Status of free-space optical communications program at JPL," in *Proc. SPIE, Free-Space Laser Communication Technologies XI*, vol. 3615, January 1999, pp. 101–105.
- [37] E. Desurvire, *Erbium-doped fiber amplifiers*. John Wiley & Sons, Inc., 1994.
- [38] H. A. Haus, Ed., *Electromagnetic noise and quantum optical measurements*. Berlin: Springer-Verlag, 2000.
- [39] M. M. Strasser, M. Pfennigbauer, M. Pauer, and P. J. Winzer, "Experimental verification of optimum filter bandwidth in direct-detection (N)RZ receivers limited by optical noise," in *LEOS '01, IEEE Laser and Electro-Optics Society 14th Annual Meeting*, vol. 2, November 2001, pp. 485–486.
- [40] G. Jacobsen, *Noise in digital optical transmission systems*. Artech House, 1994.
- [41] L. Kazovsky, S. Benedetto, and A. Willner, *Optical fiber communication systems*. Artech House, Inc., 1996.

- [42] O. K. Tonguz and R. E. Wagner, "Equivalence between preamplified direct detection and heterodyne receivers," *IEEE Photon. Technol. Lett.*, vol. 3, pp. 835–837, 1991.
- [43] J. R. Barry and E. A. Lee, "Performance of coherent optical receivers," *Proceedings of the IEEE*, vol. 78, no. 8, pp. 1369–1394, 1990.
- [44] S. Norimatsu *et al.*, "10 Gbit/s optical BPSK homodyne detection experiment with solitary DFB laser diodes," *El. Lett.*, vol. 31, no. 2, pp. 125–127, 1995.
- [45] W. Atia and R. S. Bondurant, "Demonstration of return-to-zero signaling in both OOK and DPSK formats to improve receiver sensitivity in an optically preamplified receiver," in *Proc. LEOS, IEEE Laser and Electro-Optics Society 12th Annual Meeting*, vol. 1, 1999, pp. 226–227.
- [46] J. McElroy, N. McAvoy, E. H. Johnson, J. J. Degnan, F. E. Goodwin, D. M. Henderson, T. A. Nussmaier, L. S. Stokes, B. J. Peyton, and T. Flattau, "CO₂ laser communication systems for near-earth space applications," *Proc. of the IEEE*, vol. 65, no. 2, pp. 221–251, 1977.
- [47] M. Ross, P. Freedman, J. Abernathy, G. Matassov, J. Wolf, and J. D. Barry, "Space optical communication with the Nd:YAG laser," *Proc. of the IEEE*, vol. 66, p. 319, 1978.
- [48] E. Messerschmid and R. Bertrand, *Space Stations*. Berlin Heidelberg: Springer, 1999.
- [49] K. A. Winick, "Atmospheric turbulence-induced signal fades on optical heterodyne communication links," *Applied Optics*, vol. 25, no. 11, pp. 1817–1825, 1986.
- [50] L. C. Andrews and R. L. Phillips, *Laser Beam Propagation Through Random Media*. SPIE - The International Society for Optical Engineering, 1998.
- [51] G. Gilbert and M. Hamrick, "Practical quantum cryptography: A comprehensive analysis (part one)," MITRE, Technical Report, 2000.
- [52] T. Weigel, K. Kudielka, B. Thieme, H. Mannstein, R. Meyer, C. Werner, V. Banakh, W. Holota, and S. Manhart, "Optical ground station," Contraves Space, DLR, ASTRIUM, ESTEC, Contract No. 14231/00NL/WK, Final Report, 2001.
- [53] W. K. Pratt, *Laser Communication Systems*, 1st ed. New York: John Wiley & Sons, Inc., 1969.
- [54] D. L. Fried, "Optical resolution through a randomly inhomogeneous medium for very long and very short exposures," *Journal of the Optical Society of America*, vol. 56, pp. 1372–1379, 1966.
- [55] D. L. Fried, "Statistics of a geometric representation of wavefront distortion," *Journal of the Optical Society of America*, vol. 55, pp. 1427–1435, 1965.
- [56] M. Pfennigbauer and W. R. Leeb, "Optical telescopes for intersatellite link - feasibility study," Institut für Nachrichtentechnik und Hochfrequenztechnik, TU Wien, ESTEC, Contract No. 15872/01 (Subcontract No. ML/15872/sub2 with Media Lario S.r.l.), 2002.

- [57] Z. Sodnik, J. A. Perdignes, and R. H. Czinchy, "Design data summary of the ESA optical ground station for in-orbit check-out of laser communication payloads and for the observation and registration of space debris," ESA/ESTEC, European Space Agency Report, ESA, Ref. No. XA95/267/ZS, 2000.
- [58] M. Aspelmeyer, H. R. Böhm, C. Brukner, R. Kaltenbaek, M. Lindenthal, J. Petschinka, T. Jennewein, R. Ursin, P. Walther, A. Zeilinger, M. Pfennigbauer, and W. R. Leeb, "Quantum Communications in Space (QSpace): Final Report," Institut für Nachrichtentechnik und Hochfrequenztechnik, TU Wien, Institut für Experimentalphysik, Universität Wien, European Space Agency Contract Report, ESTEC, Contract No. 16358/02/NL/SFe, 2003.
- [59] R. P. Feynman, R. B. Leighton, and M. Sands, *Lectures on Physics – Volume I*. Addison-Wesley Publishing Company, 1963.
- [60] H. Kogelnik and T. Li, "Laser beams and resonators," *Proceedings of the IEEE*, vol. 54, no. 10, pp. 1312–1329, 1966.
- [61] W. R. Leeb, "Degradation of signal to noise ratio in optical free space data links due to background illumination," *Applied Optics*, vol. 28, pp. 3443–3449, 1989.
- [62] R. C. Ramsey, "Spectral irradiance from stars and planets, above the atmosphere, from 0.1 to 100.0 microns," *Applied Optics*, vol. 1, no. 4, pp. 465–471, 1962.
- [63] H.-H. Voigt, *Abriß der Astronomie*. Spektrum Akademischer Verlag, 1991.
- [64] M. V. Zombeck, *Handbook of Astronomy and Astrophysics*, 2nd ed. Cambridge: Cambridge University Press, 1990.
- [65] Heavens Above. (2003, July). [Online]. Available: <http://www.heavens-above.com>
- [66] W. L. Wolfe and G. J. Zissis, *The infrared handbook*. Michigan, 1978.
- [67] J. M. Perdignes (ESTEC/ESA), May 2003, personal communication.
- [68] D. L. Begley, "Laser cross-link systems and technology," *IEEE Comm. Mag.*, pp. 126–132, 2000.
- [69] W. R. Leeb, "Laser space communications: systems, technologies, and applications," *The Review of Laser Engineering*, vol. 28, pp. 804–808, 2000.
- [70] M. Reyes, J. A. Rdorigez, T. Viera, H. Moreno, J. L. Rasilla, F. Gago, L. F. Rodrigez, P. Gomez, and E. Ballesteros, "Design and performance of the ESA optical ground station," in *Proc. SPIE, Free-Space Laser Communication Technologies XIV*, vol. 4635, January 2002, pp. 248–261.
- [71] J. W. Alexander, S. Lee, and C. Chen, "Pointing and tracking concepts for deep space missions," in *Proc. SPIE, Free-Space Laser Communication Technologies XI*, vol. 3615, January 1999, pp. 230–248.
- [72] M. Pfennigbauer and W. R. Leeb, "Optical telescopes for intersatellite link - feasibility study," Institut für Nachrichtentechnik und Hochfrequenztechnik, TU Wien, ESTEC, Contract No. 15872/01 (Subcontract No. ML/15872/sub2 with Media Lario S.r.l.), Trade-Off and Goals for Laser Communication Terminal Systems, 2002.

- [73] M. Sabbatini *et al.*, "ISS Users Guide for Earth Observation," MSM-EO Working Group, Tech. Rep., 2001.
- [74] E. Wolf, *Progress in Optics*. Amsterdam, New York, Oxford: North Holland Publishing Company, 1981.
- [75] F. Roddier, *Adaptive Optics in Astronomy*. Cambridge: Cambridge University Press, 1999.
- [76] CRL. (2002, September). [Online]. Available: <http://www2.crl.go.jp/mt/b162/index-e.html>
- [77] M. M. Strasser, "Optical free-space transmitters and their effects on preamplified direct detection," PhD Thesis, Institut für Nachrichtentechnik und Hochfrequenztechnik, TU Wien, 2002.
- [78] M. Pauer, "Return-to-zero coding in optical intersatellite links," PhD Thesis, Institut für Nachrichtentechnik und Hochfrequenztechnik, TU Wien, 2003.
- [79] N. A. Olsson, "Lightwave systems with optical amplifiers," *J. Lightwave Technol.*, vol. 7, pp. 1071–1082, 1989.
- [80] A. Othonos and K. Kalli, *Fiber Bragg Gratings: Fundamentals and Applications in Telecommunications and Sensing*. Boston, London: Artec House, 1999.
- [81] R. Kashyap, *Fiber Bragg Gratings*. Academic Press, 1999.
- [82] S. Lee, J. W. Alexander, and M. Jeganathan, in *Proc. SPIE, Free-Space Laser Communication Technologies XII*, vol. 3932, January 2000.
- [83] M. Pfennigbauer, "Simulation von Empfängern für optisch vorverstärkte Return-to-Zero Signale," Diploma Thesis, Institut für Nachrichtentechnik und Hochfrequenztechnik, TU Wien, 2000.
- [84] D. E. Johnson, *A Handbook of Active Filters*. Prentice Hall, 1980.
- [85] E. A. Lee and D. G. Messerschmitt, *Digital Communication*, 2nd ed. Kluwer Academic Publishers, 1994.
- [86] M. Pfennigbauer, P. J. Winzer, M. M. Strasser, and W. R. Leeb, "Optimum optical and electrical filter characteristics in optically preamplified direct detection (N)RZ receivers," in *Proc. SPIE, Free-Space Laser Communication Technologies XIII*, vol. 4272, January 2001, pp. 160–169.
- [87] P. J. Winzer, A. Kalmar, and W. R. Leeb, "Role of amplified spontaneous emission in optical free-space communication links with optical amplification – impact on isolation and data transmission; utilization for pointing, acquisition, and tracking," in *Proc. SPIE, Free-Space Laser Communication Technologies XI*, vol. 3615, January 1999.
- [88] M. Pfennigbauer, M. Pauer, P. J. Winzer, and M. M. Strasser, "Performance optimization of optically preamplified receivers for return-to-zero and non return-to-zero coding," *Int. J. Electron. Commun.*, vol. 56, no. 4, pp. 261–267, 2002.

- [89] L. Boivin and G. J. Pendock, "Receiver sensitivity for optically amplified RZ signals with arbitrary duty cycle," in *Proc. OAA, Optical amplifiers and their applications*, 1999.
- [90] P. J. Winzer and A. Kalmar, "Sensitivity enhancement of optical receivers by impulsive coding," *J. Lightwave Technol.*, vol. 17, no. 2, pp. 171–177, 1999.
- [91] M. Pauer, P. J. Winzer, and W. R. Leeb, "Bit error probability reduction in direct detection optical receivers using RZ coding," *J. Lightwave Technology*, vol. 19, no. 9, pp. 1255–1262, 2001.
- [92] D. Marcuse, "Derivation of analytical expressions for the bit-error probability in lightwave systems with optical amplifiers," *J. Lightwave Technol.*, vol. 8, no. 12, pp. 1816–1823, 1990.
- [93] P. J. Winzer, "Receiver noise modeling in the presence of optical amplification," in *Proc. OAA, Optical amplifiers and their applications*, July 2001.
- [94] I. T. Monroy and G. Einarsson, "Bit error evaluation of optically preamplified direct detection receivers with Fabry-Perot optical filters," *J. Lightwave Technol.*, vol. 15, no. 8, pp. 1546–1553, 1997.
- [95] D. Marcuse, "Calculation of bit-error probability for a lightwave systems with optical amplifiers and post-detection gaussian noise," *J. Lightwave Technol.*, vol. 9, no. 4, pp. 505–513, 1991.
- [96] P. J. Winzer, "Performance estimation of receivers corrupted by optical noise," *OSA Trends in Optics and Photonics (TOPS)*, N. Jolley, J. D. Minelly, and Y. Nakano, eds., vol. 60, pp. 268–273, 2001.
- [97] M. R. N. Ribeiro, H. Waldmann, J. Klein, and L. de Souza Mendes, "Error-rate patterns for the modeling of optically amplified transmission systems," *IEEE Journal on Selected Areas in Communications*, vol. 15, no. 4, pp. 707–715, 1997.
- [98] P. J. Winzer, M. Pfennigbauer, M. M. Strasser, and W. R. Leeb, "Optimum filter bandwidths for optically preamplified NRZ and RZ receivers," *J. Lightwave Technology*, vol. 19, no. 9, pp. 1263–1273, 2001.
- [99] M. Pfennigbauer, M. M. Strasser, M. Pauer, and P. J. Winzer, "Dependence of optically preamplified receiver sensitivity on optical and electrical filter bandwidths – measurement and simulation," *Phot. Technol. Lett.*, vol. 14, no. 6, pp. 831–833, 2002.
- [100] D. Ben-Eli, Y. E. Dallal, and S. S. Shitz, "Performance bounds and cutoff rates of quantum limited OOK with optical amplification," *IEEE J. Select. Areas Commun.*, vol. 13, no. 3, pp. 510–530, 1995.
- [101] S. R. Chinn, "Error-rate performance of optical amplifiers with fabry-perot filters," *El. Lett.*, vol. 31, pp. 756–757, 1995.
- [102] P. J. Winzer, A. Kalmar, and W. R. Leeb, "Intersatellite laser communications at 1.5 μm : Chances and problems," Institut für Nachrichtentechnik und Hochfrequenztechnik, TU Wien, "European Space Agency Contract Report, Contract No. 11846/96/NL/SB(SC), 1998.

- [103] M. Pfennigbauer and W. R. Leeb, "Optical satellite communication with erbium doped fiber amplifiers," *Space Communications*, vol. 19, no. 1, pp. 59–67, 2003.
- [104] G. Alber, T. Beth, M. H. and P. Horodecki, R. Horodecki, M. Rötteler, H. Weinfurter, R. Werner, and A. Zeilinger, Eds., *Quantum Information: An Introduction to Basic Theoretical Concepts and Experiments*. Berlin: Springer-Verlag, 2001.
- [105] D. Bouwmeester, A. Ekert, and A. Zeilinger, Eds., *The Physics of Quantum Information*. Berlin: Springer-Verlag, 2000.
- [106] N. Gisin, G. Ribordy, W. Tittel, and H. Zbinden, "Quantum cryptography," *Rev. Mod. Phys.*, vol. 74, pp. 145–195, 2002.
- [107] G. S. Vernam, "Cipher printing telegraph systems for secret wire and radio telegraphic communications," *J. Amer. Inst. Elec. Eng.*, vol. 45, pp. 109–115, 1926.
- [108] C. E. Shannon, "Communication theory of secrecy systems," *Bell System Technical Journal*, vol. 28, pp. 656–715, 1949.
- [109] C. H. Bennett and G. Brassard, "Quantum cryptography: Public key distribution and coin tossing," in *Proceedings of IEEE International Conference on Computers, Systems, and Signal Processing, Bangalore, India*. New York: IEEE, 1984, pp. 175–179.
- [110] E. Schrödinger, "Die gegenwärtige Situation in der Quantenmechanik," *Naturwissenschaften*, vol. 23, pp. 807–812; 823–828; 844–849, 1935.
- [111] A. Einstein, B. Podolsky, and N. Rosen, "Can quantum-mechanical description of physical reality be considered complete?" *Physical Review*, vol. 47, pp. 777–780, 1935.
- [112] J. S. Bell, "On the problem of hidden variables in quantum mechanics," *Rev. Mod. Phys.*, vol. 38, pp. 447–452, 1966.
- [113] J. F. Clauser and A. Shimony, "Bell's theorem: experimental tests and implications," *Rep. Prog. Phys.*, vol. 41, p. 1881, 1978.
- [114] A. Aspect, J. Dalibard, and G. Roger, "Experimental test of bell's inequalities using time-varying analyzers," *Physical Review Letters*, vol. 49, no. 25, pp. 1804–1807, 1982.
- [115] G. Weihs, T. Jennewein, C. Simon, H. Weinfurter, and A. Zeilinger, "Violation of Bell's inequality under strict Einstein locality conditions," *Phys. Rev. Lett.*, vol. 81, pp. 5039–5043, 1998.
- [116] T. Jennewein, C. Simon, G. Weihs, H. Weinfurter, and A. Zeilinger, "Quantum cryptography with entangled photons," *Phys. Rev. Lett.*, vol. 84, no. 20, pp. 4729–4732, 2000.
- [117] C. H. Bennett, F. Bessette, G. Brassard, L. Salvail, and J. Smolin, "Experimental quantum cryptography," *Journal of Cryptology*, vol. 5, pp. 3–28, 1992.
- [118] E. Waks, A. Zeevi, and Y. Yamamoto, "Security of quantum key distribution with entangled photons against individual attacks," *Phys. Rev. A*, vol. 65, p. 52310, 2002.
- [119] MagiQ. (2004, February). [Online]. Available: <http://www.maqiqtech.com/>
- [120] idQantique. (2004, February). [Online]. Available: <http://www.idqantique.com/>

- [121] W. Tittel, J. Brendel, H. Zbinden, and N. Gisin, "Violation of bell inequalities by photons more than 10 km apart," *Phys. Rev. Lett.*, vol. 81, pp. 3563–3566, 1998.
- [122] W. T. Buttler, R. J. Hughes, S. K. Lamoreaux, G. L. Morgan, J. E. Nordholt, and C. G. Peterson, "Daylight quantum key distribution over 1.6 km," *Phys. Rev. Lett.*, vol. 84, no. 24, pp. 5652–5655, 2000.
- [123] J. G. Rarity, P. M. Gorman, and P. R. Tapster, "Secure key exchange over 1.9 km free-space range using quantum cryptography," *Electronics Letters*, vol. 37, no. 8.
- [124] D. Stucki, N. Gisin, O. Guinnard, G. Ribordy, and H. Zbinden, "Quantum key distribution over 67 km with a plug&play system," *New Journal of Physics*, vol. 4, pp. 41.1–41.8, 2002.
- [125] R. J. Hughes, J. E. Nordholt, D. Derkacs, and C. G. Peterson, "Practical free-space quantum key distribution over 10 km in daylight and at night," *New Journal of Physics*, vol. 4, pp. 43.1–43.14, 2002.
- [126] A. Beveratos, R. Brouri, T. Gacoin, A. Villing, J.-P. Poizat, and P. Grangier, "Single photon quantum cryptography," *Phys. Rev. Lett.*, vol. 89, pp. 187 901–1 – 4, 2002.
- [127] C. Kurtsiefer, P. Zarda, M. Halder, H. Weinfurter, P. M. Gorman, P. R. Tapster, and J. G. Rarity, "A step towards global key distribution," *Nature*, vol. 419, p. 450, 2002.
- [128] H. Kosaka, A. Tomita, Y. Nambu, T. Kimura, and K. Nakamura, "Single-photon interference experiment over 100 km for quantum cryptography system using a balanced gated-mode photon detector," *Electronics Letters*, vol. 39, no. 16, pp. 1199–1201, 2003.
- [129] W. T. Buttler, R. J. Hughes, P. G. Kwiat, S. K. Lamoreaux, G. G. Luther, G. L. Morgan, J. E. Nordholt, C. G. Peterson, and C. M. Simmons, "Practical free-space quantum key distribution over 1 km," *Phys. Rev. Lett.*, vol. 81, no. 15, pp. 3051–3301, 1998.
- [130] J. G. Rarity, P. R. Tasper, P. M. Gorman, and P. Knight, "Ground to satellite secure key exchange using quantum cryptography," *New Journal of Physics*, no. 4, pp. 82.1–82.21, 2002.
- [131] J. Rarity, M. Aspelmeyer, H. Weinfurter, C. Kurtsiefer, P. M. Gorman, P. R. Tapster, T. Jennewein, M. Pfennigbauer, W. R. Leeb, and A. Zeilinger, "Quantum communications in space," in *Proc. CLEO Europe, Conference on Lasers and Electro-Optics*, 2003.
- [132] J. E. Nordholt, R. J. Hughes, G. L. Morgan, C. G. Peterson, and C. C. Wipf, "Present and future free-space quantum key distribution," in *Proc. SPIE, Free-Space Laser Communication Technologies XIV*, vol. 4635, January 2002, pp. 116–126.
- [133] R. J. Hughes, W. T. Buttler, P. G. Kwiat, S. K. Lamoreaux, G. G. Luther, G. L. Morgan, J. E. Nordholt, and C. G. Peterson, "Quantum cryptography for secure free-space communications," in *Proc. SPIE, Free-Space Laser Communication Technologies XI*, vol. 3615, January 1999, pp. 98–103.
- [134] M. Pfennigbauer, W. R. Leeb, M. Aspelmeyer, T. Jennewein, and A. Zeilinger, "Free-space optical quantum key distribution using intersatellite links," in *Proc. CNES Workshop on Intersatellite Links, Toulouse*, November 2003.

- [135] M. Aspelmeyer, T. Jennewein, M. Pfennigbauer, W. R. Leeb, and A. Zeilinger, "Long-distance quantum communication with entangled photons using satellites," *Journal of Selected Topics in Quantum Electronics*, vol. 9, no. 6, pp. 1541–1551, 2003.
- [136] R. Kaltenbaek, M. Aspelmeyer, T. Jennewein, C. Brukner, A. Zeilinger, M. Pfennigbauer, and W. R. Leeb, "Proof-of-concept experiments for quantum physics in space," in *Proc. SPIE, Optical Science and Technology, 48th annual meeting, San Diego (CA)*, 2003.
- [137] M. Pfennigbauer, W. R. Leeb, G. Neckamm, M. Aspelmeyer, A. Zeilinger, G. Baister, H. J. Egli, K. Kudielka, and T. Dreischer, "Accommodation of a quantum communication transceiver in an optical terminal (ACCOM): Technical Note 1: Review of objectives, scenarios and applications," Institut für Nachrichtentechnik und Hochfrequenztechnik, TU Wien, Institut für Experimentalphysik, Universität Wien, Contraves Space AG, Zürich," European Space Agency Contract Report, ESTEC, Contract No. 17766/03/NL/PM, 2004.

Curriculum Vitae – Martin Pfennigbauer

Address: Frauentorgasse 42, A-3430 Tulln, Austria
Date of Birth: Nov. 7, 1973
Citizenship: Austria
Martial Status: married

Education:
1980-1984: Elementary school St.Andrä-Wördern
1984-1988: Secondary school, Bundesrealgymnasium Tulln
1988-1993: Technical college, TGM Vienna (final exam passed with highest honors in June 1993)
1993-2000: Master studies at Vienna University of Technology (electronics and communications engineering)
June 2000: graduation (Diplomingenieur) with highest honors
since July 2000: Ph.D. studies in the field of optical communications, Vienna University of Technology

Civilian Service:
February 2002 - January 2003: Hospital Tulln
Network administration

Languages:
German (mother tongue)
Englisch (business fluent)
French (basics)

Professional Experiences:
since 03.07.2000: Assistant professor at Vienna University of Technology, Institute of Communications and Radio Frequency Engineering
September 1993 - June 2000: Benning GmbH (power systems) part-time job in the design and documentation department
Summer 1991: Benning GmbH
Summer 1990: Beckman (biomedical equipment)
Summer 1989: Zauner (electrical installation)